TAMPEREEN TEKNILLINEN YLIOPISTO
TAMPERE UNIVERSITY OF TECHNOLOGY

ENRICO MANUZZATO

DIGITALLY-CONTROLLED ELECTRICAL BALANCE DUPLEXER FOR TRANSMITTER-RECEIVER ISOLATION IN FULL-DUPLEX RADIO

Master of Science thesis

Examiner: prof. Mikko Valkama
Examiner and topic approved by the Faculty Council of the Faculty of Computing and Electrical Engineering on 9th December 2015

ABSTRACT

ENRICO MANUZZATO: Digitally-Controlled Electrical Balance Duplexer for Transmitter-Receiver Isolation in Full-Duplex Radio.
University of Trento and Tampere University of Technology
Professor Mikko Valkama (Tampere University of Technology), Fabrizio Granelli (University of Trento)

Keywords: Antenna tuning, digital control, electrical balance duplexer, full-duplex radio, hybrid junction, tracking, transmitter-receiver isolation.

Today's traditional radio systems exploit two techniques to transmit and receive which are Time Domain Duplexing (TDD) and Frequency Domain Duplexing (FDD). These two techniques allow bidirectional communication exploiting different frequencies or time-slots for the transmission and receiving operations. The ongoing research on wireless communications is currently active under in-band Full-Duplex (FD) radio communications, where co-located transmitter and receiver are operating simultaneously at the same central frequency doubling the spectral efficiency. The main technical challenge consists in suppressing the strong self-interference (SI) which is caused by the transmitting (TX) leakage into the receiving (RX) chain. Thus, FD transceivers need to provide high TX-RX isolation requirements in order to suppress the SI. Different methods are employed to mitigate the effect of the SI pursuing then FD operation. Generally, passive isolation between the TX and RX in the radio frequency (RF) domain can be built on specific antenna technologies or hybrid junction based electrical balance duplexers (EBD). On top of these, active SI cancellation is also typically required, either at analog/RF stages or digital baseband or both.

This thesis work presents a novel digitally-controlled electrical balance duplexer prototype capable of inband FD radio communications. The developed EBD prototype works in the ISM-Band, at 2.4-2.48 GHz, and can achieve TX to RX isolation of 53 dB across an 80 MHz instantaneous bandwidth. The prototype is composed of three parts, namely coupled line hybrid junction, triple-Pi balancing impedance and antenna tuning unit (ATU) which are all realized with commercial off-the-shelf components and implemented over a two layer FR4 board. The EBD contains also a self-adaptive or self-healing digital control system enabling automatic tracking of time-varying antenna impedance characteristics, providing robustness against fast changes in the surrounding environment and against user interactions. In addition to the architecture and operating principle descriptions, we also provide actual RF measurements at 2.4 GHz ISM band with real antenna connected, demonstrating the achievable isolation levels with different bandwidths and when operating in different environmental conditions. Furthermore, isolation performances are measured when operating with different antennas and under a low-cost highly nonlinear power amplifier.

PREFACE

This Master's thesis work has been carried out in Tampere University of Technology (TUT) during the academic year 2014-2015. I've spent more than one year and half on the Erasmus exchange program in Tampere University of Technology. Here, I got the chance to learn a lot of different things and meet people from all over the world, studying, living, working and experiencing something unique. I will always be grateful to Finland for this experience that has opened my mind and changed me a lot.

Concerning this thesis work, I got the chance to put into practice all the microwave engineering theory that I have studied. The prototype have been designed from the scratch and the design is inspired to the existing literature works. The implemented duplexer was fabricated and tested in the department of Electronics and Communications Engineering at TUT. The prototype's design goals have been generally satisfied, but still some improvements can be done. However, the prototype exhibits extraordinary isolation performance and up to 53 dB of TX-RX isolation are measured for 80 MHz wide signal bandwidth. Even I got surprised when I saw that !

Many people deserve my thanks starting from the professor Mikko Valkama who offered me the chance to join the full-duplex research group. Here I got the chance to learn a lot of practical knowledges exchanging tips&tricks with the other teammates. My best thanks to Timo Huusari for teaching me how to use the lab equipment and all the RF-tricks! Another thanks to Joose Tamminen for helping me with the digital-control, Matias Turunen for the RF-tips, and Dani Korpi for the control algorithm trips!

Special thanks also to the Intel folks and all the technical feedbacks.

Many thanks also to my dear friend and professor Olli-Pekka Lundèn who has introduced me the basic PCB fabrication technique and guided during the design phase giving lots of technical feedbacks. I would like to thanks all my Erasmus friends, who shared with me this awesome experience. A special thanks to Amir for all ours kahvi-breaks and meals, and especially for supporting me even when anything was working. Many thanks also to my supervisor Fabrizio Granelli who helped me with my staying in Finland and supported me during this exchange period.

Finally I would like to thank my family who supported me for all this time and especially during the academic career. A special thanks also to my unitn-crew to have supported throughout my studies.

Kiitos!

Zugliano, 21.02.2016

Enrico Manuzzato

CONTENTS

LIST OF FIGURES

LIST OF SYMBOLS AND ABBREVIATIONS

AC	alternating current
ADC	analog-to-digital converter
ADS	advanced design system, RF-simulation design tool
ATU	antenna tuning unit
BAL	balancing impedance
BB	baseband, refers to the down-converted RF signal
BeMicro	microcontroller board
CARG	compound annual growing ratio
dB	decibel unit
dBm	decibel unit, expressed with 1mW power reference
CMOS	complementary metal oxide semiconductors
CMRR	common mode rejection ratio
CSMA	carrier sense multiple access
DAC	digital-to-analog converter
DC	direct current
DLS	dithered linear search
DUT	device under test
EDB	electrical balance duplexer
EMI	electromagnetic interference
FD	full-duplex
FDD	frequency division duplexing
PCB	printed circuit board
FIR	finite impulse response
FPGA	field-programmable gate array
FR4	composite material for RF-board
HD	high definition
IBFD	inband full-duplex
IEEE802.11	communication standards for wireless local network (WLAN)
IIP_3	input referred third-order intercept point
IIR	infinite impulse response
IL	insertion loss
IP_{1dB}	1-dB input compression point
IP3	third-order intercept point
ISM	industrial, scientific and medical radio band
Labview	system design software
LO	local oscillator
LNA	low noise amplifier

LTE	long term evolution
OIP_3	output referred third order intercept point
MAC	medium access control
MIMO	multiple-input multiple-output
MMSE	minimum mean squared error
PA	power amplifier
PIFA	planar inverted F antenna
PSD	power spectral density
R&S	Rode and Schwarz, radio frequency measurements and tests device
RF	radio frequency
RMS	root mean square
RL	return loss
RX	reception
SI	self-interference
SIR	signal-to-interference ratio
SNR	signal-to-noise ratio
SOI	signal of interest
TDD	time division duplexing
TOI	third-order intercept point
TUT	Tampere University of Technology
TX	transmission
VGA	variable gain amplifier
VNA	vector network analyzer
VST	vector signal transceiver
WARP	wireless open-access research radio platform
Wi-Fi	wireless fidelity, standard for wireless communication in local networks.
WLAN	wireless local area network

1. INTRODUCTION

Wireless technologies are nowadays used in our daily life providing affordable and time efficient services to the human society. The research on wireless communication technologies has always been active resulting in an exponential growth of mobile communications processing capability of devices such as smart phones, laptops, and tablets. Nowadays all these devices can exploit the power of wireless communication technology providing *high definition* (HD) videos and audio streaming, sharing medias, and lots of other services. The ever-increasing needs of higher data rates and massively increasing device populations are creating constant push towards developing new methods and technologies to increase the capacity of wireless communication networks.

Cisco VNI Forecast [43] is an ongoing initiative to track the global mobile traffic projections and growth trends. Different worldwide analysis show that the global mobile data traffic grew an estimated 74% just in 2015. The overall mobile data traffic is expected to grow to 30.6 exabytes per month by 2020 with a *compound annual growing rate* (CAGR) of 53% from 2015 to 2020 [43].

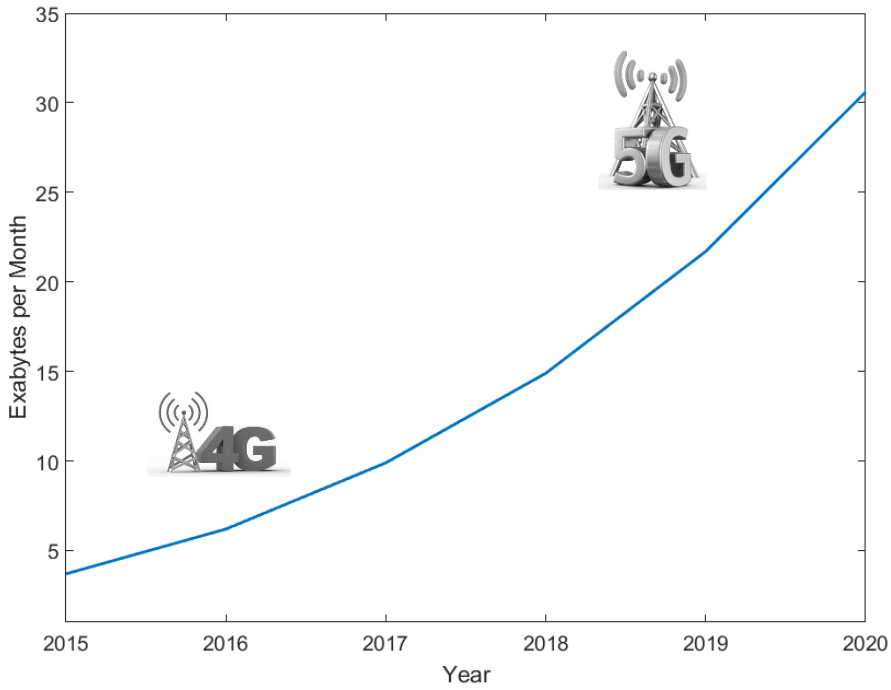

Figure 1. *Global mobile data traffic growth forecast 2015-2020 [43].*

As the data rates and network capacity are strongly connected to the amount of the available radio spectrum, which is generally a very scarce resource, finding ways to increase the efficiency and flexibility of the spectrum utilization is one of the most essential targets and ingredients towards the 5G radio networks.

In general, all existing radio communication systems exploit either *time division duplexing* (TDD) or *frequency division duplexing* (FDD), to enable bidirectional communication, where transmission and reception in an individual device are separated either in time or frequency. Thus, one intriguing method to increase the efficiency of the radio spectrum uses to transmit and receive simultaneously at the same center-frequency, commonly referred to as the *in-band full-duplex* (IBFD) radio principle. Such technology can in principle double the spectral efficiency of an individual radio link and increase the network capacity, while also potentially simplifying the radio network frequency planning [1]. Figure 2 shows the working principles of these three duplexing methods.

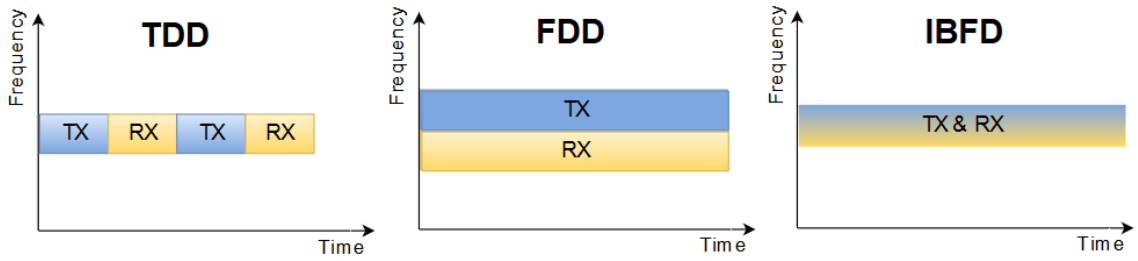

Figure 2. *Duplexing methods comparison. Left: Time Division Duplexing (TDD). Center: Frequency Division Duplexing. Right: In Band Full-Duplex (IBFD).*

One of the key technical challenges in IBFD communications is related to the suppression of the massively strong *self-interference* (SI), which is caused by the collocated *transmitter* (TX) and *receiver* (RX) operating simultaneously at the same carrier. Since the SI is a powerful signal and being TX and RX sharing the same channel is not possible to simply filter out the SI. Therefore, the detection of the RX signal is impossible because the desired signal is strongly masked by the SI. As the TX signal can in general be in the order of 100-120 dB stronger than the weak received signal, especially if the RX is operating close to its own sensitivity level, the overall TX-RX isolation requirements in the IBFD radio units are massively high, calling for novel antenna, *radio-frequency* (RF) circuit and digital signal processing solutions for their realization.

In the existing literature, several methods and solutions have been presented to suppress or mitigate the self-interference in IBFD radio transceivers. Generally, the SI is removed at different locations in the radio chain combining analog and digital cancellation. Different signal processing techniques and circuitry at RF and baseband spectrum have been recently developed resulting in passive and active SI cancellation. In general, providing elementary isolation between the TX and RX in RF domain can be building on specific antenna passive technologies such as circulators or hybrid junction based electrical balance duplexers. On top of these, active SI cancellation is also typically required, either at analog/RF stages or digital baseband or both. In spite of the required isolation performance requirements, IBFD benefits have motivated many research groups and industries to support and finance the realization of IBFD transceiver prototypes.

The aim of this master thesis is to develop, build and measure a new prototype of hybrid junction based *electrical balance duplexers* (EBD). Such EBD can enable relatively high TX-RX isolations representing one valid option to pursue in-band full-duplex operation. The EBD is

designed from the scratch and built in the department of Electronics and Communications Engineering at Tampere University of Technology (TUT). The project has been carried out in collaboration with Intel Wireless Labs. The author has been involved in the whole design process, practical realization and RF measurements of the prototype since the early stage of the project. For time reasons, the prototype is at its first revision and it has not be optimized in its physical layout implementation because the main goal was proofing the EBD's working principle and its isolation property.

The thesis is organized as follows. The next chapter introduces the background theory and the full-duplex challenges. Chapter 3 presents the EBD's working principle and describes each key elements that characterized the duplexer. Moving towards Chapter 4, design and implementation steps of the realized EBD prototype are presented in details. Chapter 5 is dedicated to the measurement results and their analysis. Finally, Chapter 6 concludes the thesis work.

2. BACKGROUND THEORY AND FULL-DUPLEX CHALLENGES

This chapter presents the main theoretical full-duplex related concepts. The chapter starts with a general overview of the IBFD potentiality and motivations. A high level block diagram of a full-duplex transceiver is presented explaining the main challenges. Therefore, the theoretical background and concepts that are involved in the EBD design are described.

2.1 In Band Full-Duplex: Motivations and Benefits

Generally the term full-duplex describes a system where data can be transmitted in both directions at the same time. That is not a completely new concept in communication technology and full-duplex systems have already been developed in the past. As an instance, the first telephone line system allowing bidirectional communication was implemented using the same TX and RX frequency band, but the signal was transmitted and received over different mediums, i.e., coaxial cable. As mentioned previously in the introduction, today's traditional radio systems exploit two different half-duplex techniques to transmit and receive data which are *Time Domain Duplexing* (TDD) and *Frequency Domain Duplexing* (FDD). These two techniques allow bidirectional communication exploiting different frequencies or time-slots for the transmission and receiving operations. Since full-duplex has emerged as an attractive solution for increasing the throughput of communication systems and networks, the recent research activity has been working to push the capacity of a single channel close to its limit. In order to do that, in band full-duplex communications challenges and opportunities have been studied and proposed as one of the most essential ingredients towards the 5G radio networks. The term *inband full-duplex* (IBFD), often shorten to *full-duplex* (FD), identifies a system where collocated transmitter and receiver operate simultaneously at the same central frequency. There are several advantages deriving from the co-existence of two data streams into the same channel such as doubling the capacity and the spectral efficiency. In [7] FD has demonstrated an increase of 84% in the medium throughput performance comparing with a standard TDD method.
One of the most interesting benefits of FD results in the simplification of the radio network frequency planning [7]. Since TX and RX share the same frequency band, no more frequencies are needed to allow bidirectional communication. Therefore, FD can practically halve the occupied bandwidth, saving then precious resources in terms of available radio spectrum.
FD can also increase the performance in *medium access control* (MAC) protocol, solving the hidden node problem [7]. The hidden node problem occurs in wireless networks when the nodes are out of hearing range each other. Figure 3 describes the typical situation in a wireless network where three nodes communicate.

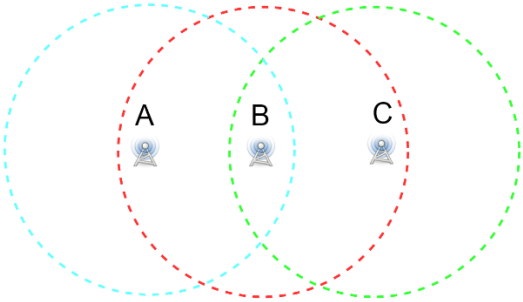

Figure 3. *Hidden node problem. Both nodes A and C can communicate with node B. If node A transmits data, node C might not be able to hear A. So, if C transmits data too, it will cause data packet collision.*

Being both nodes A and C far away each other and collocated at the opposite side of the network, they might not be able to sense the channel, before they transmit. Therefore, if A and C simultaneously transmit data to B the signals will interfere, causing packets collision. This situation is typical of the *carrier sense multiple access* (CSMA) [29] networks, where senders check if the channel is free before transmit, i.e. Wi-Fi networks. In a hypothetical FD scenario, hidden node problem can be solved and packets collision can be prevented. In fact, referring to Figure 3, node B can simultaneously transmit and receive data from A and C, informing then node C that the channel is busy. Thus, FD benefits can improve the overall throughput performance even in MAC based networks, stemming from hidden node problem.
FD potentiality can also be exploited in multi-hop relay networks where the signal is received, amplified and re-transmitted to one other area which is not covered by the *signal of interest* (SOI) [29]. In half-duplex systems the transmitted signal has to be fully received before the re-transmission phase starts, causing delay in the relay chain. Figure 4 shows a typical relay stations diagram where each station is characterized by its proper delay time T_d.

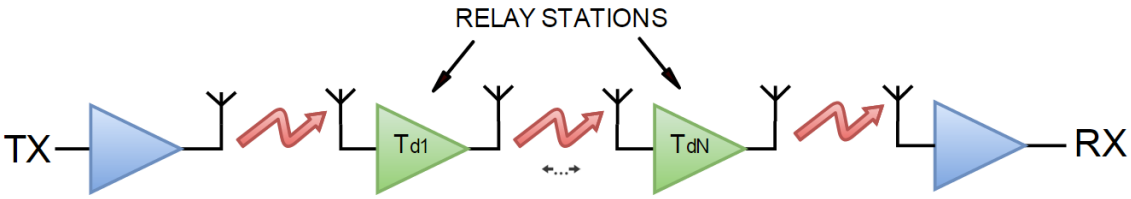

Figure 4. *Typical relay stations architecture. Each station has a specific delay time T_d. The total end-to-end delay is proportional to the number of stations and the distance between them.*

Exploiting FD technologies, the relay station can straight forward the SOI while receiving it, reducing the end-to-end delay in multi-hop relay networks.
One other very interesting uses of FD would be in cognitive radio networks. In cognitive radio networks secondary users have to release the spectrum when primary users decide to transmit [29]. So, the channel is scanned by the secondary user to detect the activity of the primary one. However, this operation is possible when just the secondary users are not transmitting. FD technology allows the secondary user to scan the channel and look for the primary user activity while they are transmitting data. This increase the overall throughput performance making cognitive radio networks more efficient.

2.2 Full-Duplex and Challenges

One of the key technical challenge in FD communications consists in removing the strong SI, which is caused by the TX leakage into the RX chain. Figure 5 shows the TX leakage in a typical single shared antenna RF front-end architecture implemented with an EBD.

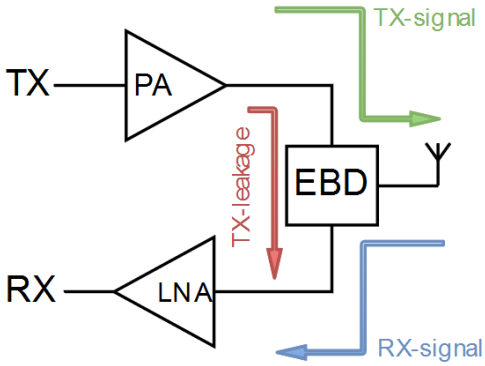

Figure 5. *Typical single shared antenna RF-front end architecture with EBD.*

The signal power level at the *power amplifier* (PA) output stage is usually in the order of 100-120 dBs more than the RX signal. Therefore, the TX-leakage masks completely the weak RX signal appearing at the *low noise amplifier* (LNA) input. Furthermore, the TX-leakage causes the saturation of the LNA and the *analog-to-digital converter* (ADC) along the RX chain, making impossible the detection of the RX signal. Therefore, as mentioned in the introduction, the TX-RX isolation requirements in the FD radio need to be very high.
For estimate the isolation order of magnitude in *wireless local area network* (WLAN), several parameters need to be considered. Starting from the thermal noise floor *power spectral density* (PSD) expressed as follows

$$\mathrm{N} = 10 \cdot log_{10}\left(\frac{k \cdot T\ (W)}{1 \cdot 10^{-3}\ (W)}\right) \quad \left[\frac{dBm}{Hz}\right] \tag{1}$$

where k is the Boltzmann's constant equal to $1.38 \cdot 10^{-23}$ J/K, T is the temperature in kelvin. Considering T=290°K (17°C), for a wideband 80 MHz signal the thermal noise power level results equal to -95 dBm. The typical RF transmit power levels in Wi-Fi and cellular user equipment are limited to the range +20…+25dBm (UE devices). Therefore the SI need to be suppressed below the RX noise floor, in order to avoid the degradation in the RX *signal to noise ratio* (SNR) due to the SI. So, in Wi-Fi systems, this means that more than 115 dB of SI suppression is required [15] . For *long term evolution* (LTE) systems the isolation requirements is even higher and close to 123 dB. This means that the interference has to be drastically reduce by a factor of over 1 trillion [15]. Because of this reason, FD was assumed to be practically impossible until nowadays. Figure 6 shows the overall power levels and the isolation requirement in a WLAN network for 80 MHz wideband signal.

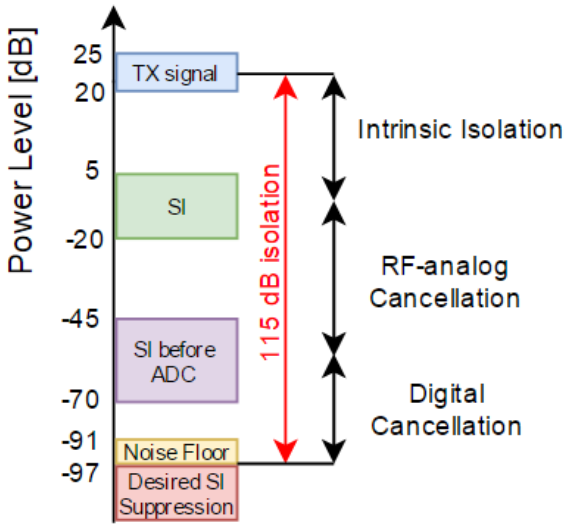

Figure 6. *Overall power levels for a WLAN network considering a 80 MHz wideband signal.*

In the existing literature several solutions can be found to satisfy the overall isolation requirements combining RF-analog cancellation, digital cancellation and antenna-based solutions. Figure 7 shows where the RF-analog and digital cancellations are performed along the RX chain in a FD transceiver.

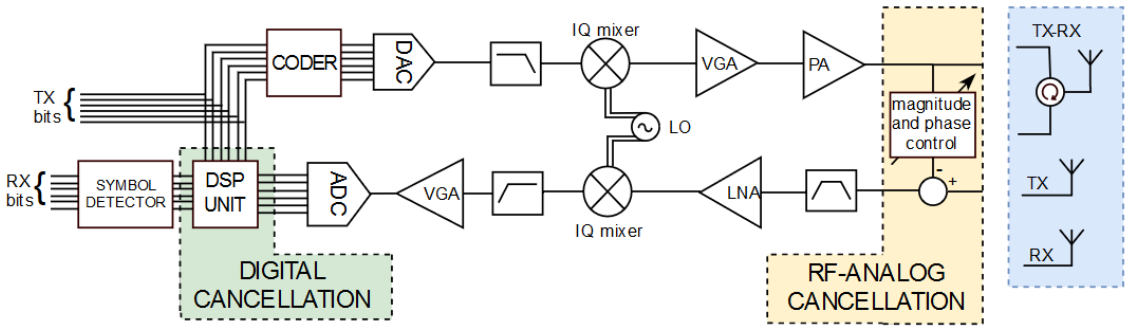

Figure 7. *Typical FD transceiver is illustrated. It integrates a RF-analog cancellation (orange area) and digital cancellation (green area) circuits. On the right side (blue area) multiple and shared antenna configuration are presented employing circulator-based solution and separated TX-RX antennas/arrays.*

Those cancellation techniques are required to obtain that huge amount of SI suppression. Considering Figure 7, both antenna configurations exhibit their own intrinsic isolation. In shared antenna configuration, circulators are typically used providing isolation between 15 and 20 dB. Different antennas configurations can be also used. Multiple/MIMO systems [7] presents 20-30 dB of isolations employing multiple transmitting antennas that create a spatial null toward the receiving one. This, however, has the downside of calling for separate TX and RX antennas/arrays, which may potentially be feasible in, i.e., relay type of devices but not in smaller form-factor consumer devices.

The RF-analog cancellation is implemented before the LNA input in order to protect it from saturation issues caused by the high SI power level. RF-analog cancellation is also needed before the LNA to relax the ADC dynamic range requirements in the RX architecture. The RF-

analog cancellation stage exploits a relatively simple theoretical concept to suppress the SI, which consists in changing magnitude and phase of the TX signal, subtracting it from the RX one. The SI is in fact a close copy of the TX signal, but modified in its magnitude and phase frequency responses. So, the SI signal is the result of the changes and distortions along the TX and RX paths. Therefore, SI suppression is strongly related to the ability to model those changes. This result in a proper active RF cancellation circuit called RF-canceller that is able to generate a copy of the SI, removing it from the RX signal. State-of-the-art RF-analog cancelers, such as the one reported in [2], can typically provide 30-50dB of active SI suppression. Digital cancellation is implemented in *baseband* (BB). Its working principle exploits the same concept as analog cancellation. A digital copy of the SI is subtracted from the digital RX signal in form of digital samples. Digital filters such as FIR and IIR, characterized by specific impulse response, are applied to the TX signal samples in order to match magnitude and phase frequency responses of the SI. Therefore, the signal is again subtracted from the RX signal samples. The filters are inserted in a feedback system in the DSP unit and the parameters are specifically tuned optimizing an error function.
Combining all those analog and digital cancellation techniques altogether it is possible to suppress the SI down to the RX noise floor level. This, in fact, represents the main challenge in a FD scenario. High RX architecture complexity is needed, integrating multiple digital and analog control systems able to mimic and track the SI signal at different stage along the RX chain.

2.3 Scattering Parameters

Scattering parameters (S parameters) are very important in microwave design because they are conceptually simple, analytically convenient, and capable of providing a great insight into a measurement and design problem. Figure 8 illustrates a two-port network device. The scattering matrix is defined by four parameters S_{11}, S_{12}, S_{21}, and S_{22} that allow to describe the input-output ports relations of the two-port network device. Considering Figure 8, the a_n terms represent the electromagnetic wave travelling towards the device while the terms b_n denote the reflected one. Their ratios identifies the aforementioned four S-parameters that describe the device in all its ports interactions. The parameters S_{11} and S_{22} express the forward and the reverse reflection coefficients, while S_{12} and S_{21} are respectively the forward and the reverse gains. All those parameters are frequency-dependent complex numbers that describe magnitude and phase responses of each port transfer function.

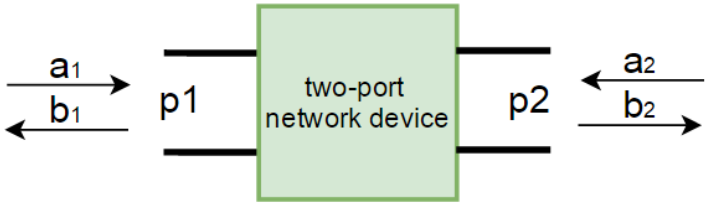

Figure 8. *Scattering Parameters in a two-port network device.*

The two-port network device shown in Figure 8 can be described as follows:

$$\begin{bmatrix} b_1 \\ b_2 \end{bmatrix} = \begin{bmatrix} S_{11} & S_{12} \\ S_{21} & S_{22} \end{bmatrix} \begin{bmatrix} a_1 \\ a_2 \end{bmatrix} \quad (2)$$

The terms S_{11} and S_{22} have the meaning of reflection coefficients, while S_{21} and S_{12} are related to the transmission coefficients. In RF and microwave engineering the terms S_{11} and S_{21} are more conveniently used to design and characterize antennas or amplifiers. The term S_{11} in fact identifies the input reflection coefficient which expresses the amount of the incident power that is reflected back to the source. The term S_{21} represents the forward gain or loss. These two parameters are found terminating the network with a load equal to the reference impedance (Z_0) forcing then the term a_2 equal to zero.

$$S_{11} = \frac{b_1}{a_1} \quad , a_2 = 0 \quad (3)$$

$$S_{21} = \frac{b_2}{a_1} \quad , a_2 = 0 \quad (4)$$

For reflection and transmission parameters the decibel form refers to as return loss (*RL*) and insertion loss (*IL*) respectively.

$$RL_{dB} = 10log_{10}|S_{11}|^2 \quad (5)$$

$$IL_{dB} = 10log_{10}|S_{21}|^2 \quad (6)$$

Often in amplifier design the *IL* has to match a specific value given by the design specs and the *RL* has to be low enough to minimize the reflected power. A general rule of thumb specifies a proper impedance matching conditions for *RL* higher than 10 dB. This means that just the 10% of the transmitting power is reflected back to the source.
Altogether the scattering parameters represent the scattering matrix for the two port network device. Although two-port network represents the easiest case, S-parameter analysis can be extended to any kind of n-port device.
Furthermore, S-parameters analysis such as Mixed Mode [31] can be used to combine together single ended S-parameters data to fully characterize a differential port device. In this thesis work, S-parameter simulations and measurements have been extensively used to design the EBD prototype and to validate the results.

2.4 Differential Port Devices

Differential port devices are widely used in analog circuits to reduce the *electromagnetic interference* (EMI) and noise issues to improve the signal quality. However, in traditional microwave theory, electric current and voltage are treated as single-ended and the S-parameters are used to describe single-ended signaling [41]. This makes advanced microwave and RF circuit design and analysis difficult, when differential signaling is utilized in modern communication circuits and systems. This section introduces the technique to deal with differential signaling

in microwave and millimeter wave circuits explaining the parameter that characterize a differential device.
As reported in [31] , Figure 9 shows a balanced to single ended and a fully balance devices. Generally, differential-mode signal are characterized by the same amplitude and 180° phase shift, which creates a virtual ground along the axis of symmetry of the device. Common-mode signal differs from the differential ones because they are characterized by the same amplitude and phase.

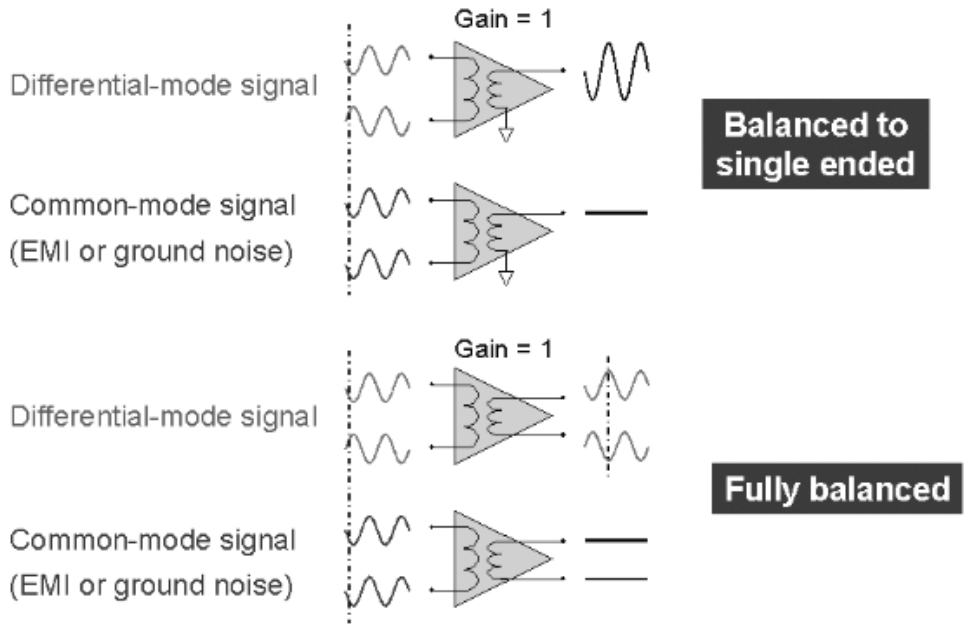

Figure 9. *Single ended and differential outputs [31].*

When using common-mode signals, differential and single ended components don't differ in terms of performance. That is no true when differential-mode signal are applied, rejecting then common-mode signals. For example, in radio communication the EMI affects both terminals with the same phase shift, appearing to the device as a common-mode signal.

2.4.1 Mixed Mode

Mixed-mode S-parameters technique is a mathematical method that transform single-ended data to differential parameters for characterize a differential device. A single stimulus signal is applied to each port and the response is measured [31]. This is a very useful procedure because datas are often measured with a *vector network analyzer* (VNA) having single-ended probes. Thus, just single-ended data are available. Mixed-mode S-parameter technique essentially seeks to determine (with a differential-mode stimulus on a differential port) the corresponding differential and common mode responses on all the device port. For a common mode stimulus it determines the differential mode and common mode response [31]. Figure 10 shows a generic two port device, where the Mixed-mode S-parameter matrix is defined by the rows and columns which represent the stimulus and response conditions respectively.

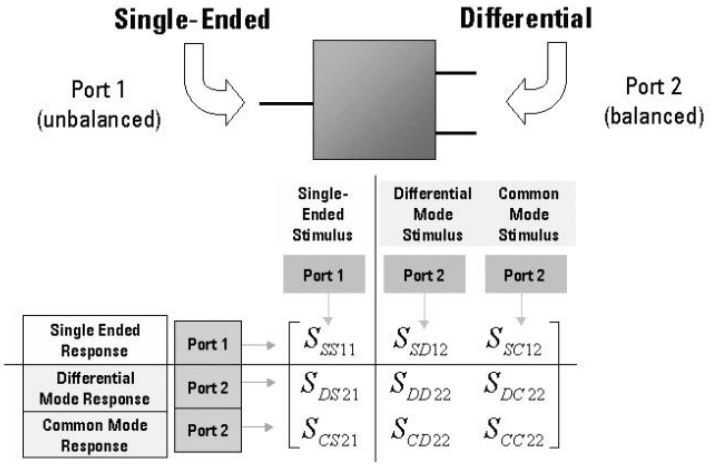

Figure 10. *Mixed mode S-parameter matrix of a two port differential device [31].*

The naming convention includes the sequence mode response, mode stimulus, port response and port stimulus. Here, two columns and two rows describe the differential port while one column and one row identify the single ended port. It is obvious that the term S_{SS11} describes the reflection coefficient at Port 1, while the terms S_{ij22} represent the four different reflection coefficient at Port 2. All the other parameters describe the differential and common mode transmission characteristic in the forward and reverse direction [31].

The *common-mode rejection ratio* (CMRR) is the figure of merit used to describe differential system. It is defined as the ratio between the transmission characteristic in the differential mode over the transmission characteristic in the common-mode of the balanced port. High CMRR value means more rejection of common mode, which is desirable in differential devices. The differential-mode and common-mode responses are typically expressed in dB scale.

$$CMRR_{dB} = 10\,log\left(\frac{\mathrm{S_{DS21}}}{\mathrm{S_{CS21}}}\right)^2 \tag{7}$$

The imbalance is also an important parameter when describing the performance of a differential circuit. The imbalance express the difference in the transmission characteristic between the two single-ended balanced ports (A, B) when a single ended stimulus is applied. Imbalance is typically expressed in its magnitude and phase response.

$$Imbalance = -\frac{(\mathrm{S_{SS21}})_A}{(\mathrm{S_{SS21}})_B} \tag{8}$$

2.5 Impedance Matching and Matching Networks

Impedance matching is a well-known topic in RF-engineering which is often a part of the larger design process for microwave component or system. The basic idea of impedance matching is illustrated in Figure 11, where an ideally losses matching network is inserted between the generator and the load impedance.

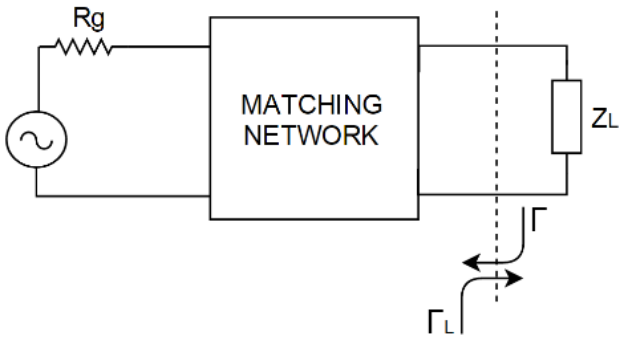

Figure 11. *Matching Network placed between the source and the load.*

When delivering ac power to complex load impedances, maximum real power is delivered to the load when the source impedance presented to the load is equal to the complex conjugate of the load impedance [17]. The load impedance is often an antenna which impedance can vary due to changing in the surrounding antenna's environment, changing in the antenna configuration, operating frequencies and antenna-user interactions. So, in order to maximize the source-load power transfer the matching network should be dynamically adjusted every time when there is a variation in the load impedance. The purpose of the impedance matching network therefore is to ensure that the source impedance seen by the load is exactly its complex conjugate [17].
Such situation is called conjugate matching and it can be expressed considering the reflection coefficients shown in Figure 11, such that

$$\Gamma = \Gamma_L^* \tag{9}$$

Where Γ is the output matching network complex reflection coefficient seen by the load and Γ_L^* is the complex conjugate reflection coefficient of the load impedance.
To design an impedance matching network, different topologies can be used: L-structure, Pi-structure [17], T-structure [40], line transformers and distributed components [38]. Several factors need to be considered in the selection of the particular matching network. Complex matching networks are generally more expensive and lossy than the simple one, but they can match the load impedance for a wider frequency band. On the other hand complex matching networks are more difficult to tune due to the infinite number of possible combinations available for a specific impedance matching problem.

2.5.1 VSWR

The *voltage standing wave ratio* (VSWR) is a parameter that is often used in the industry to characterize how efficiently the transmitting power is transferred from the power source to the load, using a transmission line. Figure 12 describes one of the most common example where the generator sends a RF signal to an antenna over a transmission line.

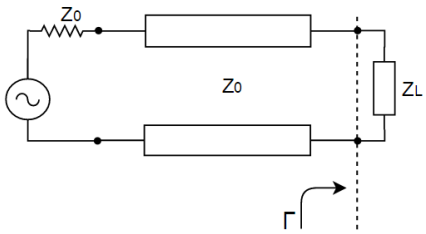

Figure 12. *Transmission line with generator and load impedance.*

The VSWR can be expressed in function of the antenna input reflection coefficient (Γ) considering the load antenna impedance (Z_L) and the characteristic line impedance (Z_0) as follows:

$$\Gamma = \frac{Z_L - Z_0}{Z_L + Z_0} \tag{10}$$

$$\text{VSWR} = \frac{1 + |\Gamma|}{1 - |\Gamma|} \tag{11}$$

Standing waves are the distributed patterns of voltage and current along the line as a consequence of the incident and reflected wave superposition. Standing waves are in fact characterized by their minimum and maximum amplitude which defines the VSWR. The VSWR is a real and positive number greater than one. Perfect matching conditions are identify for VSWR equal to 1, when Γ is equal to zero. This happen when Z_L matches Z_0, so no transmitting power is reflected back to the source.
In practice, the industry standard specification for an acceptable antenna impedance variation is a VSWR of 3:1 [18]. This means that the 25% of the power delivered by the generator is reflected back to the source, and the 75% is delivered to the antenna.

2.6 Distortions in Non-Linear Systems

Distortions in non-linear systems are identifies in two different categories which are harmonic distortion and intermodulation distortion. Generally in amplifiers, harmonic distortion is caused by the input-output voltage characteristic which is not ideal because the voltage supply is not infinite, but limited to a specific value. When the input signal voltage exceeds that value, the output signal saturates to its maximum voltage driving the amplifier into clipping. This involves in the generation of an unwanted series of spurious signaling harmonics, whose frequency are integer multiples of the fundamental one. So, if we denote the fundamental frequency with f_0 the spurious harmonics will result at $2f_0, 3f_0, 4f_0$ and so on. Those harmonics are fortunately far away from the SOI, thus they can be easily filtered out.
Intermodulation distortion differs from the harmonic distortion because it is caused by the mixing between each frequency components of the signal. This leads to generate additional signals that are not at the harmonic frequencies, i.e. harmonic distortion, but at the sum and the difference of the original frequencies and at their respective multiples. In order to observe intermodulation distortion, the *device under test* (DUT) is fed with two sinusoidal tones at frequencies f_1 and f_2 with a small frequency gap. The closest intermodulation products occurring in

the DUT are the so called 3^{rd} order intermodulation products which are at the frequencies $2f_2 - f_1$ and $2f_1 - f_2$. Those intermodulation components are usually difficult to filter out because they are close to the SOI. Thus, RF system and components need to respect some intermodulation constraints. Figure 13 depicts the harmonic and intermodulation distortions considering the output power spectrum of a general non-linear device, enhancing their difference.

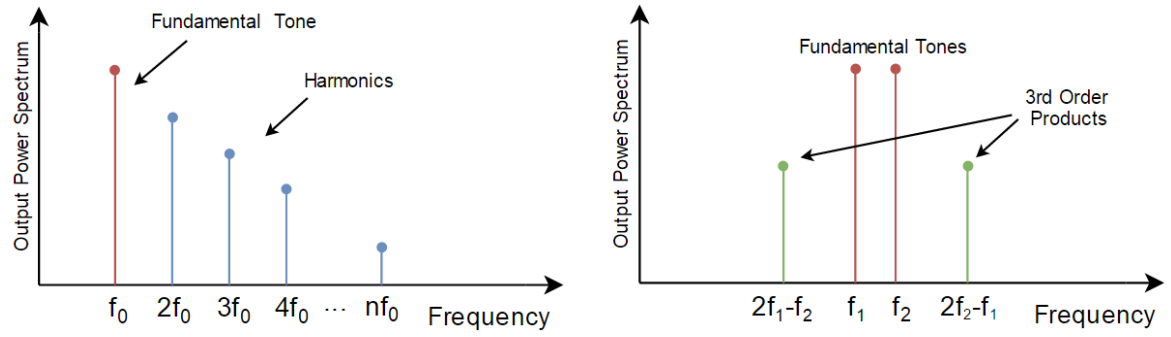

Figure 13. *Left: output power spectrum in presence of harmonic distortion. Right: output power spectrum in presence of intermodulation distortion.*

Third-order intercept point (IP_3 or TOI) and 1-dB compression point are a well-known parameters that gauge linearity in RF functions and components. The IP_3 is often used to characterize the intermodulation distortion. The amplitude of both fundamentals and 3^{rd} order intermodulation products are measured and the IP_3 is estimated. This is defined by OIP_3 and IIP_3 parameters which are respectively the output and input related interception points. Those parameters are defined as follows

$$IIP_3\ (\text{dB}) = \frac{3}{2}P_T - \frac{1}{2}P_{3rd} \tag{12}$$

$$OIP_3\ (\text{dB}) = IIP_3 + G \tag{13}$$

Where P_T is the power of a single fundamental tone, P_{3rd} is power level of the 3^{rd} order intermodulation product and G in the gain or attenuation of the DUT.

The figure of merit 1-dB compression point (IP_{1dB}) is commonly used to describe harmonic distortion in amplifiers. This point represents the minimum input power level to reduce the amplifier gain by 1 dB from the linear amplifier's response. This point identifies also different curves in the amplifier characteristic which are the *linear region* and *compression region*. Figure 14 illustrates the two commonly used figures of merit to describe distortions in non-linear system.

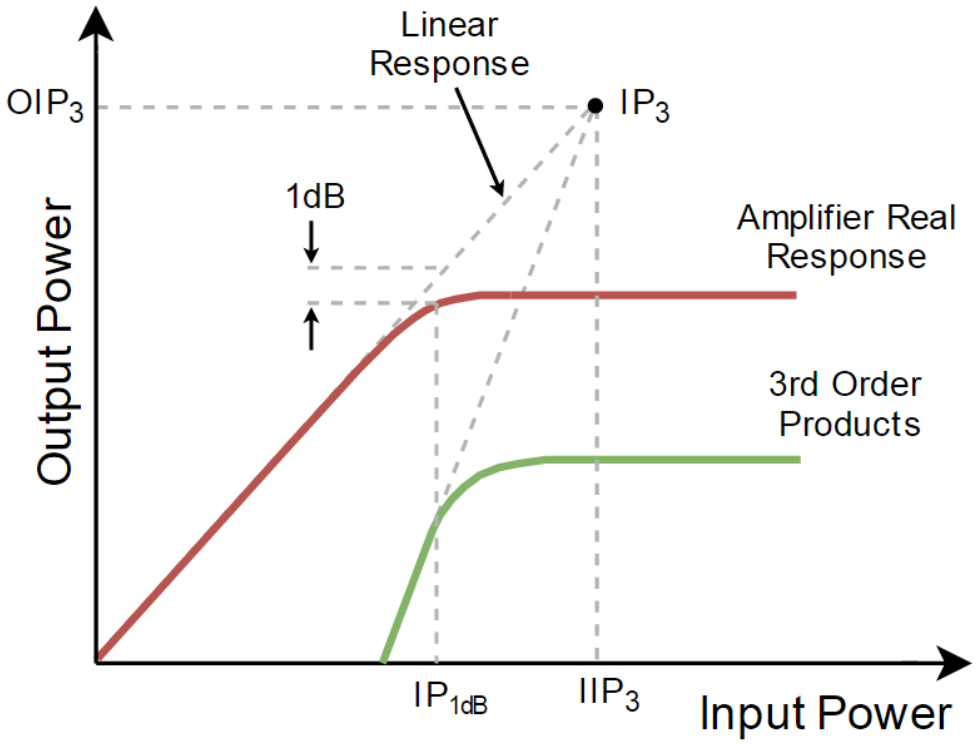

Figure 14. *Third-order intercept point (IP3 or TOI) and 1-dB compression point (IP_{1dB}).*

3. ELECTRICAL BALANCE DUPLEXER

The chapter starts with the theoretical background necessary to understand the working principle and properties of *electrical balance duplexer* (EBD). Each subsection presents each key element that can be found in an EBD. Hybrid junction, hybrid junction topologies, balancing impedance, antenna tuning unit and tuning algorithms are well described thoroughly the chapter. Finally, the existing EDB implementations are discussed at the end of the chapter.

3.1 Electrical Balance Duplexer

One alternative antenna based method to achieve high isolation levels is the electrical balance duplexer. Such EBD can enable relatively high TX-RX isolations allowing to share a single antenna. EBD are commonly implemented on a chip making it a suitable choice for handheld devices. EBD is not an unknown concept in communication technology and it has been used since the early stage in wired telephone lines [30]. In this case the challenge consists in isolating user's microphone (TX) and speaker (RX) to suppress the weak in-coming user's echo. Thus, considering that TX and RX share the same medium, i.e. twisted pair, the interfering signal needs to be removed to increase the *signal-to-interference ratio* (SIR).
Figure 15 illustrates the most typical EBD implementation which integrates four core elements, namely a hybrid junction, an antenna, a balancing impedance and a control system for tuning the balancing impedance. An *antenna tuning unit* (ATU) can also be included as an optional element. These are elaborated in more details in the following sections.

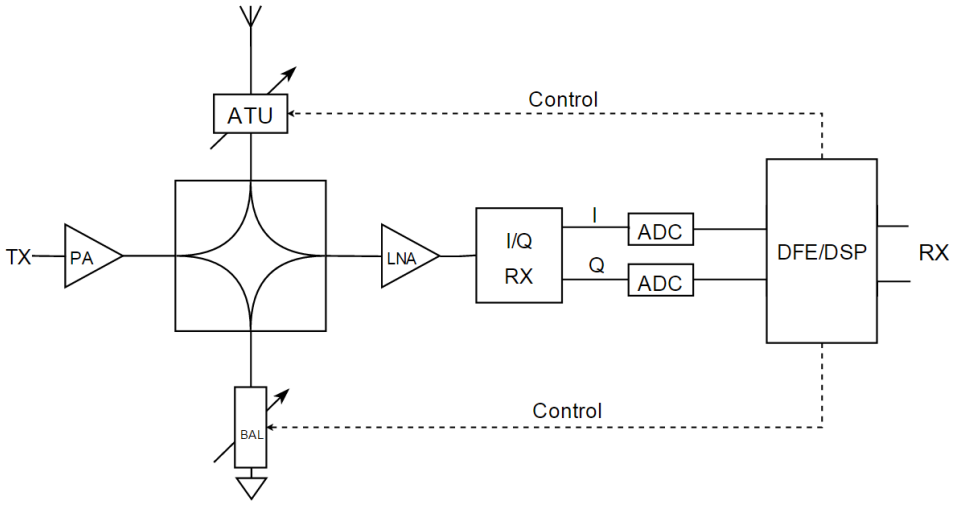

Figure 15. *Electrical Balance Duplexer (EBD) block diagram.*

The EBD is a four ports passive device that allows high TX-RX isolation. The hybrid junction represents the key core element of any EBD. All the other devices such antenna, ATU, balancing impedance circuit, TX and RX are connected to the hybrid junction terminations. The TX and RX are connected to a specific hybrid junction's pair of ports, while antenna and *balancing impedance* (BAL*)* are connected to the other two ports. The ATU can be inserted between the

antenna and the hybrid junction or even removed being an optional element. The EBD integrates the RX architecture in cascade with a control system to properly control the balancing impedance circuit. So, in order to simplify the discussion and make the EBD's working principle easy to understand let's denote with A, B, C and D the hybrid junction ports as depicted in Figure 16. The amount of isolation between A and B depends on the accuracy of the impedance matching between the ports C and D. If those impedances are perfectly matched, the isolation between ports A (TX) and B (RX) is theoretically infinite, otherwise the overall EBD's isolation performance decreases.

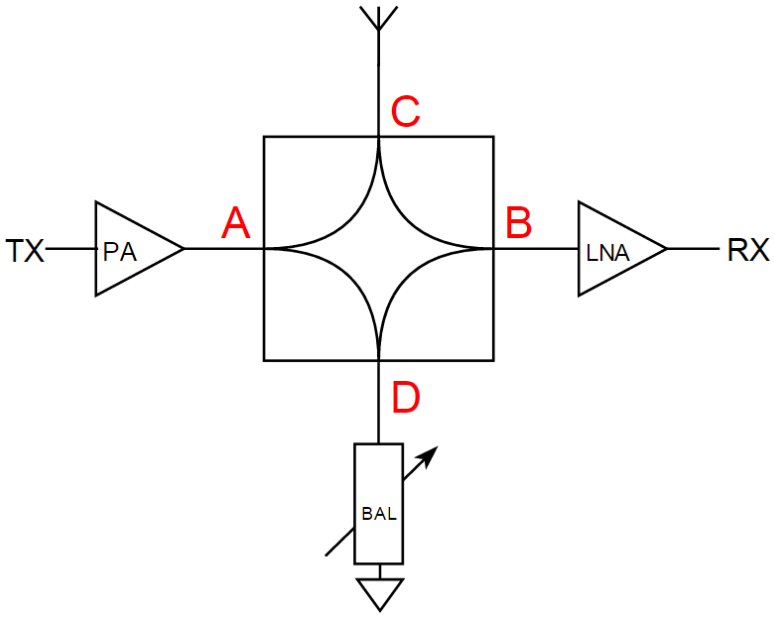

Figure 16. *EBD basic implementation: antenna, balancing impedance and hybrid junction.*

Therefore, since the antenna impedance is frequency dependent and it varies according to the changes in the surrounding antenna environment and antenna-user interactions [23], the balancing impedance needs to be controlled and adjusted with high accuracy to match the antenna impedance over the desired frequency range.
In order to simplify and have a more practical overview of the aforementioned balancing challenge it is useful to refer to a balancing operation in a simple balance. In this case the equilibrium state is dictated by the object's weight in each branch. If the weight of the objects in the two balance branches is equal, the system reaches its equilibrium point because the potential energy is the same. If just one of the object's weight is modified then the balance starts to swing. Thus, the balancing challenge consists in the ability to compensate the weight variation with high accuracy and time resolution.
This example represents perfectly the aforementioned balancing operation challenge, where the accuracy is represented by the ability of the balancing circuit to track the antenna impedance variation in all its frequency behavior, and the time resolution is given by the speed of the balancing operation. In conclusion, balancing operation represents the main challenge in an EBD duplexer, and its accuracy determines the isolation capability of the device.

3.2 Hybrid Junction

The hybrid junction is a four port lossless reciprocal device in which opposite pairs of ports are isolated one another [15]. This device has several key properties including bi-conjugacy and isolation between alternate sets of ports, impedance matching at each port, as well as the ability to split the TX and RX power in any desired portion between two ports. All these properties are explained thoroughly the section listing then all the other parameters that have been considered during the design. In order to simplify the explanation, the hybrid junction ports will be referred as the one reported in Figure 17. Generally in EBD, the PA output is connected to the TX port, the LNA input to the RX port, while antenna and balancing impedance are connected to ANT and BAL ports respectively.

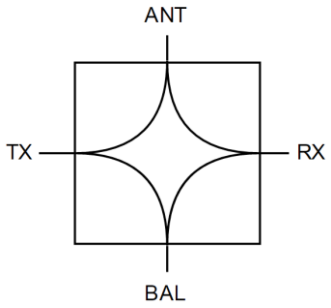

Figure 17. *Hybrid Junction symbol with four terminations*

Hybrid junction are commonly implemented using hybrid autotransformer [14], center tapped transformer [15], differential hybrid transformer [34], microstrip coupled line hybrid junction [16] and 90°or 180° hybrid couplers [15].

3.2.1 Bi-conjugancy

Concerning hybrid junction, the term bi-conjugate identifies two different ports that are electrically isolated from each other. Furthermore, from one of the four conjugate pair to one other there is a 180° phase shift. In order to achieve high isolation and bi-conjugancy between the ports all hybrid junction's terminations have to match a specific impedance value depending on the impedance relations. The most common criteria that have been used in transformer-based hybrid junction design is given by the following relation [32]:

$$Z_{ANT} = Z_{BAL} = \frac{Z_{TX}}{2} = 2Z_{RX} \tag{14}$$

where the Z_i term represent the impedance at each specific hybrid junction's port. Generally the nominal antenna impedance is 50 Ω, so that would impose some constraint in the choice of the port impedances.
Bi-conjugancy is one of the key properties of hybrid junctions. Thus, when (14) is satisfied the device is completely balanced and the port sets TX-RX and ANT-BAL are bi-conjugate.

3.2.2 Power Splitting

Hybrid junctions are passive devices which are not ideal and therefore present some losses. Figure 18 shows the power flows in a generic hybrid junction.

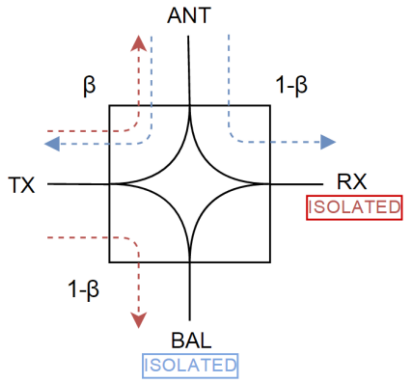

Figure 18. *TX and RX power flows through an hybrid junction.*

If an ideal antenna with fixed impedance Z_{ANT} is connected to ANT port and the same impedance is connected to BAL port, the hybrid junction results balanced. The red lines depicted in Figure 18 identifies the TX power flow which goes through the device, where it is then split between ports ANT and BAL. The blue lines denote the RX power flow which comes from ANT port and is then split between TX and RX ports. Since (14) is satisfied, the hybrid junction results balanced and the RX port is completely isolated from the TX one. The same happens to the BAL port which is completely isolated from the ANT port. The red power flow between TX and ANT ports represents the TX-path. Therefore, the effective transmitting power is equal to β and the losses to 1-β. The power flow between ANT and RX ports identifies the RX-path, where again the power is divided between TX and RX. Because of the symmetric property of hybrid junction, the term 1-β identifies the effective RX power. The relation between the TX and RX power is given by the power splitting ratio *r*.

$$r = \sqrt{\frac{\beta}{1-\beta}} \tag{15}$$

This relation imposes a trade-off constraint between the TX insertion loss (IL_{TX}) and the RX insertion loss (IL_{RX}) [10].

$$IL_{TX-dB} = 10log_{10}(1+\mathrm{r}) \tag{16}$$

$$IL_{RX-dB} = 10log_{10}\left(1+\frac{1}{\mathrm{r}}\right) \tag{17}$$

Lower insertion loss in one path can be achieved at the cost of higher loss in the other one by controlling the splitting ratio [10]. Typically in hybrid transformers, the power splitting ratio is

changed skewing the transformer in favor of one path. Figure 19 depicts TX and RX insertion losses in function of the power spitting ratio, without considering any additional losses which are presented in real circuit implementations.

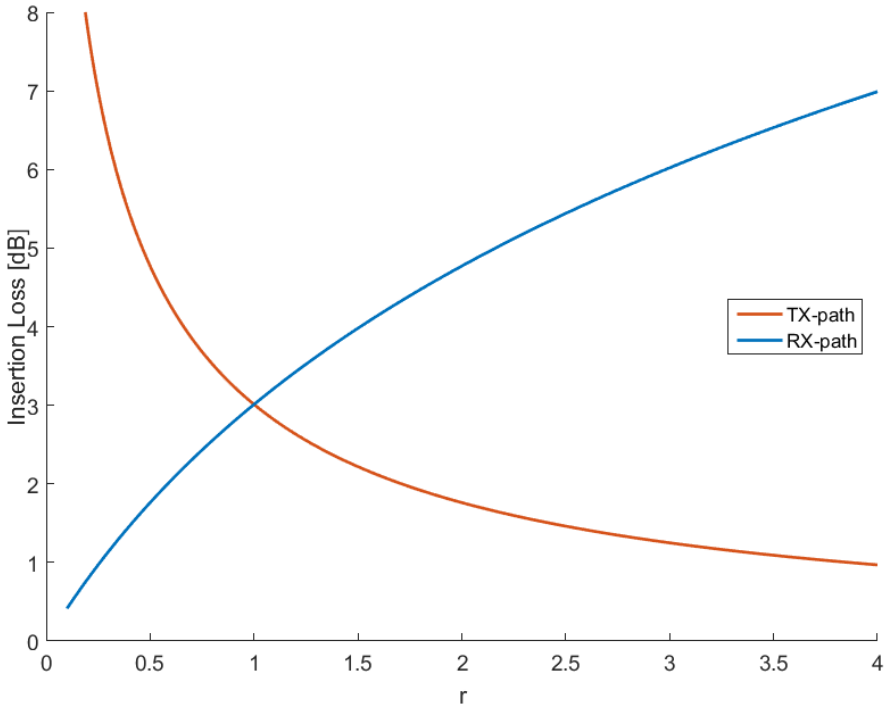

Figure 19. *TX and RX insertion losses trade-off in hybrid junction [15].*

The hybrid junction is symmetric when the power splitting ratio is equal to one. Thus, the insertion loss is equal to 3dB for both TX and RX. Depending on the application, the power splitting ratio can be skewed introducing asymmetry in the hybrid junction.

3.2.3 Isolation

Infinite isolation can be achieved with hybrid junction when the ports are bi-conjugate. In reality, the isolation is not infinite, but it can be very high if all the ports are well matched. Referring to Figure 20, TX and RX impedances are commonly fixed and they cannot be changed. Therefore, the TX-RX isolation depends on the complex antenna and balancing impedance frequency-dependent reflection coefficients resulting in the following expression

$$\Upsilon_{TX-RX,dB}(\omega) = 10log_{10}|\Gamma_{ANT}(\omega) - \Gamma_{BAL}(\omega)|^2 - 20log_{10}\left(\frac{1+r}{\sqrt{r}}\right) \quad (18)$$

where

$$\Gamma_{ANT}(\omega) = \frac{Z_{ANT}(\omega) - Z_0}{Z_{ANT}(\omega) + Z_0} \quad (19)$$

$$\Gamma_{BAL}(\omega) = \frac{Z_{BAL}(\omega) - Z_0}{Z_{BAL}(\omega) + Z_0} \quad (20)$$

with $Z_{BAL}(\omega)$ and $Z_{ANT}(\omega)$ denoting the complex frequency-dependent balancing impedance and antenna impedance respectively. Furthermore, Z_0 denotes the characteristic impedance which is usually 50 Ω for commercial devices. Therefore, $\Gamma_{BAL}(\omega)$ and $\Gamma_{ANT}(\omega)$ represent the balancing and antenna reflection coefficients, respectively. As is obvious, when $\Gamma_{ANT}(\omega) \approx \Gamma_{BAL}(\omega)$, high TX-RX isolation can be achieved.

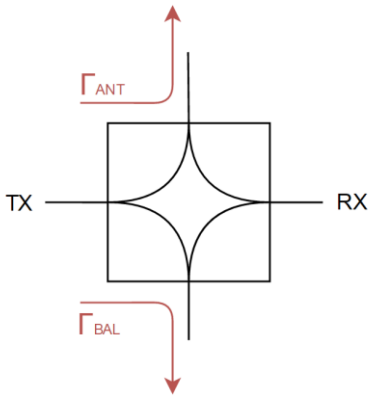

Figure 20. *Hybrid junction with balancing and antenna frequency-dependent reflection coefficients.*

In order to understand the accuracy requirements in terms of balancing operation, let's define ΔΓ as the reflection coefficient squared error.

$$\Delta\Gamma = |\Gamma_{ANT}(\omega) - \Gamma_{BAL}(\omega)|^2 \tag{21}$$

Figure 21 illustrates the variation in the isolation performance versus the quantity ΔΓ. Considering the symmetric case, in order to achieve isolation performance higher than 40 dB, ΔΓ has to be lower than $3 \cdot 10^{-4}$. This imposes high accuracy requirements within the controlling of the balancing impedance such that it reflects the antenna impedance as closely as possible. This directly impacts on the level of TX-RX isolation, and hence the level of SI suppression in a FD radio unit.

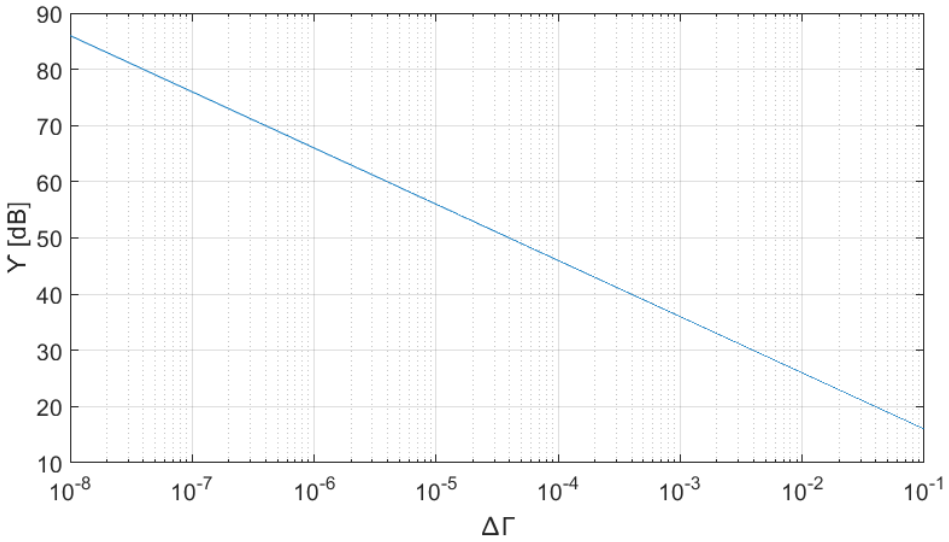

Figure 21. *Symmetric hybrid junction isolation performance variation.*

3.3 Hybrid Junction Topologies

Hybrid junctions can be classified in two different topologies basing on the construction technology. Those topology are transformer-based and microstrip-based hybrid junctions. Hybrid junction transformer-based topologies are the most widely used which include auto-transformer [14], center-tapped transformer [15] and differential hybrid transformer [34]. In the literature is possible to find EBD implementations integrating the aforementioned transformer topologies. Those are reported in Figure 22.

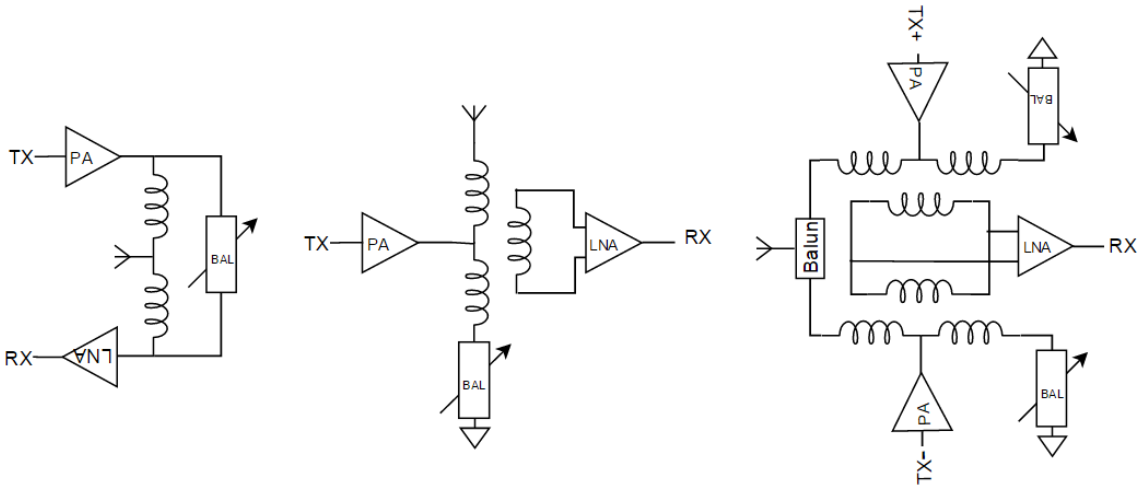

a. Auto-transformer b. Center-tapped transformer c. Differential hybrid transformer

Figure 22. *EBD hybrid junction implementations: Auto-transformer (a), Center-tapped transformer (b), Differential hybrid transformer (c).*

Each configuration has its own drawbacks and advantages, such that a proper choice is based on a trade-off between insertion loss, common mode isolation and occupied area (death area). Figure 22.a shows an auto-transformer which is the simplest hybrid junction implementation. It provides the best theoretical insertion loss and at the same time the minimum death area. Besides that, this topology can't provide any kind of common mode isolation between TX and RX ports decreasing the isolation performances. Moreover, a possible mismatching between the antenna and the balancing impedances can rise in a small DC-voltage offset at the input of the LNA port which can affect the system performances. Figure 22.b shows the center-tapped transformer configuration. Within this implementation TX and RX ports are electrically separated, but magnetically coupled through the transformer winding. Considering the working principle of a center-tapped transformers [32], that involves in a better common mode isolation. The extra winding requires extra area and it increases the RX insertion losses. This is due to the intrinsically resistance of the metal substrate and the flux leakage between the two inductances of the first winding. Also, since the transformer coupling coefficient cannot be ideal, this will add even more losses. The third implementation uses two hybrid transformers in a bridge configuration. This configuration exhibits very high common mode isolation, but both TX and RX insertion losses increase due to the transformers related losses. Moreover, this configuration requires to double the area, which can be a problem for on-chip implementations and a

balun is needed to connect the antenna. Furthermore, since the balun is a passive device whose typical insertion loss is around 1dB, this will increase the insertion loss.
Thus, the choice for the right topology is based on the specific application requirements and implementation challenges. First of all the TX output power is determinant for the topology choice and the required common mode isolation performance. Considering the three different configurations represented in Figure 22, the RX balanced line provide the best TX-RX isolation performances in terms of isolation bandwidth with high input power level. Differently, in the hybrid autotransformer case, a large voltage drop across the TX and RX port can induce large inductive current which creates an additional voltage across the balancing network. This creates a phase shift effect that limits the isolation bandwidth of the duplexer [24].
Microstrip-based hybrid junction topology includes 90° or 180° hybrid couplers [15], and coupled line hybrid junction [16]. Generally, 90° or 180° hybrid couplers cannot provide high isolation for wideband signal and being non-differential devices any kind of common mode isolation exists between TX and RX ports. A recent implementation of a coupled line hybrid junction [16] using edge coupled lines can achieve high isolation performance for wideband signal. This implementation is deeply analyzed in the next subsection as a part of this thesis work.

3.3.1 Directional Coupled Line Hybrid Junction

Figure 23 illustrates the coupled line hybrid junction. It uses the electrical balance principle to achieve high isolation. Indeed, electrical balance exploits symmetry of the network which makes it independent from the frequency, resulting in high isolation bandwidth [16].

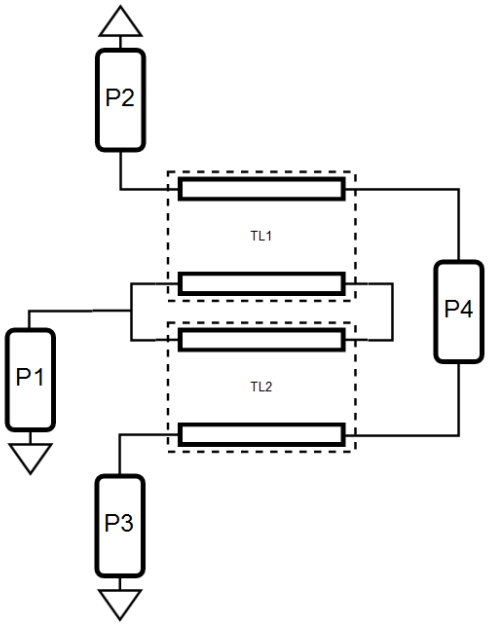

Figure 23. *Coupled Line Hybrid Junction schematic.*

The coupled line hybrid junction is a passive four ports device integrating two coupled line directional coupler TL1 and TL2 with high even mode impedance. Those are realized with

edge coupled line quarter wavelength transformers. The working principle can be explained using different stimulus at each port and applying the superposition.
Figure 24 shows the case where a stimulus is applied at port P1. The network appears symmetric with respect to its horizontal axes. Therefore, port P4 results isolated from the rest of the circuit because its terminations are equipotential ($V_A = V_B$). Both transmission lines TL1 and TL2 can be considered short-circuited at their other ends. This involves in port P1 connected to the parallel combination of port P2 and P3.

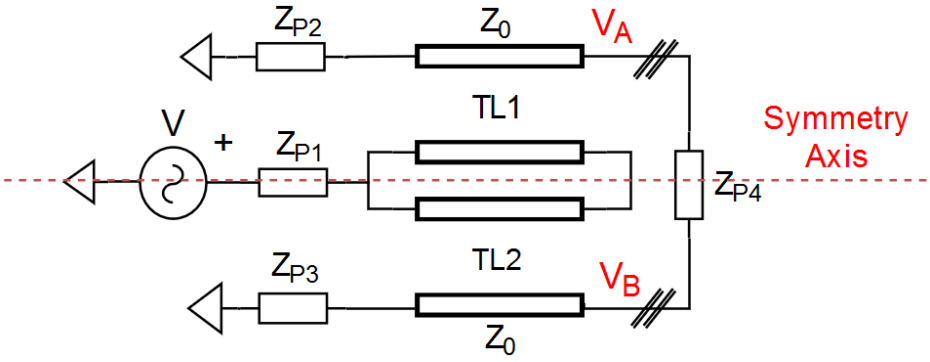

Figure 24. *Equivalent Circuit when the stimulus is applied at port P1.*

Even-Odd analysis [44] is necessary to understand how the circuit behave if a stimulus is applied at port P2. Even-mode analysis imposes equal sign signals to be applied at port P2 and P3 resulting then in the even-response, as depicted in Figure 25. Here, no current can flow along the horizontal axis because the two generators impose the same potential. The horizontal axis is the so called magnetic wall.

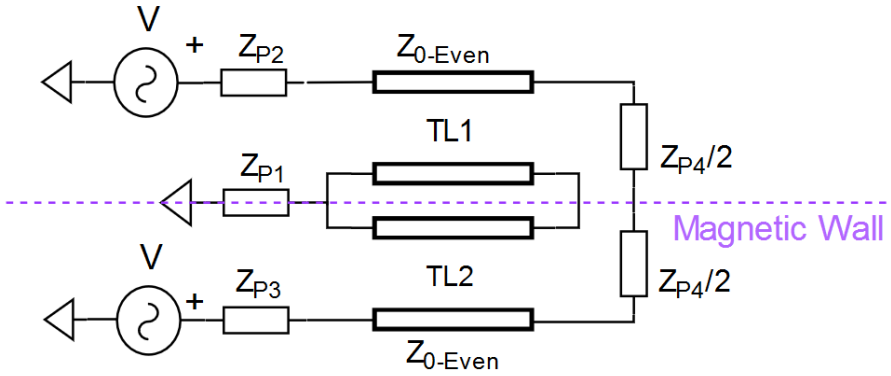

Figure 25. *Equivalent circuit for the even-mode analysis.*

In the odd-mode analysis, signal are applied to port P2 and P3 with 180° phase shift resulting then in the odd-mode response. Here, again the circuit results symmetric with respect to its horizontal axis. Thus, a virtual ground appears in the middle of port P4 such that is possible to equally split the port load as depicted in Figure 26. In this case, just odd mode current can flow in TL1 and TL2 because they are characterized by high even mode impedance. In this case the horizontal axis is called electric wall.

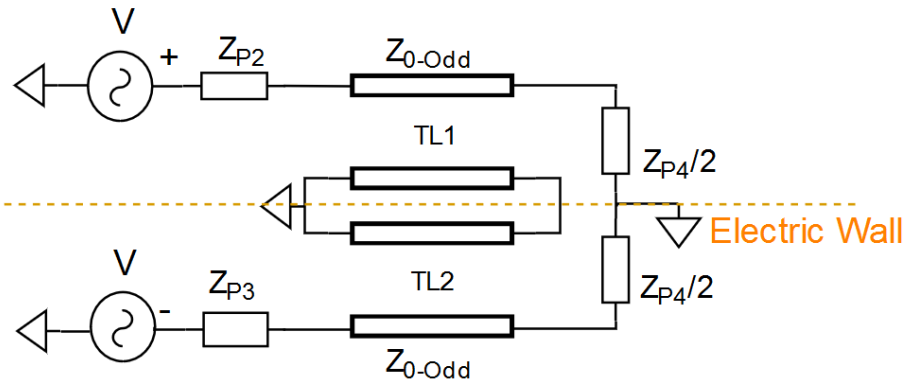

Figure 26. *Equivalent circuit for the odd-mode analysis.*

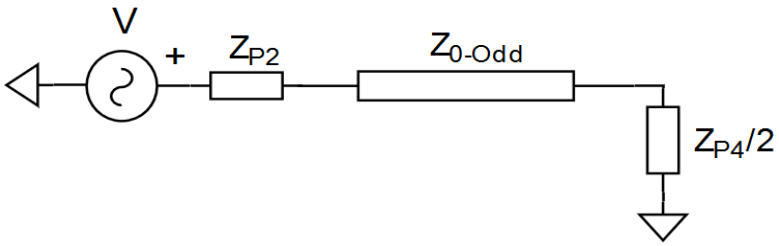

Figure 27. *Odd-mode simplified circuit.*

For the odd-mode analysis, the circuit can be simplified to the one represented in Figure 27, where the impedance seen by port P2 and P3 can expressed according to the relation that describes the quarter wavelength transformer [44]. If the following condition is satisfied no reflection occur at port P2 and P3.

$$Z_{P2} = Z_{P3} = \frac{2Z_{O-Odd}^2}{Z_{P4}} \tag{22}$$

The final circuit response is given by the superposition between odd and even mode responses. This shows that the port sets P1-P4 and P2-P3 are electrically isolated. Port P2 and P3 exhibits 90° phase shift with respect to port P4. Furthermore, the power entering at each port is equally split between the coupled ports. Therefore the scattering matrix can be expressed as following

$$[S] = \frac{\sqrt{2}}{2}\begin{bmatrix} 0 & 1 & 1 & 0 \\ 1 & 0 & 0 & -j \\ 1 & 0 & 0 & j \\ 0 & -j & j & 0 \end{bmatrix} \tag{23}$$

The isolation between P1 and P4 depends on two factors which are the impedance mismatching between port P2 and P3 and the length mismatching between the two transmission line TL1 and TL2. Any kind of mismatch can destroy the symmetry reducing then the overall isolation performance.

3.4 Antenna Tuning Unit

The antenna tuning unit (ATU) is an automatic impedance matching network which is commonly inserted between PA and antenna. ATU have been extensively used in radio communication technologies to increase transfer power efficiency and the device frequency tunability. ATU's design guidelines are well reported in [36] and [37]. Most of the ATU implementations are realized with different technologies including varactors diodes, binary switching capacitor banks and inductor arrays. In [20] a narrowband matching network realized with a Pi-network is able to achieve between 20 dB and 30 dB of return loss. An electronically controlled ATU for handheld devices integrating an automatic matching system is reported in [19]. The ATU structure is a Pi Network where variable capacitors are implemented with a capacitor banks controlled by switching p-i-n diode. Variable inductors are implemented using an equivalent circuit integrating two quarter wavelength transformers and a capacitor bank controlled in the same way. Experimental tests show at least 15 dB of return loss at the ATU port considering antenna impedance perturbations. Furthermore, the prototype performs reasonably well with different antennas and other frequencies outside the design bandwidth [19].
The ATU is also an optional stage that can be adopted in the EBD framework. In the existing literature, integrating such a unit and its benefits are discussed at principal level, i.e., in [15] and [18] but no existing real EBD prototype with ATU involved has so far been reported. This is one specific contribution of this thesis work. In general, antenna impedance can be subject to substantial variations due to the environmental effects and user interactions, in particular in case of handheld devices [23]. The purpose of ATU is to be able to provide dynamically controlled impedance matching exploiting the complex conjugate matching domain theory [17], while also reducing the range of antenna impedances seen by the duplexer. One central aspect behind the ATU is to also reduce the RX-TX path losses under antenna mismatches and to compress the range of variations of the antenna impedance in the center of the Smith Chart, thus simplifying the balancing operation and adding robustness against environmental changes and user interactions. This is very essential since as reported in [18], the balancing impedance network is typically able to track the antenna impedance variations with high accuracy around the center of the Smith Chart, while the accuracy is lower in other areas. One common implementation structure of ATU [19] is shown in Figure 28, which contains a Pi-network with variable capacitors and inductors.

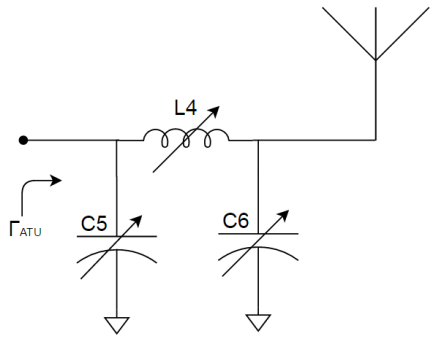

Figure 28. *An example circuit structure of an antenna tuning unit (ATU).*

3.5 Balancing Impedance

The balancing impedance is generally an electronically-controlled multi-stage Pi-network able to mimic the antenna impedance. Therefore, by controlling the balancing impedance such that it is equal to the antenna impedance the duplexer isolate TX and RX [9]. Typically, the network complexity defines the ability of the balancing impedance to follow and track the antenna impedance variations over a specific frequency band. The balancing impedance needs to fit some requirements such that it has to cover a wide range of impedance to track perturbations of the antenna impedance. Secondly, it should tolerate high power level and at the same time it has to be highly linear as any intermodulation products on the antenna side have to be balanced on the balancing side [34]. Finally, the balancing impedance needs to have high resolution, which means that it has to be capable of reproducing the antenna impedance with high accuracy.
Different topologies of balancing impedance have been reported in the literature. Figure 29 illustrates two different balancing topologies in a FD scenario, a fairly simple single-pole and a more advanced multi-pole Pi-network.

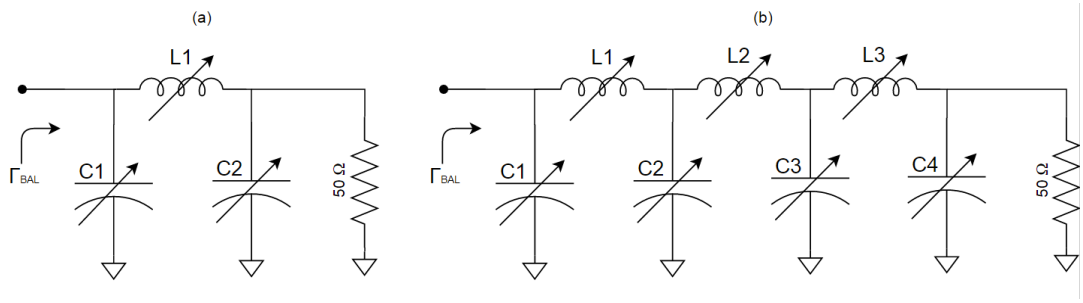

Figure 29. *Two alternative balancing network topologies; (a) single pole Pi network, (b) triple pole Pi network.*

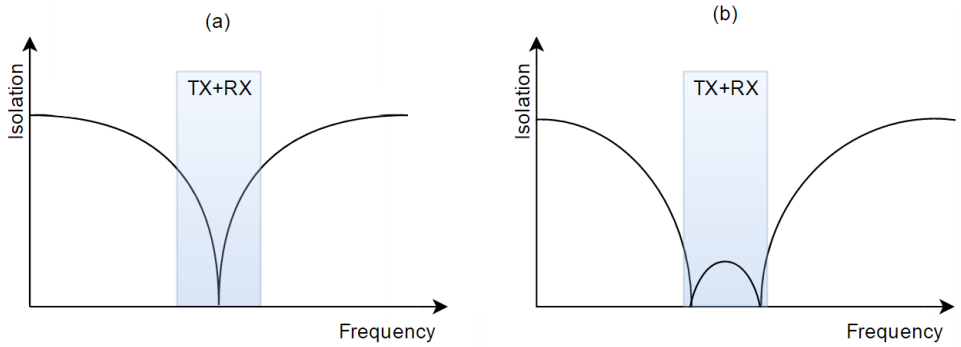

Figure 30. *Typical TX-RX isolation characteristics versus frequency with (a) single-pole and (b) triple-pole Pi balancing networks.*

These networks allows to control the magnitude and phase response characteristics of $\Gamma_{BAL}(\omega)$, such that they can mimic the frequency-dependent antenna characteristic $\Gamma_{ANT}(\omega)$. Therefore, the isolation bandwidth performance are dictated by the ability of $\Gamma_{BAL}(\omega)$ to match $\Gamma_{ANT}(\omega)$ in all its frequency domain.
Figure 30 describes the typical isolation curves in EBD in a FD scenario for the two alternative balancing topologies. Simple single-pole network can be controlled just for one frequency such that it is possible to insert a single notch at the balancing frequency at which $\Gamma_{ANT}(\omega) \approx$

$\Gamma_{BAL}(\omega)$ with high accuracy. High isolation performance can be achieved for a narrowband signal which is typically around 60-70 dB for 5 MHz instantaneous signal bandwidth [14]-[12]-[34]. Multiple stage Pi-networks allow generally more accurate control of the magnitude and phase response characteristics of $\Gamma_{BAL}(\omega)$, thus being able to better reproduce and track the characteristics of $\Gamma_{ANT}(\omega)$, especially over wider instantaneous bandwidths. This kind of networks substantially increase the isolation bandwidth provided by the EBD, by fitting two poles inside the instantaneous bandwidth, reducing the SI level with wider bandwidth waveforms.

3.5.1 Isolation VS Bandwidth

Adopting above kinds of more complex balancing networks in EBDs exhibit better isolation performance but are also often difficult to control. In [9] and [13], an optimization technique is used to maximize the isolation across the bandwidth of interest by minimizing (21) which represents the discrepancy between the antenna and the balancing impedance reflection coefficients. This leads to a minimum mean square error (MMSE) problem that can be expressed as follows

$$\min_{[C_1, C_4]; [L_1, L_3]} \frac{1}{B} \int_{f_1}^{f_2} \Delta\Gamma(f)\, df \tag{24}$$

where f_1 and f_2 are the two cut-off frequencies, B is the bandwidth of interest, the terms C_i and L_j are the capacitors and inductors values for the balancing impedance. The TX-RX isolation simulation result for a triple-pole Pi balancing network is reported in Figure 31. It illustrates the variation of the isolation performance when a MMSE tuning algorithm is applied. This enhance again one the main isolation challenge in any EBD system, in particular from the emerging wideband radio communication systems perspective.

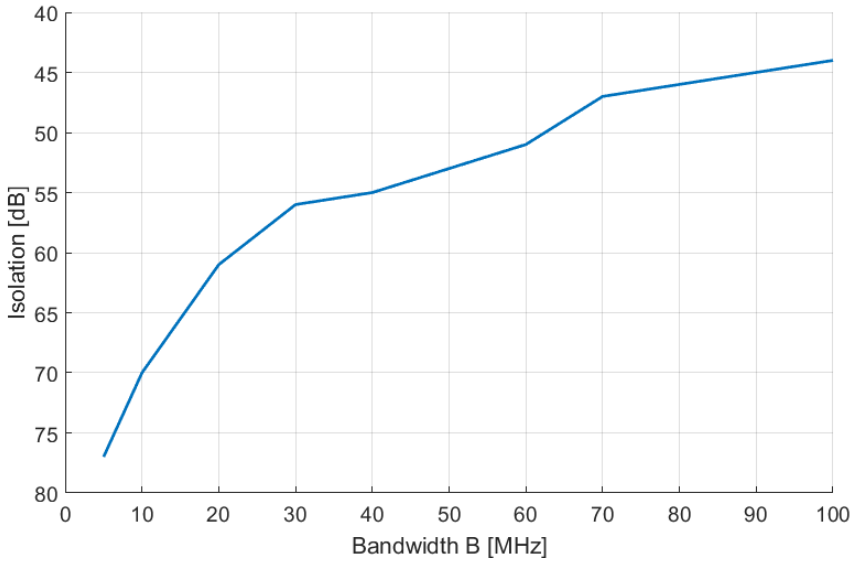

Figure 31. *TX-RX isolation simulation results in function of the bandwidth. This results is presented in [9] considering MMSE.*

However, no online or adaptive control system knows how to carry out the MMSE minimization in a real device, and potentially in a sample adaptive manner, was described.
Moreover, considering also the potential antenna impedance variations due to the local electromagnetic environment as well as user interactions in consumer devices, the balancing impedance has to be generally adaptive to cover the whole antenna impedance balancing domain [9].

3.6 Tunable Inductors

Both the ATU and the balancing impedance are later realized with passive tunable components, more specifically variable shunt capacitors and series inductors. Lumped tunable series inductor are difficult to implement, and they are often realized using only shunt elements and particular types of transmission lines. The Kuroda identities [44] can be used for conversion of this form, but another possibility is to use admittance inverters (J-inverters) [44]. Those inverters substantially invert the load admittance such that a series element can be transformed into shunt one. Figure 32 shows the admittance inverter.

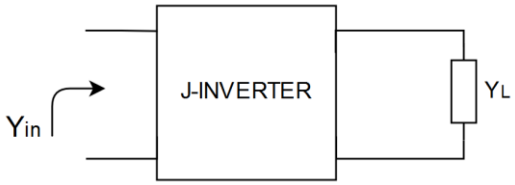

Figure 32. *Admittance inverter.*

The input admittance (Y_{in}) depend on the J-inverter characteristic admittance (J_o) and the load admittance (Y_L) as following

$$Y_{in} = \frac{{J_0}^2}{Y_L} \tag{25}$$

Therefore, as reported in [19], an inductors can be realized combining two admittance inverters and one capacitor as depicted in Figure 33.

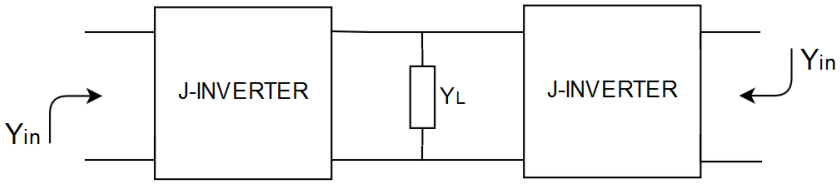

Figure 33. *Variable inductor equivalent circuit*

Thus, considering a the reactance of a single capacitor ($Y_{C_{eq}}$) instead of Y_L, the input impedance (Z_{in}) can be expressed as following

$$Z_{in} = \left(\frac{{J_0}^2}{Y_{C_{eq}}}\right)^{-1} = \left(\frac{1}{j\omega C_{eq} \cdot {Z_0}^2}\right)^{-1} = j\omega C_{eq} {Z_0}^2$$

Therefore, the equivalent inductance L_{eq} can be expressed considering its equivalent capacitance C_{eq} and the J-inverter characteristic impedance [19].

$$L_{eq} = C_{eq} \cdot Z_0^2 \tag{26}$$

Admittance inverters are commonly implemented using quarter wavelength transformers, which length (l) depends on the following equation

$$l = \frac{\lambda}{4} = \frac{c}{4f\sqrt{\varepsilon_{r,eff}}} \tag{27}$$

where f is working frequency, c is $3 \cdot 10^8\ m/s$, and $\varepsilon_{r,eff}$ is the relative effective dielectric constant of the transmission line.
In conclusion, an inductor can be implemented using an equivalent circuit integrating two J-inverters and a capacitor. In order to implement a tunable inductor a variable shunt capacitor is needed between the two J-inverters.

3.7 Balancing Operation: Tuning Algorithms

In EBD the balancing impedance needs to be dynamically tuned in order to track the antenna impedance variations achieving high TX-RX isolation. The balancing impedance is often realized with N tunable elements. Considering each tunable component resolution ξ and values range Δ, the number of possible combinations M resulting in the balancing operation is equal to

$$M = \left(\frac{\Delta}{\xi}\right)^N \tag{28}$$

This yields in an N-dimensional optimization problem where the optimum combination between all the parameters need to be find in an N dimensional space. Optimization algorithms and techniques have been extensively used to solve N-dimensional optimization problems. In those algorithms an object-function is defined to model the optimization challenge finding then the best set of parameters. Those algorithms can be classified in derivatives-based (or gradient-based) optimization techniques and derivative-free (or derivative-less) optimization technique. The first ones utilize the derivatives of the object function to find the optimum point, while the second ones look at the algorithms for optimization problems where derivatives information is not available because the object function is not differentiable, the derivative is not available or

the derivative is just too expensive to compute [42]. In this thesis work two different optimization algorithms are used to tune the EBD. Subsection 3.7.1 explains the Dithered Linear Search algorithm, while subsection 3.7.2 provides a general overview of the Simplex Method.

3.7.1 Dithered Linear Search

The Dithered Linear Search (DLS) is a gradient based optimization algorithm that have been widely used in analog filter parameters adaptation [21]. The algorithm aims to solve the so called "black-box" optimization problem, in systems where multiple inputs define a single system output. In black-box models no system's internal states information is available. Thus, its working principle is basically based on the change or changes that are made to the model's parameters and a resulting effect is observed at the output port.
DLS technique does not require any knowledge about the system's internal states and the system's parameters (weights) may be adapted simultaneously and independently of one another [21]. In order to explain the algorithm concept the analog filter adaptation challenge is considered. That consists in adjusting the filter's parameters according to a cost-function. Adaptive filters are often required for applications where some parameters are not known a priori. In this case a closed loop system allows to tune the adaptive filter parameters exploiting the feedback information to refine the system's transfer function. The dither term refers to a signal with small amplitude and zero mean that is injected in the system perturbing the weights [21].

$$w_i'(k) = w_i(k) + \delta_i(k) \tag{29}$$

$$E\{\delta_i(k)\} = 0 \tag{30}$$

where $w_i(k)$ and $w_i'(k)$ are the current and the perturbed weights respectively and $\delta_i(k)$ represents the dithered signal. The DLS algorithm makes perturbations to the filter parameters correlating then the perturbations with changes in the output signal. These correlations are integrated to derive a gradient vector, which is then used to calculate the magnitude and direction in which to vary the system's parameters. Figure 34 shows the DLS block diagram and its straightforward hardware implementation [21].

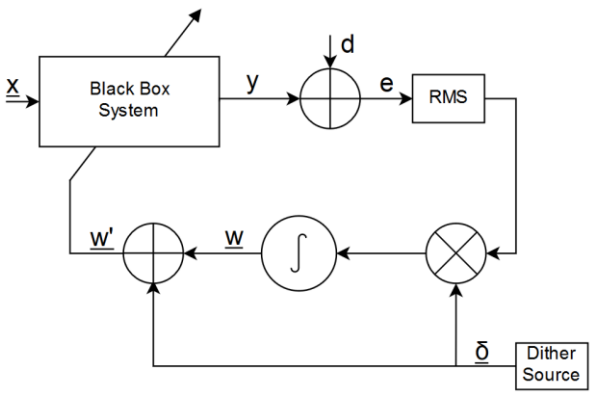

Figure 34. *Block diagram of the DLS for a general black box model [21].*

where $\underline{x}$ and y are the system's inputs and output respectively, d is the reference signal and e represents the error. The optimum system's weights vector is found using the following gradient-based mathematical relation as expressed in [21].

$$w_i(k+1) = w_i(k) - \frac{\widehat{\partial \varepsilon}}{\partial w_i} \tag{31}$$

The gradient estimate is given by,

$$\frac{\widehat{\partial \varepsilon}}{\partial w_i} = \frac{\mu}{\sigma^2} \cdot \delta_i(k) \cdot e^2(k) \tag{32}$$

where μ represents the step-size (learning rate) and σ^2 is the variance of the dithered signal. One other version of the DLS called DLS-BLOCK determines the gradient averaging L data samples continuously such that

$$\frac{\widehat{\partial \varepsilon}}{\partial w_i} = \frac{1}{L} \sum_{k=l}^{l+L} \left(\frac{\delta_i(k) \cdot e^2}{\sigma^2} \right) \tag{33}$$

The theoretical performance of the DLS and DLS-Block are the same, but the block implementation is practically more stable if compared to the first one.

3.7.2 Downhill Simplex Method

The concept of a "Simplex" and simplex vertices is generally referring to a certain geometric figure composed of $n+1$ corner points (or vertices) in an n dimensional space [22]. All the vertices are interconnected with line segments, polygonal faces, etc. In a two dimensional space the simplex is a simple triangle while for a three dimensional space is a tetrahedron.
For multidimensional optimization problem, the algorithm is initialized with a starting guess, that is, an n-vector of independent variables. The object-function is then evaluated at the $n+1$ vertices and the simplex is progressively and iteratively geometrically deformed through reflection, expansion and multiple contraction operations as described in [22]. This leads to the converge to the optimal solution, where each simplex corner is updated following relation

$$\underline{P_i} = \underline{P_0} + \lambda \cdot \underline{u_i} \tag{34}$$

Where $\underline{P_0}$ is the starting point or initial guess, $\underline{P_i}$ is the predicted optimal point, $\underline{u_i}$ are the n unit vectors and λ is a constant. More details about the algorithm are provided in [22].

3.8 EBD: State of the Arts

Several different prototypes of EBD have been developed in the recent years. They can be differently classified for the construction technology. Discrete duplexers are nowadays obsolete and almost all of them are implemented on a chip through a silicon process. However, discrete EBD are obviously more accessible and easy to fabricate for testing purposes. Recent works aim to develop duplexers for FD, but still there are a relevant number of existing implementations for FDD applications.

An EBD CMOS prototype operating in FD scenario is presented in [11], including a Wireless open-Access Research radio Platform (WARP), a commercial planar inverted-F antenna (PIFA). The prototype operates in the IEEE802.11 channel at 2.4 GHz ISM band. A simple balancing network realized with a variable resistor in parallel with a capacitor is tuned using an intelligent tuning algorithm. The algorithm uses machine learning techniques to model, estimate and control the balancing impedance. The prototype achieves an average of 50 dB of TX-RX isolation across 20 MHz signal instantaneous bandwidth with different environmental scenarios such as user-antenna interactions, presence of reflectors and antenna movements. The prototype exhibits an IL_{TX} of 3.4 dB.

An alternative implementation of discrete EBD can be found in [16]. The prototype is designed to work in a FD scenario for wideband applications. It integrates edge coupled lines directional coupler and a balun to realize the hybrid junction. The duplexer is realized using microstrip and coplanar line technology and it doesn't integrated any kind of balancing impedance, but just a simple 50 Ω resistor. The overall isolation performance swings between 31 and 36 dB in the 2.3-3 GHz frequency range. The TX and RX insertion loss are roughly 4 dB.

In [12]-[34] a dual-band EBD is implemented on a 65-nm CMOS process occupying 2.2 mm^2. It integrates a differential hybrid transformer as depicted in Figure 22.c and a balancing impedance realized with a differential triple-pole network. The variable capacitor are implemented using high-voltages switched capacitor banks, while transformers are used to implement fixed inductor. A genetic algorithm for global optimization is used to tune the balancing impedance. The EBD is able to achieve more than 50 dB of isolation for both TX and RX band. However, the high isolation performance is justified by the 6 MHz instantaneous signal bandwidth and the overall isolation decrease already to 45 dB for a 10 MHz signal. The prototype shows an IL_{TX} less than 3.8 dB and IL_{RX} equal to 4 dB, which are roughly 1 dB more than the ideal symmetric condition. Experimental tests with a 64-QAM LTE signal with 5 MHz bandwidth and central frequency of 1.95 GHz show an IIP_3 of -4.6 dBm and IP_{1dB} of -21 dBm exhibiting high level of linearity.

Another interesting work is reported in [35], where the EBD is realized with a hybrid transformer and a balancing network fabricated in the 0.18µm RF SOI CMOS process occupying 1.75 mm^2. The prototype is designed to work between 1.9 and 2.2 GHz. The balancing impedance is implemented with four arrays of switched capacitors and two fixed inductors. The duplexer achieves more than 50 dB of isolation with narrowband signal and using an external impedance tuner. The measured TX and RX insertion losses are 3.7 dB and 3.9 dB respectively. An interesting feature of this prototype is the high IIP_3 which is greater than +70 dBm.

Another prototype is reported in [10] where a hybrid transformed-based tunable differential duplexer is implemented in a 90-nm CMOS process occupying 0.6 mm^2. The EBD works in the 3G bands between 1.7 and 2.2 GHz. The balancing impedance is fabricated with a control voltage resistor in parallel with a voltage controlled capacitor. The prototype shows deep isolation peaks, because of its differential hybrid transformer. The TX-RX isolation performance is between 60-70 dB for the TX band and 40 dB for the RX band. The prototype shows IL_{TX} equal to 4.7 dB and an IIP_3 of -5.6 dB.

One more tunable integrated duplexer is presented in [14]. The EBD works between 1.5-2.5 GHz and it is implemented in a 40 nm CMOS process occupying 0.2 mm^2. An auto-transformer is used as hybrid junction and the balancing impedance is realized with a variable resistor in parallel with a capacitor. Isolation level of more than 50 dB in a bandwidth of 5 MHz is achieved by a proper impedance tuning. Two different versions of the EBD are tested skewing the auto-transformer. The TX and RX insertion losses are respectively 5.9 and 2.9 dB for the asymmetric autotransformer. In the symmetric case the TX and RX insertion losses are both 4.2 dB.

In [18]-[24] an EBD working in the frequency range 1.8-2.2 GHz is described. The prototype is realized in a 65 nm CMOS process occupying 0.2 mm^2. It integrates a center- tapped transformer and the balancing impedance is implemented with an array of switched resistor and capacitors. The isolation performance is greater than 55 dB for the TX band and 45 dB for the RX band. The EBD shows a TX insertion loss equal to 2.2 dB.

4. ELECTRICAL BALANCE DUPLEXER DESIGN AND IMPLEMENTATION

In this chapter a novel electrical balance is presented. All the important steps and the choices related to the design and implementation processes are described. The chapter starts showing the proposed duplexer architecture and design goals. Therefore, the topology choices for each components and the main design choices are reported for the hybrid junction, ATU and balancing impedance. After, the adaptive digital control system and the final tuning algorithm are described. The chapter ends with an overview of the final prototype.

4.1 Proposed architecture

The proposed EBD architecture consists in three key elements which are hybrid junction, balancing impedance circuit and antenna tuning unit (ATU). A simplified block diagram of the prototype is illustrated in Figure 35.

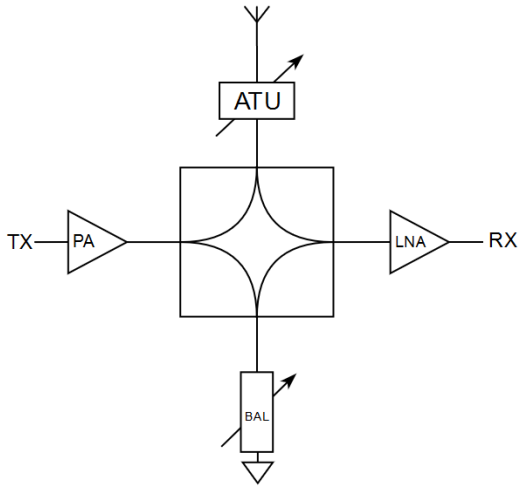

Figure 35. *Electrical balance duplexer with antenna tuning unit [15].*

The prototype implementation follows the one presented in [15]. The LNA is not included, since the primary goal of this work is to evaluate and demonstrate the isolation properties of the EBD in a FD radio scenario, such that the SI is measured already prior to the LNA. This is the point where the SI characterization is done also in most previous works in the literature.
The project and the physical duplexer implementation has been carried out in Tampere University of Technology (TUT). Considering that no labs were equipped with ICs machinery and since IC design is not the focus of this thesis work, the prototype has been implemented using standard commercial off-the-shelf discrete components. This has obviously simplified the realization process, but at the same time it has imposed several constraints concerning the design choices.

4.2 Prototype Goals

The EBD prototype is designed to work at the 2.4 GHz ISM band, in particular at 2.4-2.48 GHz. ISM band operation itself is naturally motivated by the license-free operation, thus enabling flexible live measurements in real environments. Considering the recent radio communication standard and the reported EBD works, several prototype goals have been established.
In particular, the duplexer has to achieve high isolation performance for a wideband signal. Up to 80 MHz instantaneous bandwidth is pursued as it can facilitate carrier aggregation of several 20 MHz channels in both LTE-Advanced cellular mobile radio network as well as in IEEE 802.11ac WLAN/WiFi system. The duplexer has also to be capable of automatic tracking of time-varying antenna impedance characteristics in order to provide robustness against fast changes in the surrounding environment and against user interactions in a FD scenario. Moreover, TX and RX insertion losses have to be minimize. Table 1 presents the duplexer design goals summary.

DUPLEXER DESIGN GOALS		
Parameters		**Value**
Frequency Range[GHz]		2.4-2.48
Typology		FD
Max TX power[dBm]		20
$\boldsymbol{IL_{TX}}$**[dB]**		4
$\boldsymbol{IL_{RX}}$**[dB]**		4
$\boldsymbol{IIP_3}$**[dB]**	TX path	20
	RX path	0
TX-RX Isolation	Isolation[dB] $_{TX\text{-}RX}$	>40
	Ass. BW [MHz]	80
40 dB Isolation Bandwidth [MHz]		80
Technology		Discrete
Balancing Impedance Tuning Dimension		7
ATU Tuning Dimension		3
Area [mm^2**]**		PCB

Table 1. *Duplexer design goals*

4.3 Hybrid Junction Choice

Almost all of the recent EBD implementations are for small form factor realizations, where the duplexer is implemented on a chip. The hybrid junction is often realized with center-tapped transformers implemented as a multi-layer planar transformer. Specifics monolithic planar transformer RF IC design guidelines are well reported in the literature which are suitable for

small form factor design [25]-[26]. However, the following practical challenges have to be considered during the design and implementation phases.

- The majority of RF transformer design guidelines are for microscale transformers, where the metal trace width and the line spacing between the windings are in the order of 10-50 μm.

- A careful design of the transformer is required to ensure that the required performances are met and additionally parasitic effects due to the integration process have to be considered.

- In order to reduce the losses, the transformer has to be design with high coupling coefficient. Stacked transformers [25] provide the highest coupling coefficient, but the only way they can be realized is with high quality multi-metal layer materials.

- For reducing the input-output losses extra shunt capacitors need to be added to the transformer pins of each windings resulting then in a transformer tuning operation which makes the realization process even more challenging [25].

- Transformers have usually limited frequency ranges and they are suitable for small bandwidth applications.

Considering these practical challenges and the technology limits, the center-tapped transformer does not seem to be the best solution for the hybrid junction topology choice. The *printed circuit board* (PCB) etching process allows a minimum trace width of 0.2 mm that makes impossible the realization of micro-scale transformers. Thus, implementing a transformer with this line gap, would have decrease the coupling coefficient adding more losses. High quality RF metal substrates can reduce the losses, but at the same time they are quite expensive and they are not a suitable choice for testing purpose. Lumped center-tapped transformers are nowadays available in the market for specific frequency ranges starting from 0.01 to 1400 MHz [27]. The EBD is designed to work in the ISM band (2.4-2.48 GHz), so no lumped center-tapped transformer exists for this kind of application. These transformers are in fact commonly used in the RF-mixer, where they are directly embedded in the IC. Therefore, due to the design complexity, lack in the facilities and for time reasons the center-tapped transformer solution is discharged and a novel microstrip coupled line hybrid junction is chosen as the best candidate for this application.

4.4 Coupled Line Hybrid Junction Design

The design is strongly inspired by the one described in [16], but naturally adjusted and tailored to the specific application at hand and the targeted frequency range. The hybrid junction is implemented on a two layer FR4 board which is shown in Figure 36.

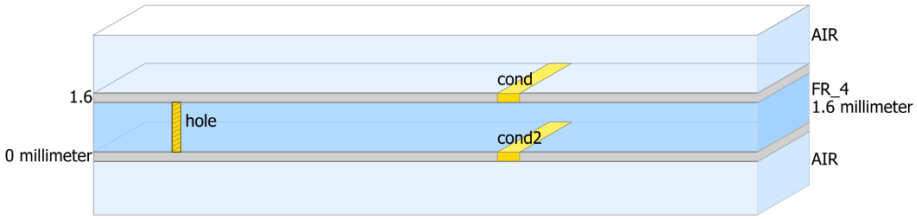

Figure 36. *PCB Substrate layers.*

The dielectric parameters are reported in Table 2. The hybrid junction is designed using the software ADS Momentum Microwave, which is a powerful 3D planar electromagnetic simulator suitable for passive circuit modeling and analysis. It uses frequency-domain Method of Moments (MoM) technology to accurately simulate complex electromagnetic effects including coupling and parasitic.

SUBSTRATE SPECS	
Thickness	1.6 mm
Relative effective dielectric constant	4.3
Relative permeability	1
Conductivity	$5{,}8 \cdot 10^6$S/m
Conductor thickness	35 µm
Dielectric loss tangent	0.02
Conductor surface rough	0 mm

Table 2. *Prototype FR4 substrate specification*

Considering the theoretical concepts explained in 3.2.2, the first design step consists a proper choice of each port impedance and power splitting ratio *r*. In order to satisfy (22), the directional line coupler odd impedance is chosen equal to 50 Ohm. This implies a very high even mode impedance. Then, considering (14), the impedance at each port is chosen to satisfy the bi-conjugancy condition. So, the impedance at ANT and BAL ports are chosen equal to 50Ω, while the impedance at the differential RX port results equal to 100 Ω. The impedance at TX port results equal to 25 Ω. The space gap between the two transmission lines is chosen equal to 0.2 mm according to the minimum allowed from the fabrication technology in order to maximize the coupling coefficient, reducing the losses. The circuit represented in Figure 23 is then modified merging together the two transmission lines TL1 and TL2 since they are equipotential surfaces. Furthermore, a quarter wavelength transformer is integrated matching the TX port impedance to the commercial standard 50 Ω. The length and the characteristic impedance of the quarter wavelength transformer are computed considering the central frequency as reported in [44]. Then the theoretical quarter-wavelength parameters are found using (25) and (27).

$$Z_o = \sqrt{z_{in} z_l} = \sqrt{50 \cdot 25} = 35.35\ \Omega$$

$$\frac{\lambda}{4} = \frac{c}{4f\sqrt{\varepsilon_{r,eff}}} = \frac{3 \cdot 10^8}{4 \cdot 2.44 \cdot 10^9 \cdot \sqrt{4.2}} = 14.9 \text{ mm}$$

In order to have equal losses in both TX and RX paths, *r* is chosen equal to one (symmetric condition). This means that the power is equally divided between the hybrid junction ports resulting in 3 dB loss for both TX and RX path. As suggested in [16] the length of the merged line is slightly shorted to compensate the extra capacitance added by the open circuit. In order to increase the even mode impedance the ground plane under the directional couplers is also removed. Differently from [16], no balun is adopted to avoid degrading the isolation performance. An hybrid 180º coupler (i.e., "rat race"-coupler) working at the 2.4 GHz ISM band is therefore designed to properly mix the differential ports in order to provide a single ended receiving port.
The layout with the dimensions and the 3D model of the microstrip directional coupler hybrid junction is shown in Figure 37 and Figure 40 respectively.

Dimension	Value[mm]
W1	3.1
W2	5.3
W3	3.1
W4	1.1
W5	2.54
S1	0.2

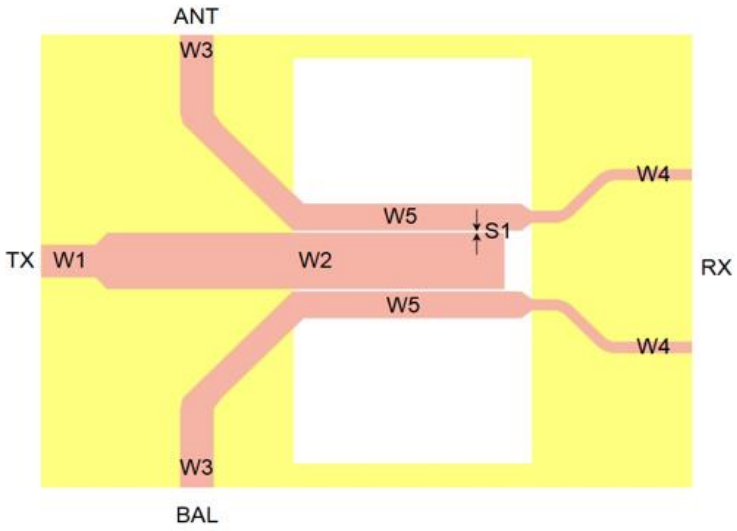

Figure 37. *On the left the geometry dimensions of the microstrip coupled line hybrid junction. On the right side the prototype layout. The yellow area represents the ground plane, the RF traces are pink.*

The conventional and proposed structure is simulated using ADS to calculate the scattering matrix over a frequency range 2-3 GHz. The simulation method is the momentum method (MoM) and the mesh is set equal to 100 cells/λ to provide accurate results. The theoretical equations described in sections 2.3 and 2.4 are then applied to compute the parameters. The optimization process then establishes the best trade-off between the overall TX-RX isolation, insertion losses, port return losses, CMRR and magnitude and phase imbalance, in particular

- The overall isolation between TX and RX port has to be maximized for the whole spectrum analysis.
- The insertion losses for both TX and RX paths have to be close to 3 dB.
- The return loss at each port needs to be lower than 10 dB. This condition implies impedance matching at each port.

- The CMRR has to be high as possible. A high value indicates more rejection in the common mode, which is desirable in a device that is receiving information in the differential portion of the signal. Around 30 dB of CMRR are typically required for differential device.
- The imbalance has to be as low as possible in order to keep the device electrically symmetric. This improves the isolation performance. The magnitude imbalance can be consider acceptable if it is lower than 1 dB, while the phase difference has to be close to 180º. Usually commercial devices present a phase imbalance difference of ±10º.

Figure 38 and Figure 39 shows the hybrid junction simulation results.

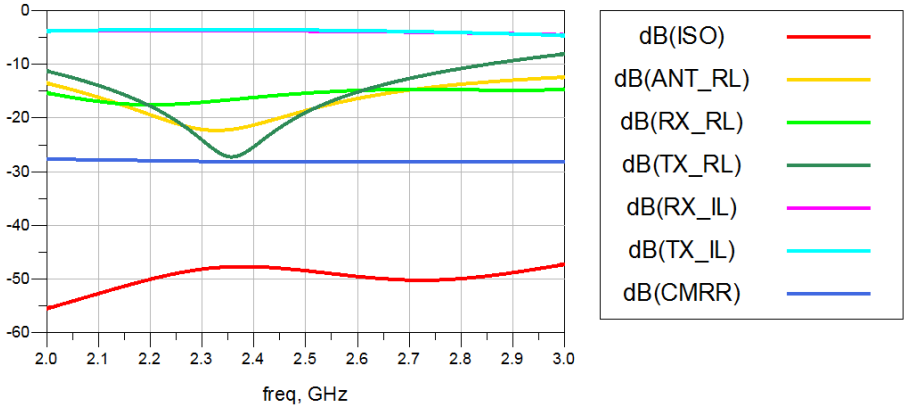

Figure 38. *Hybrid junction simulation results: TX-RX isolation (ISO), Port return losses (ANT_RL, TX_RL, RX_RL), common mode rejection ratio (CMRR), TX and RX insertion losses (TX_IL, RX_IL).*

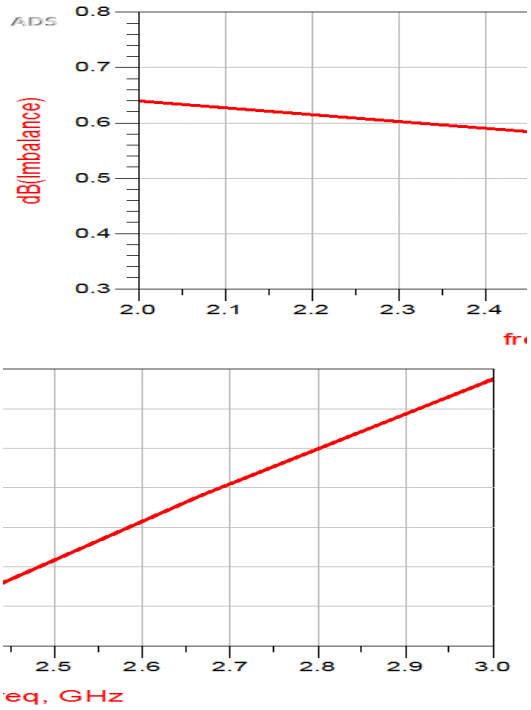

Figure 39. *Hybrid junction simulation results: magnitude and phase imbalance.*

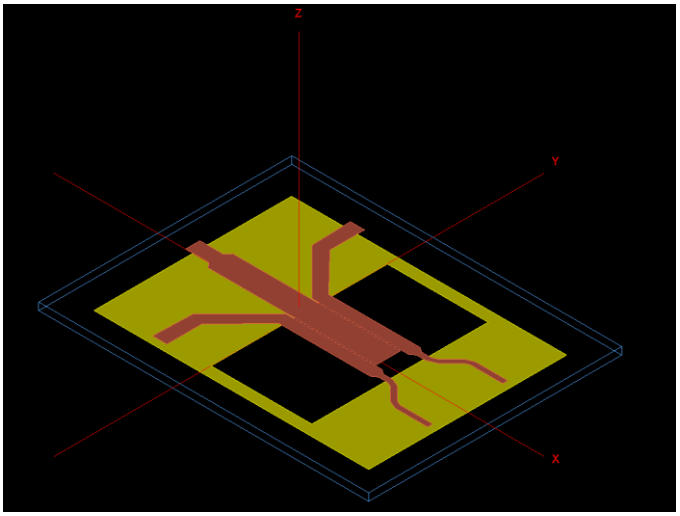

Figure 40. *3D model of the coupled line hybrid junction.*

The simulated results show that the coupled line hybrid junction prototype matches the design criteria. The simulation considers all the parasitic effects and the non-idealities of the dielectric substrate, so the expected result cannot be ideal. However, from Figure 38 is possible to note that the isolation fluctuates between 45 and 56 dB from 2 to 3 GHz. This result is promising and it represents the maximum isolation that the device is able to achieve in the whole frequency range with ANT and BAL ports terminating on a 50 Ω ideal resistor. The TX and RX insertion losses are respectively 3.6 dB and 3.7 dB at 2.44 GHz ISM central band frequency. The insertion losses are then close to the theoretical limit. All the ports exhibit less than 10 dB return loss. The TX return loss curve presents a notch slightly outside the ISM band, but in any case it is more than 15 dB for the bandwidth of interest. So, all ports are well matched. The CMRR oscillates between 25 and 28 dB, which is almost close to the targeted value. Finally, the amplitude imbalance is less than 1 dB, while the phase imbalance is less than 3° for the whole frequency range. In conclusion, the simulated results satisfy the design goals and guidelines, resulting in promising EBD isolation performance. Figure 41 shows the physical implementation of the coupled line hybrid junction prototype.

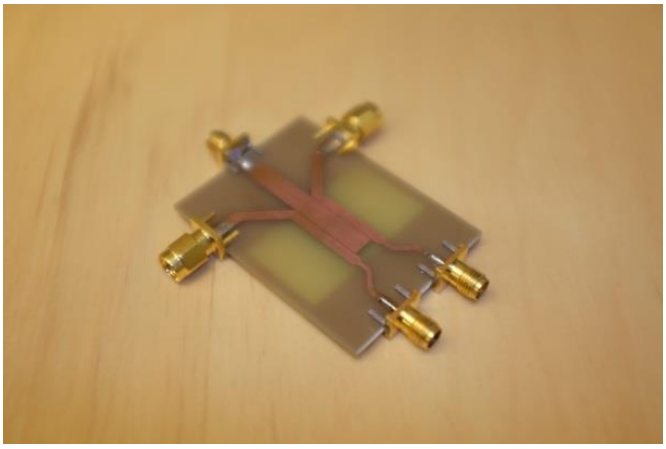

Figure 41. *Coupled line hybrid junction prototype.*

4.5 Tunable Components

The next sections introduce the design procedures for the ATU and the balancing impedance. In order to briefly understand how these two elements are implemented it is useful to present the elements that have been directly involved into the design process. Both the ATU and the balancing impedance are realized with variable shunt capacitors and series inductors. Variable inductors are realized combining two J-inverters and one variable capacitor as explained in section 3.6. The equivalent inductance can be expressed considering its equivalent capacitance and the J-inverter characteristic impedance using (26). Figure 42 shows the equivalent variable shut capacitor and series inductor realized with varactor diodes.

There are a lot of different tunable capacitors implemented with different tunable technologies such semiconductor varactors with switches, MEMS varactors, capacitors switched by PIN diode, capacitors switched by MEMS, tunable transmission lines and ferroelectric varactors. These components have their own advantages and disadvantages as reported in [20]. Considering this work, varactor diodes were chosen as the most appropriate solution for flexible demonstration purposes. This was based on the assumption that the typical RF transmit powers are limited to the range of say +20…+25dBm dBm (feasible TX power i.e. in WiFi and cellular user equipment, UE, devices), and the fact that the range of controllable capacitance variations is higher than those of many other components. On one side, varactors are non-linear devices, so this implies intermodulation distortion being created at the higher transmit powers. However, the capacitance variations can be easily realized and controlled by applying a proper biasing reverse voltage across the p-n junction. That makes the varactor diodes devices that are fairly easy to control in a precise manner. Hence, stemming from these arguments, varactor diodes were eventually chosen to realize variable capacitors and inductors, imposing then a constraint in the TX power levels to around +20 dBm or so.

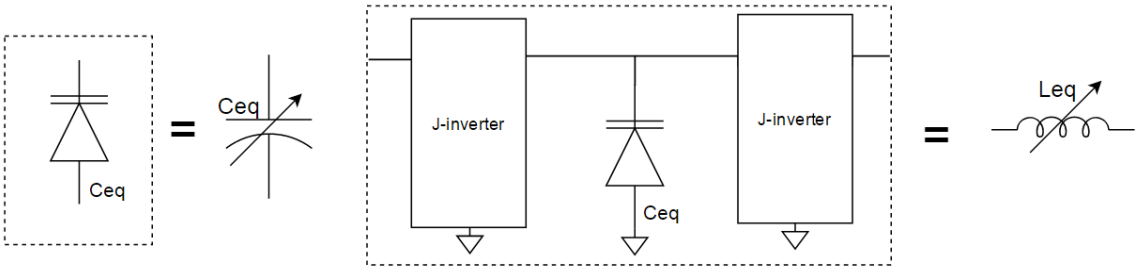

Figure 42. *Equivalent shunt capacitor and series inductor realized with varactors.*

4.6 ATU and Balancing Impedance Design and Implementation

Both the ATU and the balancing impedance are designed considering the adoption of realistic Cisco-based commercial antennas and associated device measurements in different scenarios.

Three common scenarios are chosen to characterize $\Gamma_{ANT}(\omega)$ in standard lab conditions, presence of metal reflectors, and antenna-user interactions, as will be explained more thoroughly Chapter 5.

4.6.1 Antenna Tuning Unit

The choice of inserting an ATU as a part of the prototype is due to three main motivations. First of all, an adaptive ATU provides robustness against fast environmental changes, secondly it simplifies the balancing operation in the EBD. Finally, in the literature there is no actual implementation of an EBD which includes an ATU, and all the related benefits are just theoretically discussed. So, for these reasons an ATU is designed for this specific application. The matching network is chosen according to the matching domain theory as explained in section 2.5. Figure 43 shows several different measurements of the magnitude of antenna input reflection coefficient (Γ_{in}) considering three different scenarios.

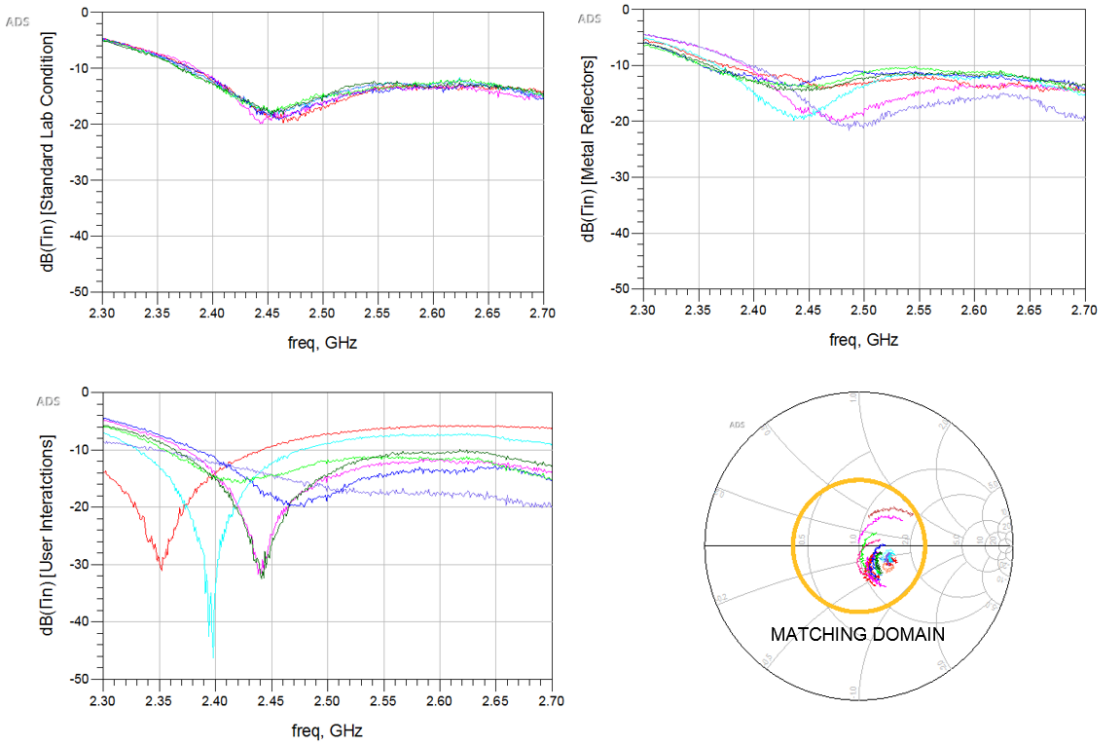

Figure 43. *Antenna input reflection coefficient (Γ_{in}) measurements for three different scenarios. The matching domain is depicted in the right corner for the frequency range 2.4-2.48 GHz.*

As it is possible to note from Figure 43 the antenna input reflection coefficient can be very different considering different scenarios. In standard laboratory conditions and metal reflectors cases, Γ_{in} results similar in its frequency characteristic. Different is the case of the user interactions, where strong reflections are created by the user hand moving around the antenna, changing the characteristic impedance, creating then a strong impedance mismatching. To design a narrow band impedance matching network, different topologies can be used: L-structure, Pi-structure, T-structure, or distributed components [20]. For these structures, the challenge is

to introduce tunability. It is well known that the L-structure cannot cover the whole Smith chart, while Pi and T structures provides better matching and tunability range in terms of frequency, covering more area in the Smith chart. Therefore, Pi-structure is selected to design the ATU. The ATU aims to dynamically transform the antenna impedance variations to 50 Ω input impedance. In order to do that, the antenna matching domain is then considered. The component ranges of the ATU are chosen to properly cover the complex conjugate matching domain. The equivalent capacitance ranges are defined by the varactor characteristic while the equivalent inductors are established using (26). The ATU is designed according to the schematic shown in Figure 28. The variable capacitors and inductors are realized with varactor diodes SMV1405-040LF and J-inverters using quarter wavelength transmission lines as shown in Figure 42. The ATU is designed providing the low insertion loss as possible. Figure 44 shows the ATU simulation results. The insertion loss result less than 0.7 dB in the ISM band. The impedance range seen by the duplexer (Γ_{ATU}) defines the EBD balancing domain resulting compressed in a VSWR circle of radius 1.5.

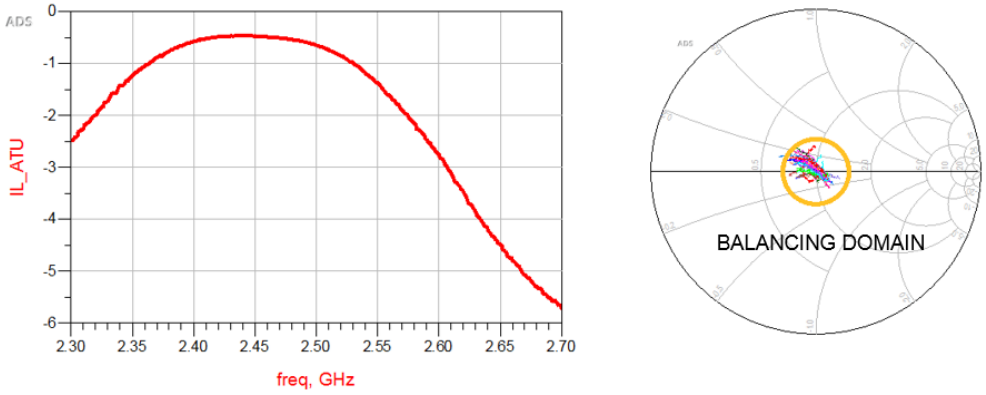

Figure 44. *ATU simulation results. On the left side the ATU insertion loss (IL_ATU), on the right side the balancing domain is reported for the frequency range 2.4-2.48 GHz.*

4.6.2 Balancing Impedance

The balancing impedance, on the other hand, builds on the multi-stage topology presented in Figure 29.b, hence exploiting all of its benefits. Variable capacitors and inductors are implemented using the same equivalent circuits as depicted in Figure 42. Substantially, the balancing impedance has to be designed in a way that the balancing reflection coefficient (Γ_{BAL}) has to match the ATU reflection coefficient variations (Γ_{ATU}) in all its balancing domain. Because of the wide capacitance tuning range of the adopted varactors, the balancing impedance exhibits very high dynamic range capable of covering the whole antenna balancing domain. Therefore high TX-RX isolation can be achieved.

4.7 Duplexer Isolation Performance: Simulation Results

The duplexer isolation performance is simulated with ADS before the implementation. The simulation setup is reported in Figure 45 including the hybrid junction, ATU and balancing

impedance equivalent models, real Cisco antenna measured data and an ideal balun to transform the differential RX port to a single ended.

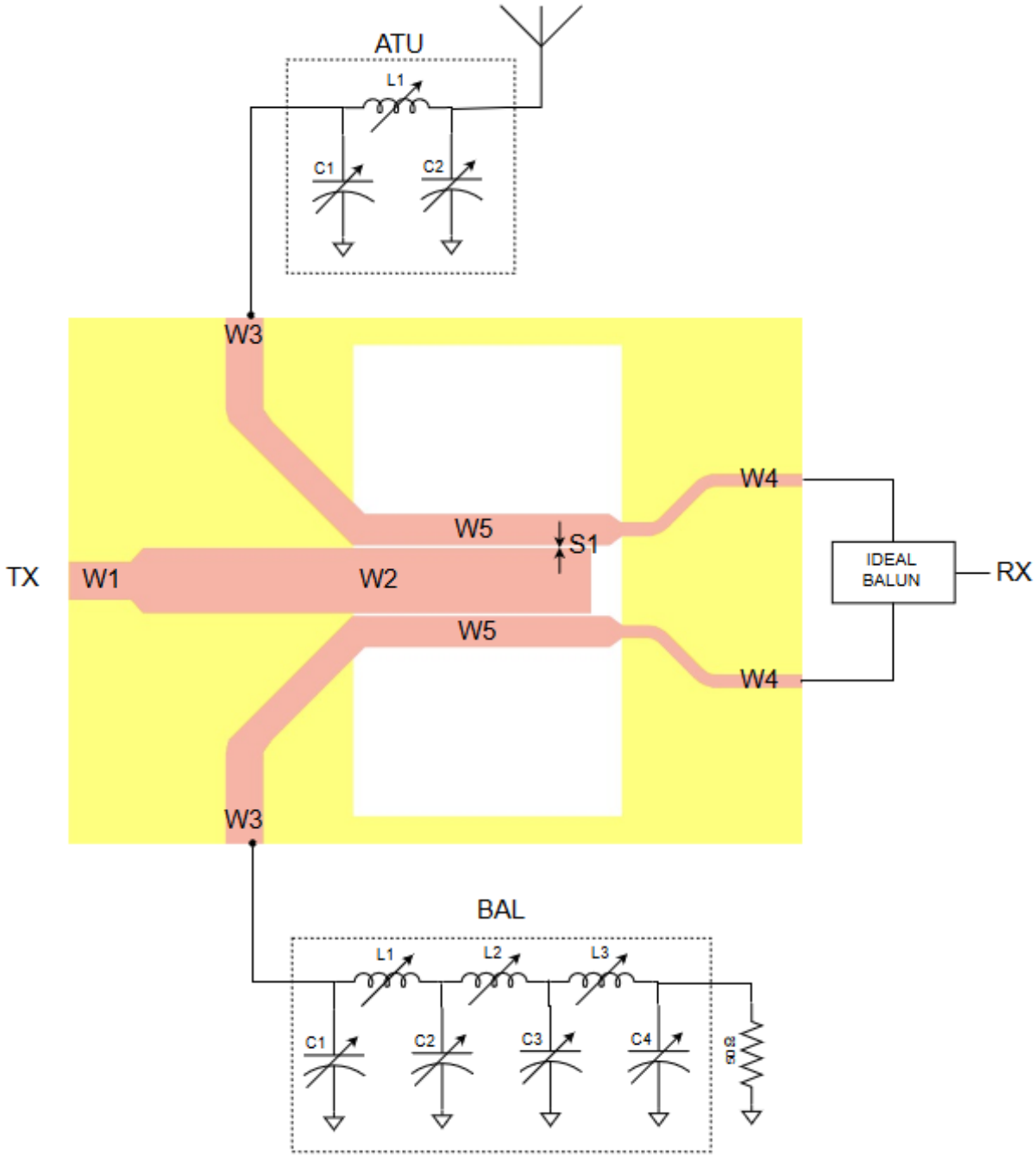

Figure 45. *Electrical balance duplexer simulation setup.*

The simulated TX-RX isolation performance are reported in Figure 46 considering the three different scenarios which are standard lab conditions (blue), presence of reflectors (purple) and antenna-user interaction (red). The isolation curves are obtained applying a MMSE approach finding the optimal varactor control voltage set to minimize (24). Therefore the isolation is given by the insertion loss between TX and RX path.

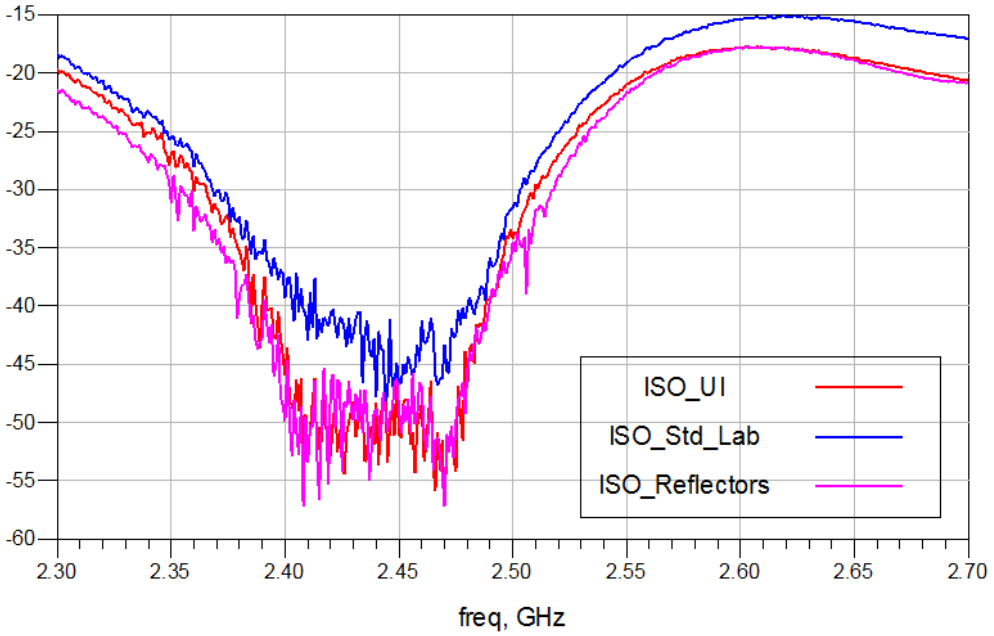

Figure 46. *TX-RX isolation performance simulation result. Three isolation curves are obtained: standard lab. conditions (blue), antenna-user interaction (red), presence of reflectors (purple).*

Figure 46 shows that the overall expected isolation performance are between 40 and 55 dB in the whole ISM Band (2.4-2.48 GHz) for the three different scenarios.

4.8 Adaptive Digital Control System

The overall digital control system builds on the general configuration depicted in Figure 47, where the prevailing instantaneous SI power is observed through the RX chain. Based on this observation, the varactor control voltages are then adjusted exploiting the feedback information. Two different optimization algorithms are used in parallel in order to realize high TX-RX isolation.

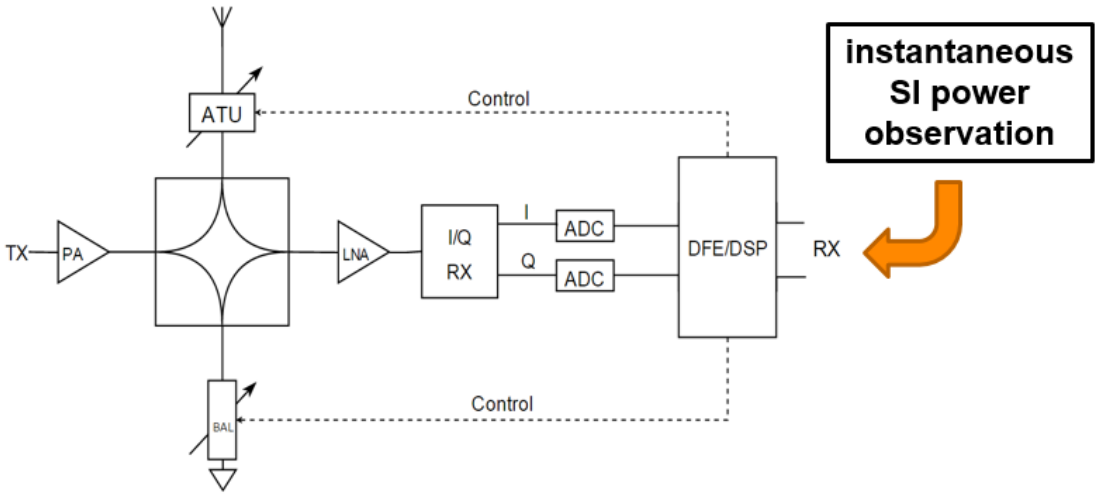

Figure 47. *Adaptive digital control system.*

Since also an ATU is adopted, the overall control system aims to find a proper set of control voltages such that $\Gamma_{ATU}(\omega) \approx \Gamma_{BAL}(\omega)$. In this demonstrator entity, the dithered linear search (DLS) algorithm and a multidimensional extension of the simplex method are combined to be able to tune both the ATU and the balancing impedance control voltages efficiently and accurately. Thus, the overall control system integrates together both gradient based and geometric based optimization techniques, in order to facilitate fast convergence in finding the global optimum. Considering the optimization complexity of the balancing network and the ATU, as a whole, yields a ten-dimensional minimization problem, where the ATU and the balancing impedance control voltages are all tuned together.
In the developed control system, the algorithm alternates the balancing impedance tuning and ATU tuning operations to balance the overall device. The balancing impedance weights are update using a slightly modified version of the DLS block expressed as

$$w_{k+1} = w_k - \mu \cdot \frac{1}{L} \sum_{k=l}^{l+L} [P_{SI}(w'_{k+1}) - P_{SI}(w_k)]^2 \cdot \delta_{k+1} \tag{35}$$

where w_{k+1} denotes the updated balancing control weight vector, w_k is the previous balancing control vector, μ is the learning step size, L represents the amount of averaging in the learning, $P_{SI}(w_k)$ refers to the observed instantaneous SI power under control weights w_k, and δ_{k+1} denotes the dithering signal vector implemented with Hadamard sequences in our control system. Furthermore, $P_{SI}(w'_{k+1})$ refers to the observed SI power with dithered control weights w'_{k+1}.
The control of the ATU, in turn, builds on the concept of a "Simplex" and simplex vertices which is generally referring to a certain geometric figure composed of $n+1$ corner points in an n dimensional space. The SI power is constantly monitored at the $n+1$ vertices of the prevailing simplex while the simplex is progressively and iteratively deformed and restructured moving towards the optimum point.
The overall digital control is implemented using a BeMicro FPGA board from Altera, which is connected to a host processor, using two DACs to get 10 different analog control voltages ranging from 0 to 3 V. An operational amplifier based buffer is also fabricated and inserted to amplify the control voltages to proper range for the varactor diodes. National Instruments PXIe-5645r (NI VST) is used as the transmitter baseband waveform generator and RF modulator, and also to downconvert and observe the RX signal. The actual processing and optimization algorithms run on a host processor, building on Labview to interface the NI VST and the digital computing software. The FPGA is connected to the host processor using a serial port.

4.9 Prototype Overview and Summary

The final version of the EBD prototype implementation is shown in Figure 48 including the hybrid junction, antenna tuning unit (ATU) and the balancing impedance. All the varactor control voltages are connected to the buffer and controlled with the digital control board. The

differential RX port terminations are properly mixed together with a 180° hybrid coupler working in the ISM Band.

(a) General system overview and lab equipment

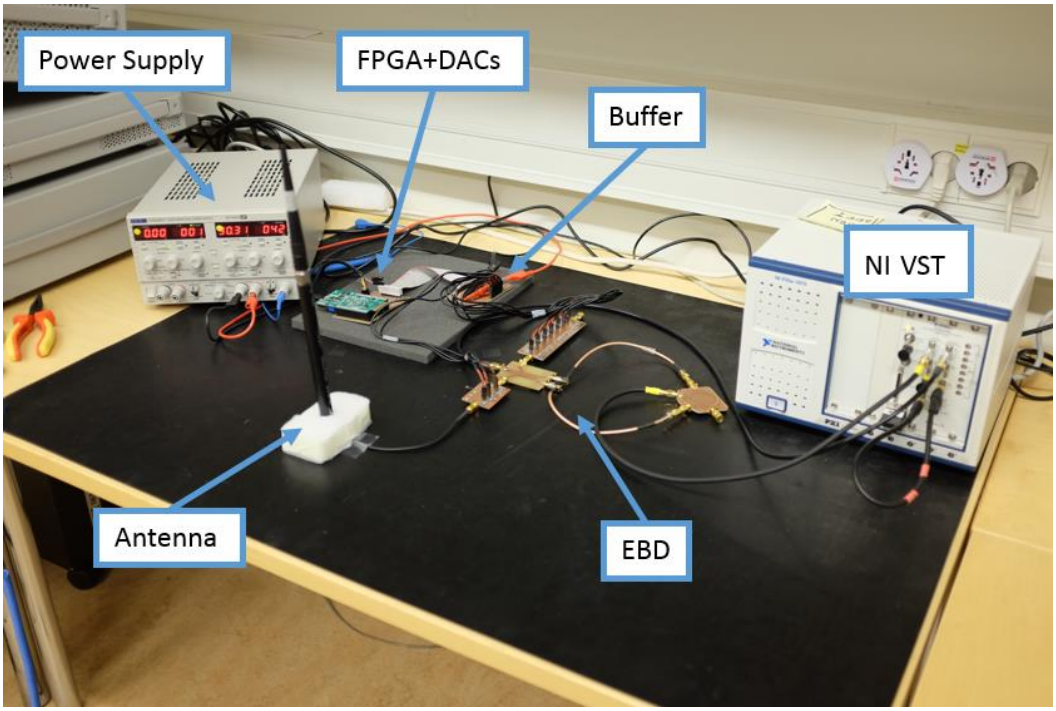

(b) Electrical balance duplexer

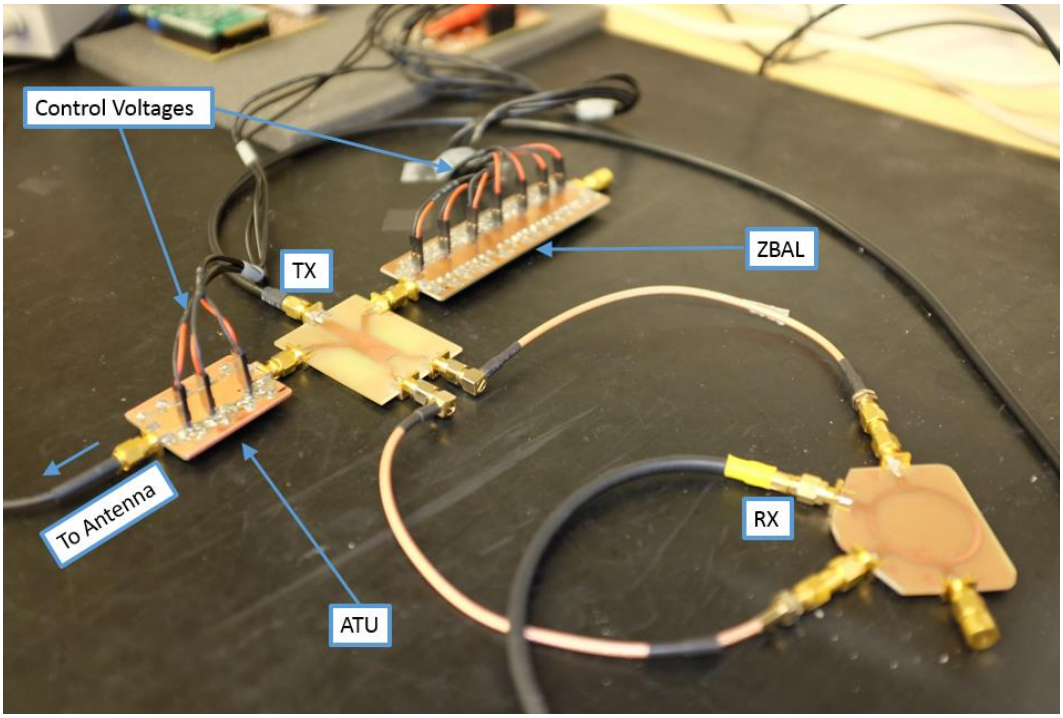

Figure 48. *(a) General system overview and lab equipment. (b) EBD prototype integrating an antenna tuning unit (ATU) and a balancing impedance (ZBAL)*

5. RF MEASUREMENTS AND RESULT ANALYSIS

In this chapter the measurement results of the implemented EBD are presented and analyzed. Each section describe an EBD's parameter starting from the isolation bandwidth, insertion losses, imbalance, CMRR, concluding with the linearity. Therefore, the isolation performances and the analysis results are reported for the automatic tuning algorithm. Then algorithm convergence speed and the measurement summary are presented at the end of the chapter.

5.1 Isolation Bandwidth

The isolation bandwidth and the TX-RX peak isolation are generally two different metrics to evaluate the duplexer isolation performance. The TX-RX peak isolation is given by the maximum level of isolation that the duplexer is able to achieve. This is often around 60-70 dB, which is a relatively high value for a small signal bandwidth. However, one of the key technical challenge in EBD is the given by the ability to achieve high isolation for wideband signals. In this case, the isolation bandwidth represents the most interesting parameter because it allows to describe the isolation performance for wideband signal. Generally, it is defined as the bandwidth where the isolation level is below a certain values. The typical value is 40 dB. In almost all the recent EBD implementations, the isolation bandwidth is found with a proper tuning of the balancing impedance maximizing the isolation for the frequency range of interest. Finding this value is quite challenging and it often requires a manual tuning of the balancing impedance. The measurement setup used to determine the 40 dB-isolation bandwidth is depicted in Figure 49.

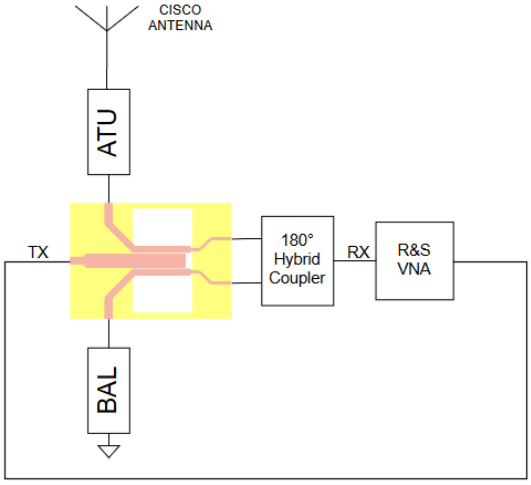

Figure 49. *Isolation bandwidth measurement setup. The VNA is inserted between the duplexer TX and RX ports.*

The *Rode&Schwarz* (R&S) ZLV Network Analyzer is connected to the TX and RX port of the EBD prototype. The TX power is chosen equal to 0 dBm to avoid to generate any intermodulation products on the ATU and balancing sides.

Both ATU and balancing impedance are manually tuned using the digital control. The ATU is tuned such that the return loss is greater than 10 dB in the ISM Band frequency range. Therefore the balancing impedance is tuned to maximize the TX-RX isolation bandwidth. Figure 50 shows the comparison between two isolation curves.
The measured 40 dB-isolation bandwidth of the implemented duplexer is depicted in blue, while the simulated one is represented in red.

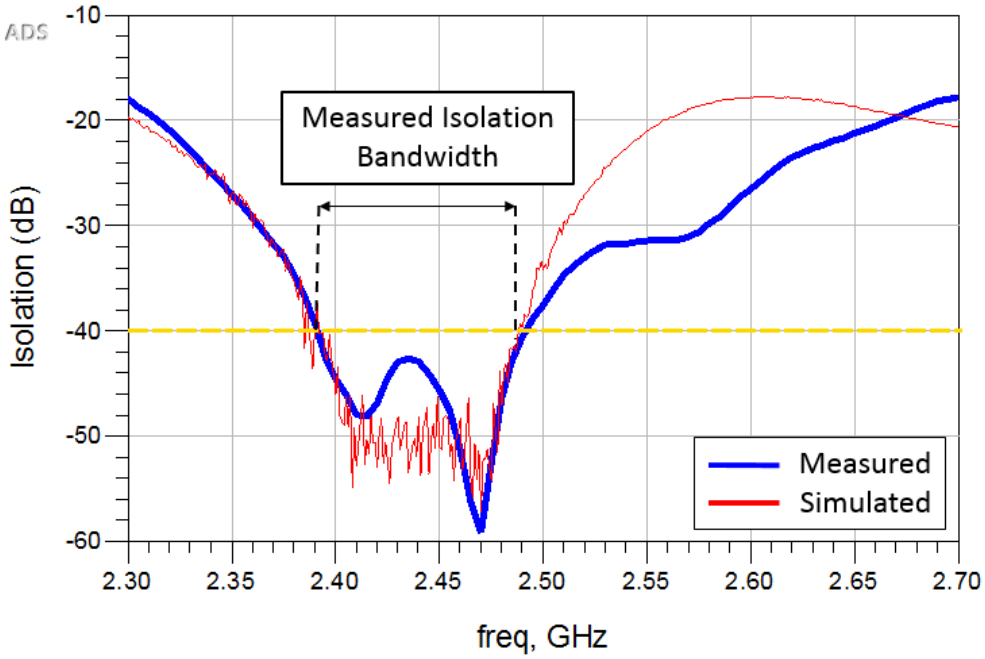

Figure 50. *Measured and simulated result of the 40 dB isolation bandwidth.*

The duplexer exhibits slightly more than 100 MHz 40 dB-isolation bandwidth and the overall isolation performance are comparable with the simulated one. This shows that the duplexer is able to theoretically and practically achieve more than 40 dB-isolation level for wideband signal up to 100 MHz.
Considering the measured isolation curves, it is possible to note the similarity with the one reported in Figure 30.b, where two poles are fitted inside the ISM Band. This is again, one of the main benefits given by the triple pole balancing network structure.

5.2 Insertion Losses

Two different setups are used to measure the TX and RX insertion losses. The R&S VNA is inserted between the TX and the antenna ports as depicted in Figure 51.a, in order to measure the TX insertion loss. Figure 51.b shows the RX insertion loss measurement setup where the VNA's probes are connected to the antenna and the RX ports. The power levels is set equal to 0 dBm. Figure 52 compares the TX and RX insertion losses measurements with the simulation result for the frequency range 2.3- 2.7 GHz.

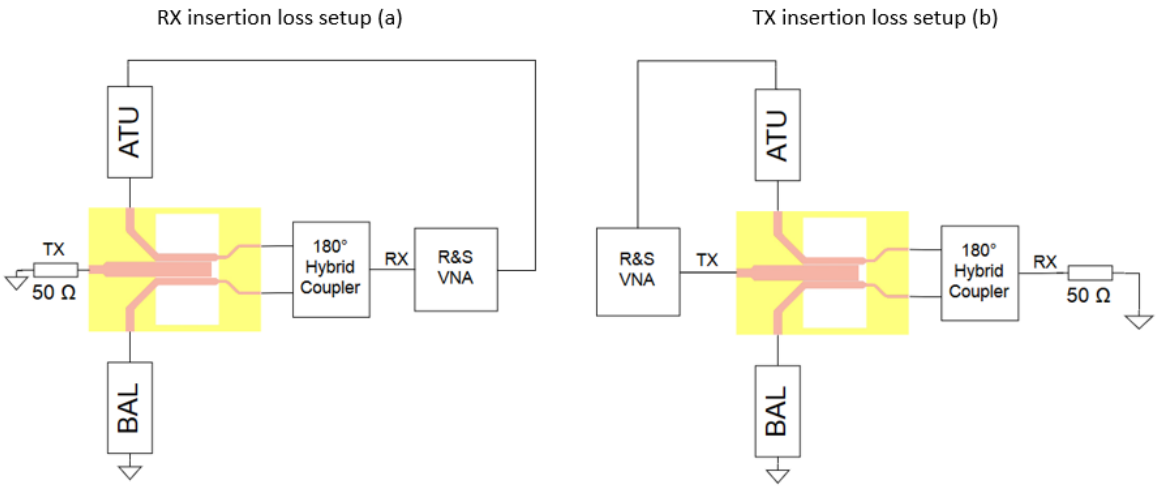

Figure 51. *Insertion losses measurement setup: (a) RX insertion loss measurement setup, (b) TX insertion loss measurement setup.*

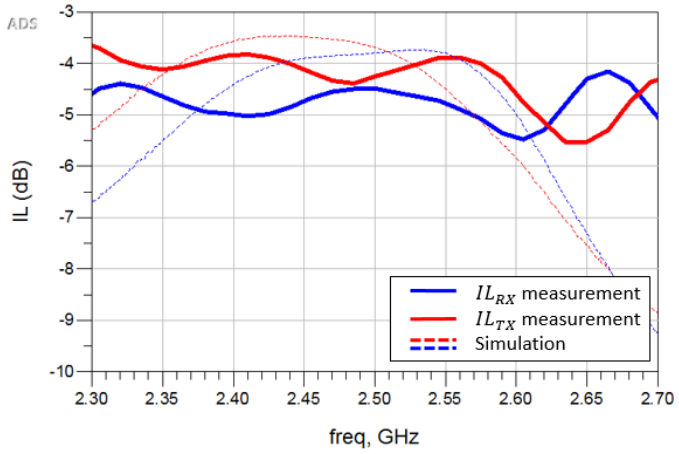

Figure 52. *Measured and simulated result for the TX insertion loss (red) and RX insertion loss (blue).*

The EBD prototype exhibits a IL_{TX} between 3.9 and 4.5 dB and IL_{RX} between 4.5 and 5 dB for the ISM Band frequency range. Both measured values for the TX and RX insertion losses are roughly 1 dB more than the expected value. The extra losses are substantially due to the non-idealities of the components, i.e. connectors, mutual parasitic effects, that have not been perfectly considered into the simulation. However, the obtained TX and RX insertion losses are comparable with the ones reported in the recent literature.

5.3 Imbalance

The magnitude and phase imbalance frequency responses are depicted in Figure 53, where simulation data (red) and measurements (blue) data are reported. The imbalance is measured with multiple VNA measurements between the TX and RX ports of the hybrid junction, matching the antenna and the balancing ports with a 50 Ω load. Therefore, (8) is applied to compute the magnitude and phase imbalance frequency response. Figure 53 shows that the measured magnitude response and phase response for the imbalance is less than 1 dB and 7° respectively

from 2.3 to 2.7 GHz. The measured parameters are aligned with the simulation results respecting the tolerance limits for differential device as reported in 4.4.

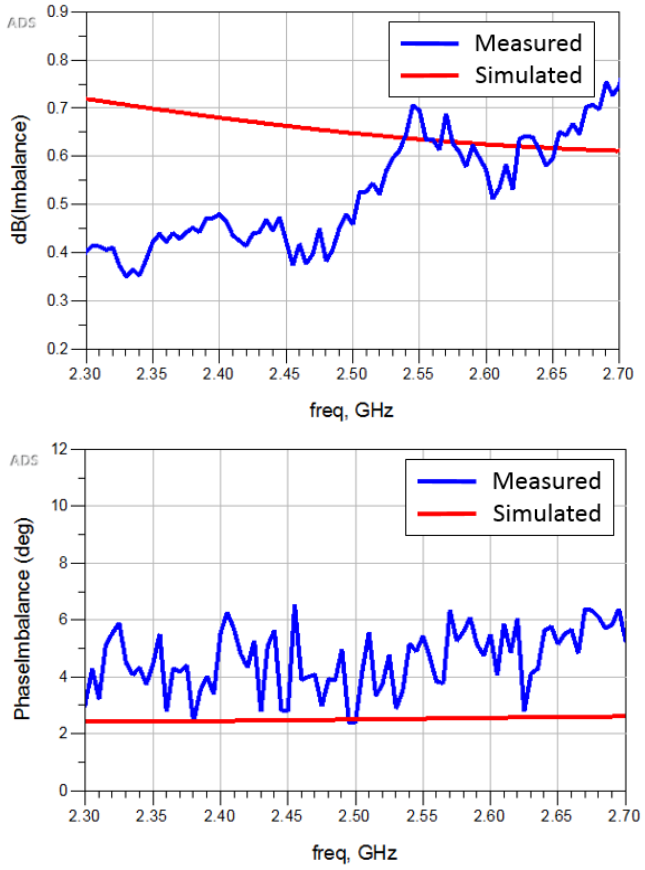

Figure 53. *Above: measured and simulated magnitude frequency response for the imbalance. On the Below: measured and simulated phase frequency response for the imbalance.*

5.4 CMRR

The measurement and the simulation result for the CMRR is illustrated in Figure 54. It is measured applying the Mixed Mode analysis and using the relations described in 2.4.1.

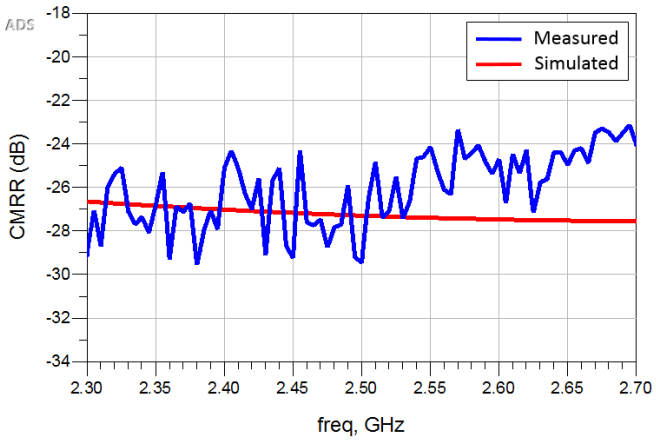

Figure 54. *Measured and simulated result for CMRR.*

Several different measurements are done with the R&S VNA closing both the antenna and the balancing impedance ports of the hybrid junction on 50 Ω terminations. Therefore, the Mixed mode S-parameter matrix is extracted for a two port differential device.
The measured CMRR swings between 24 and 29 dB for in the ISM Band frequency range respecting the simulated result. The measured CMRR is roughly 5 dB less than the typically required value (30 dB) for differential device, which means that the RX port is not perfectly balanced. This is mainly due to the intrinsic device asymmetry in the hybrid junction caused by the fabrication process. That of course would theoretically limit the overall isolation performance of the device, but from Figure 50 it is already possible to see that the duplexer can still achieve high isolation performance over a wideband frequency range. Thus, no additional optimization for enhance the CMRR performance is required.

5.5 Linearity

The setup used to measure the linearity of the duplexer is illustrated in Figure 55. Two vector signal generators (KeySight EXG N5172B and Hp Hewlett Packard E4437B) are used to generate two sinusoidal tones. Both generators are connected to the power combiner (Mini-Circuits ZN2PD2-63-S+) to produce the two-tone source, while the spectrum analyzer (CXA Signal Analyzer N9000A) is connected to each output port to measure the intermodulation products.

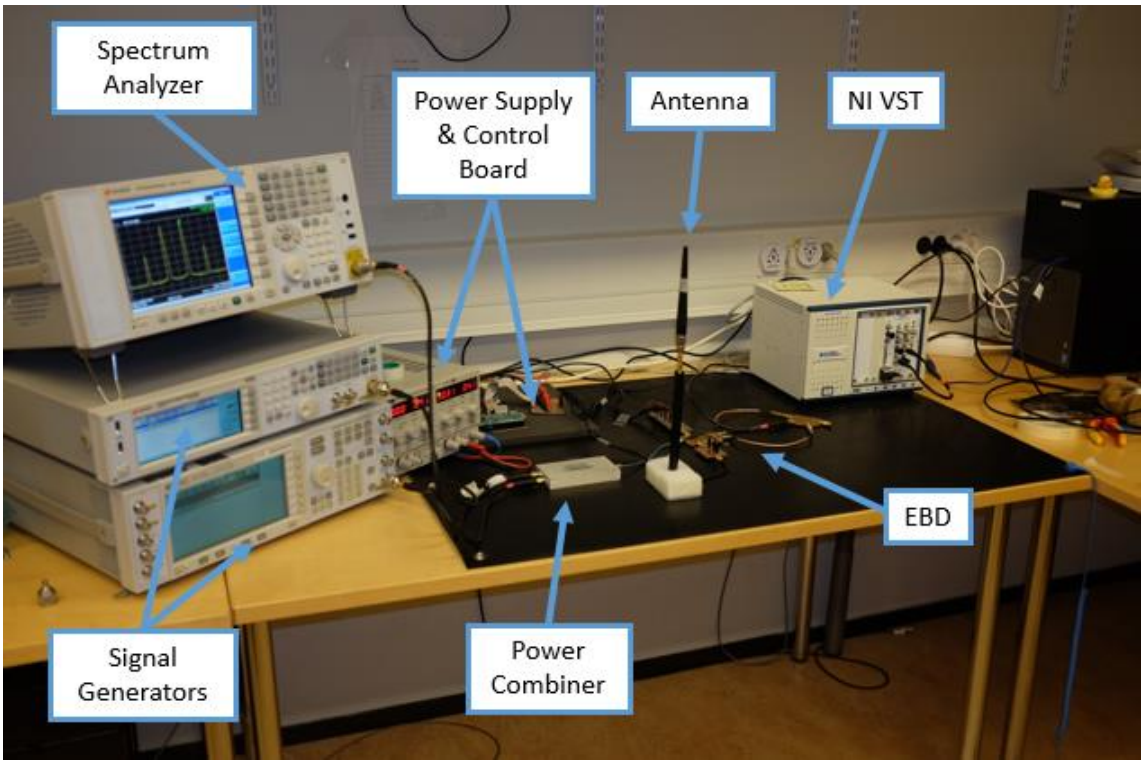

Figure 55. *Third Order Intercept Point (IIP3) measurement setup*

Here, two different measurement setups are used to measure the IIP_3, characterizing the duplexer's linearity. In the first setup, the two-tone source is injected in the TX port and the intermodulation products are measured at the antenna port, after the ATU. In the second setup,

the two-tone source is injected into the antenna port and the intermodulation products are measured at the RX port. With these two measurements it is possible to characterize the duplexer's linearity for both TX and the RX path. In order to properly measure the IIP_3, the power of the vector signal generators is chosen such that the distortion products of both the sources and the signal analyzer are significantly smaller than the distortion products introduced by the duplexer. The block diagrams for the two different setups are shown in Figure 56.

(a) TX path IIP_3 measurement setup

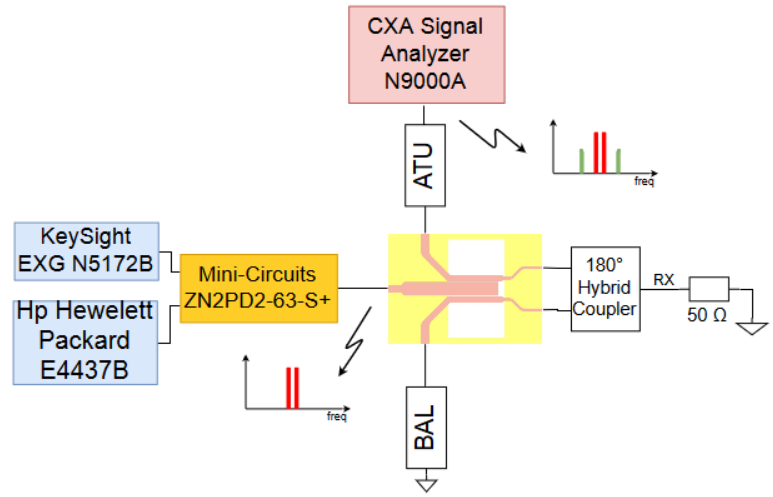

(b) RX path IIP_3 measurement setup

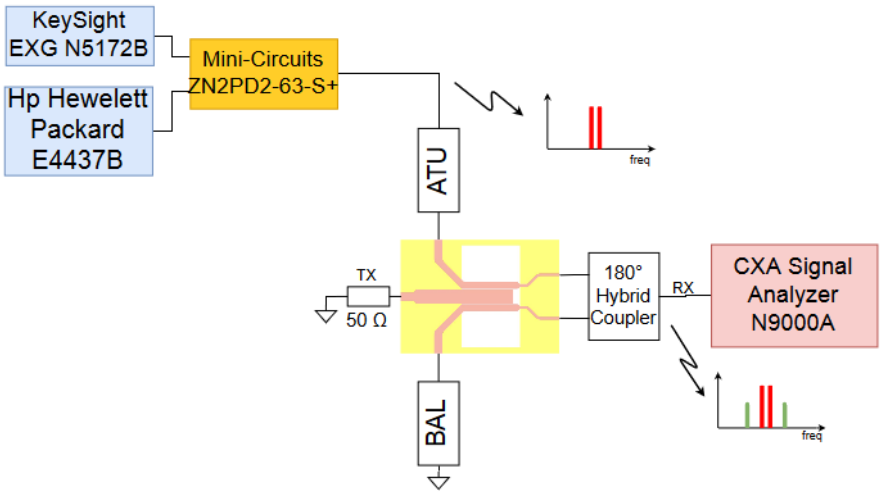

Figure 56. *Linearity measurement setups: (a) TX path IIP_3 measurement setup, (b) RX path IIP_3 measurement setup.*

The IIP_3 is found measuring the power level of the intermodulation products and applying (12) as reported in 2.6. Different power levels for the two-tone signal source are used. The IIP_3 measurement results for both TX and RX path are reported in Figure 57.

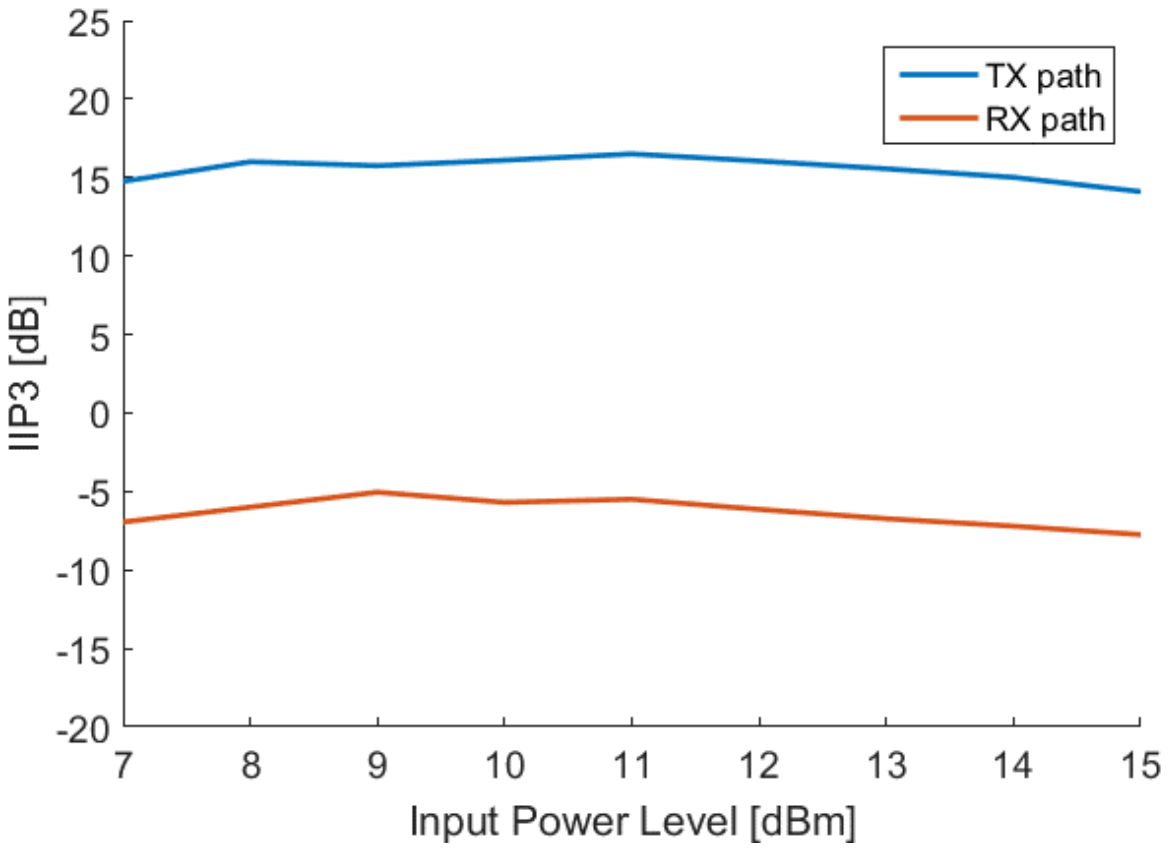

Figure 57. *TX and RX path IIP_3 measurement results.*

The measured IIP_3 curve is almost constant increasing the input power level and varying also the control voltage sets for the balancing impedance and ATU. The measured IIP_3 swings between 14 and 16 dB for the TX path and between -5 and -7 dB for the RX path.

5.6 Automatic Duplexer Tuning: Measurement Setup

In this section the measurement setup for the automatic duplexer tuning is described. Figure 58 shows the measurement setup where balancing impedance and the ATU are dynamically controlled through the adaptive digital control system.
In all the measurements, the operating center-frequency is 2.44 GHz at the corresponding ISM band. The TX signal is an LTE mobile cellular radio system compliant modulated waveform generated with the NI VST platform. The instantaneous bandwidth of the transmit waveform is also varied in the experiments, from 5 MHz up to 80 MHz.
In this experimental measurements the TX signal refers to the signal at the duplexer input, while the RX signal refers to the signal at 180° hybrid coupler output port.
Here, two different measurement tests are executed. Firstly, the TX signal is injected in the duplexer at 0 dBm power, and the secondly it is amplified to +20 dBm using an external low-cost PA.

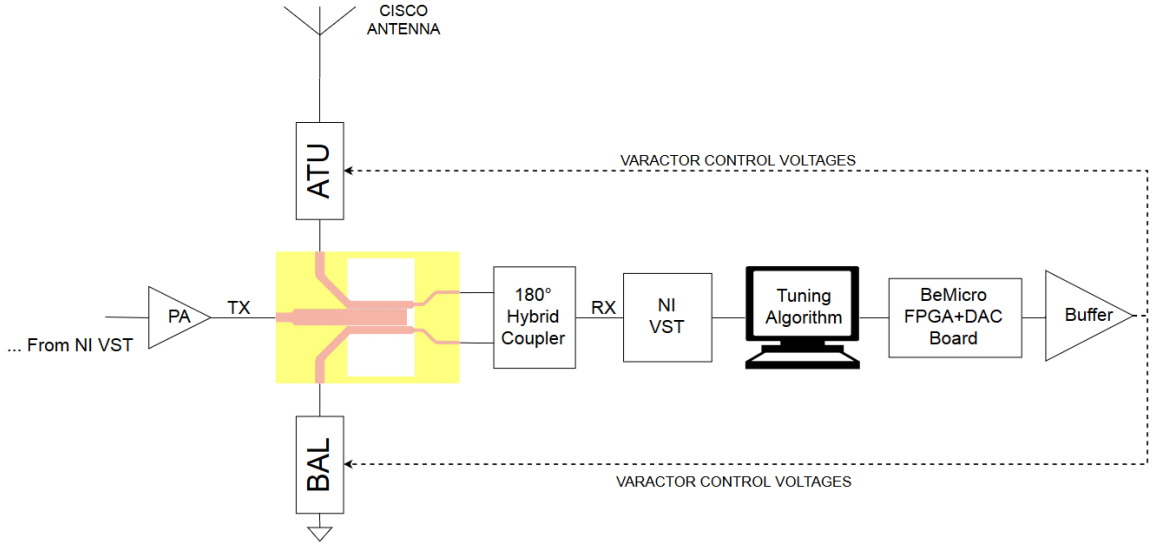

Figure 58. *Measurement setup high level diagram. The PA is inserted to evaluate the isolation performance for high TX power.*

5.7 Isolation Performance Measurements

In order to evaluate and demonstrate the performance of the developed digitally-controlled EBD prototype, different measurement test setups for different indoor scenarios are considered. These kind of scenarios are chosen according to [23] in order to measure the isolation performance in the most common real situations. Thus, the measurement test setups are constructed to simulate different antenna conditions, including standard lab conditions, presence of metal reflectors, as well as antenna-user interactions. For each scenario four different measurements of the isolation are obtained changing the instantaneous TX signal bandwidth and running the tuning algorithms at each change. The isolation performance is computed from the TX signal and the RX signal power levels at baseband. In the following pictures the TX signal baseband spectrum is depicted with the blue line, while the RX signal is shown in red. For the antenna-user interactions scenarios multiple colors are used to represent different interactions.
Figure 59 shows the measured isolation performance in standard lab conditions scenario where no objects surround the antenna, beside the laboratory equipment. This setup simulates the typical antenna condition in wireless access point, i.e. Wi-Fi repeater, where no obstacles are placed close to the antenna. However, the TX signal electromagnetic wave is still reflected back to the antenna by the surrounding elements, but those reflections are weak due to the path-loss, thus they are negligible.

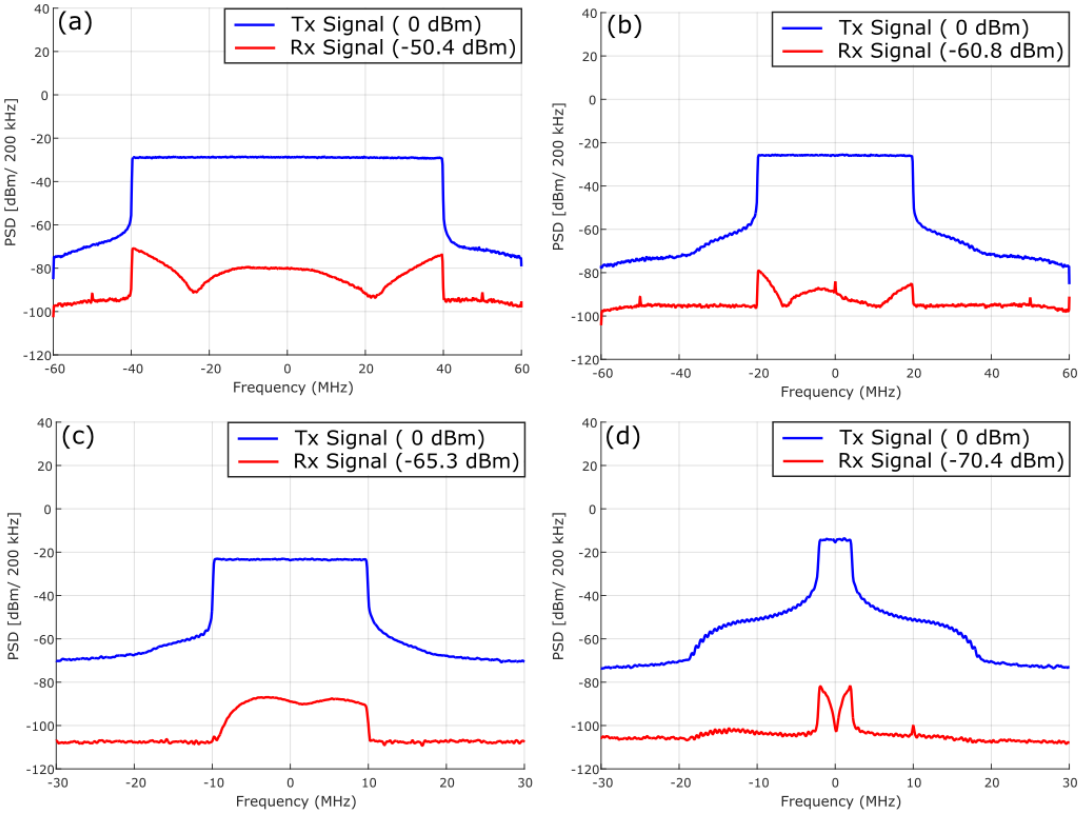

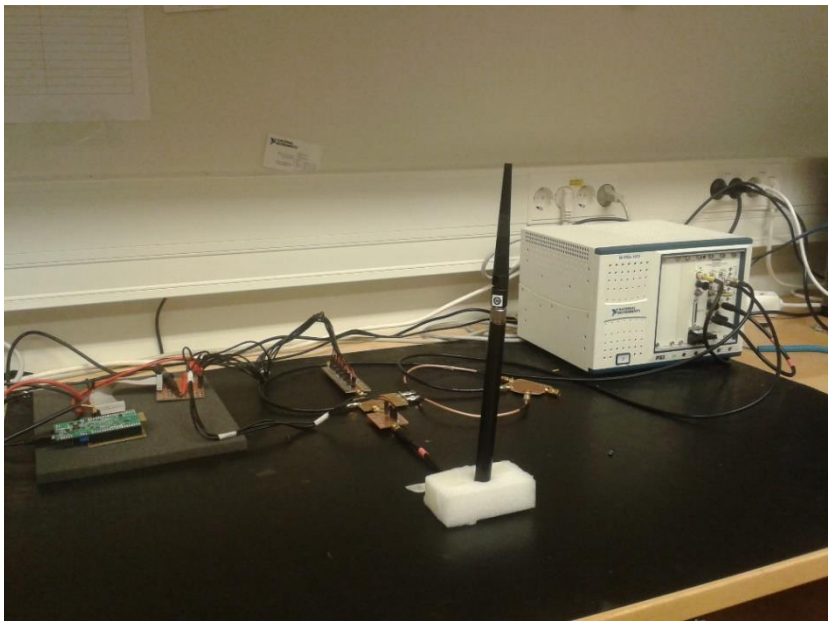

Figure 59. *Measured isolation performance in standard lab conditions scenario: (a) 80 MHz, (b) 40 MHz, (c) 20 MHz, (d) 5 MHz. In this measurement the TX power is 0 dBm.*

Figure 60 illustrates the metal reflector case, where several metal objects with different shape and size are placed close to the antenna simulating a reflective environment. Here, multiple reflections are created towards the antenna changing the antenna reflection coefficient. The energy of the electromagnetic wave associated to those reflectors is comparable with the TX signal and therefore cannot be neglected.

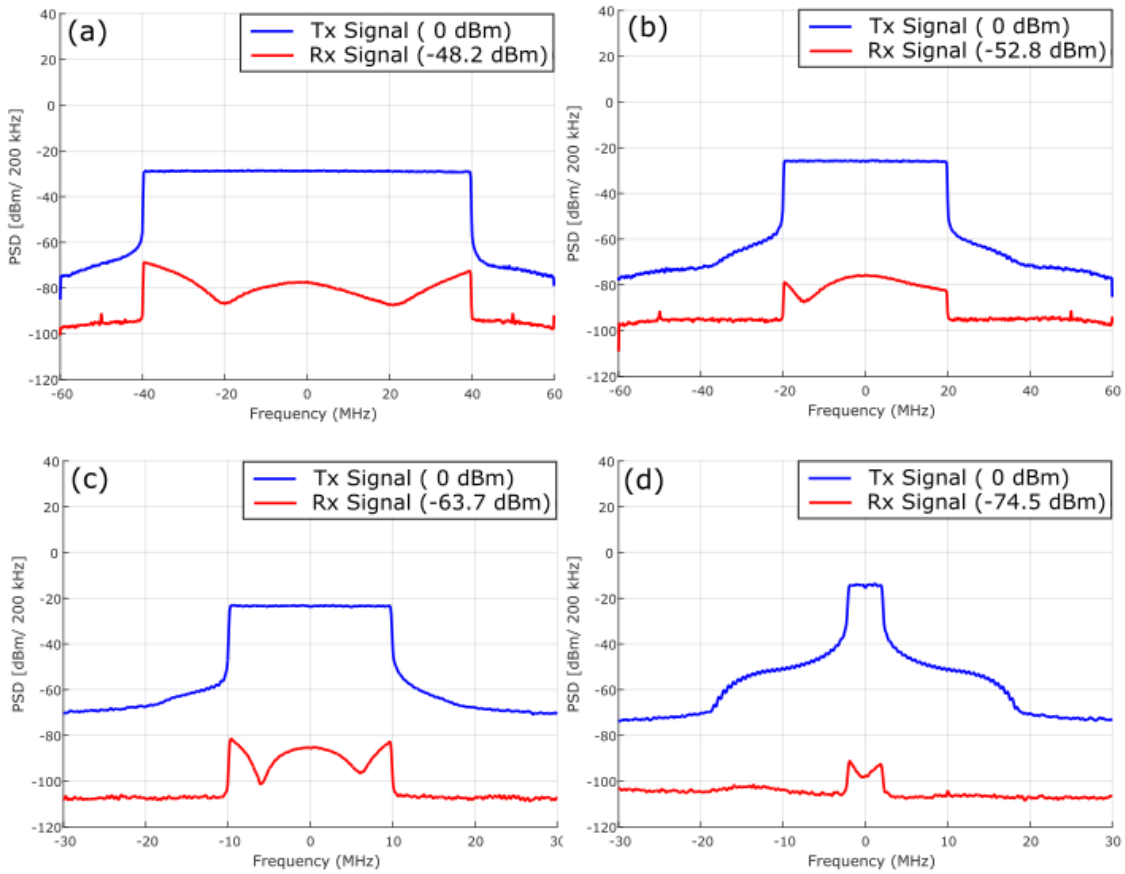

Figure 60. *Measured isolation performance in presence of reflectors scenario for different signal bandwidths: (a) 80 MHz, (b) 40 MHz, (c) 20 MHz, (d) 5 MHz. In this measurement the TX power is 0 dBm.*

Figure 61 represents the antenna-user interactions scenario. Here, the user hand moves around the antenna, creating strong reflections and changes in the antenna reflection coefficient.

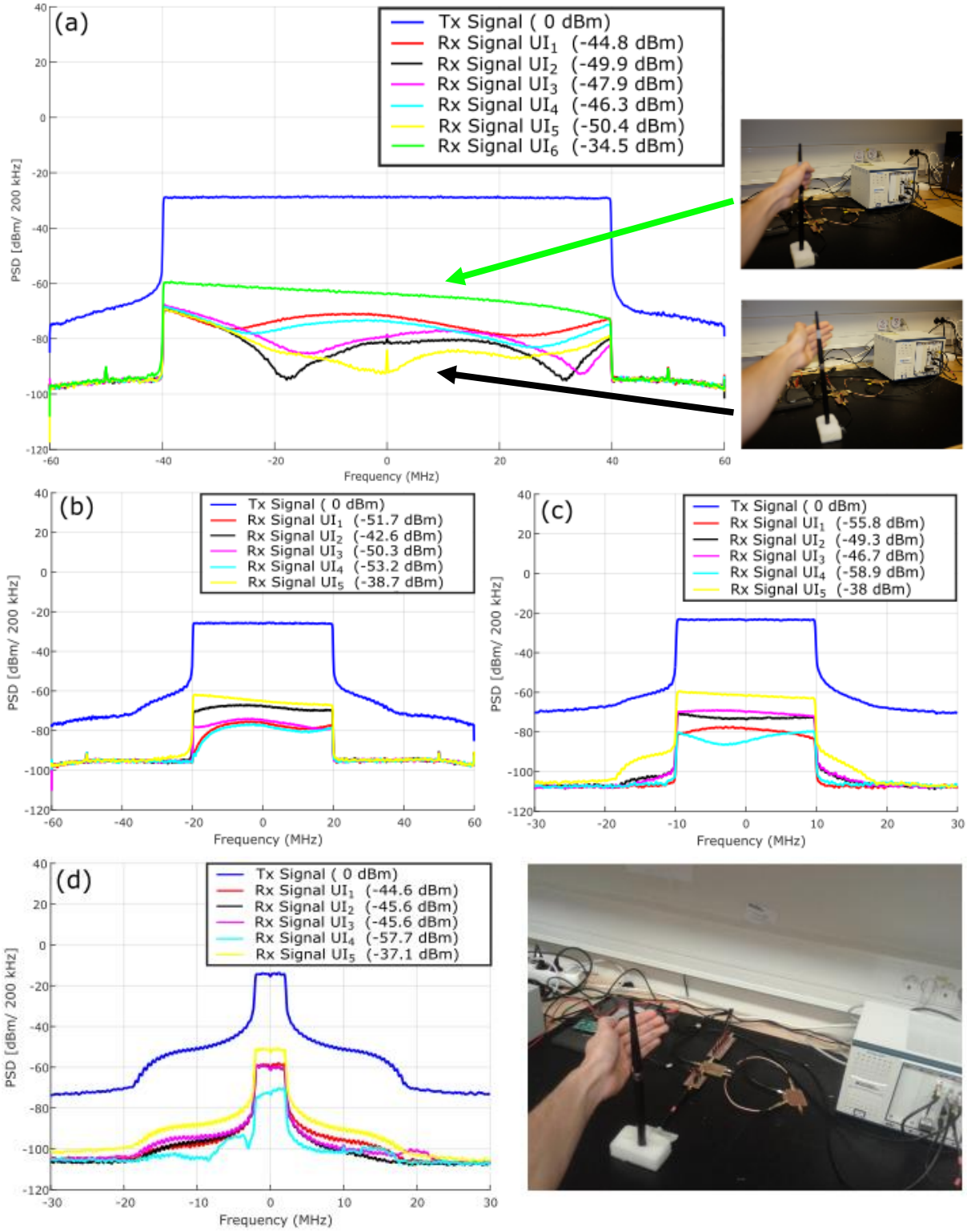

Figure 61. *Measured isolation performance in antenna-user interactions scenario for different signal bandwidths: (a) 80 MHz, (b) 40 MHz, (c) 20 MHz, (d) 5 MHz. In this measurement the TX power is 0 dBm.*

Five different measurements for the antenna-user interactions case are reported for each bandwidth value. In Figure 61 extra measurements imposing an aggressive change is done by fully grabbing the antenna with the hand, reflecting substantial antenna-user interactions, i.e. handheld devices. This specific measurement case is shown in green for the 80 MHz signal (Figure 61.a) and yellow for the other cases (Figure 61.b, Figure 61.c and Figure 61.d).
In Figure 62, the overall isolation performance are reported including a low-cost external PA, namely Texas CC2595. At these higher output power levels, this low-cost PA is already highly non-linear, thus reflecting realistic transmitter and SI scenarios in devices where the PA is pushed close to saturation for power-efficiency purposes, resulting into non-linear SI coupling to the own RX.

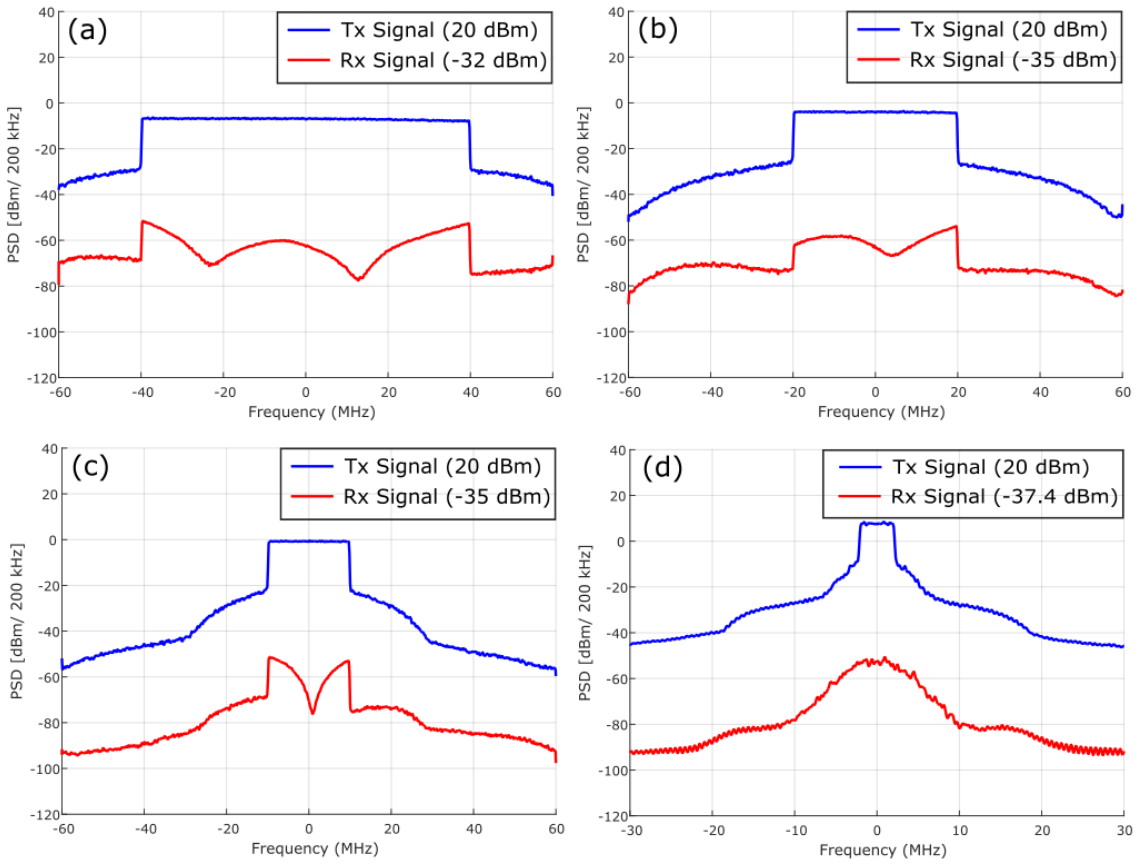

Figure 62. *Measured isolation performance in standard lab conditions scenario for different signal bandwidths: (a) 80 MHz, (b) 40 MHz, (c) 20 MHz, (d) 5 MHz. In this measurement the TX power is +20 dBm.*

Finally, Figure 64 represents three additional isolation measurements, carried out deliberately with different antennas working in the ISM Band. A standard lab condition setup is considered for those measurements. The first antenna is another Cisco-based antenna while the other two are different custom-made antennas developed at Tampere University of Technology, Finland, for FD device demonstration purposes. Figure 63 illustrates the three different antennas and the respective reflection coefficient measurements. The antenna reflection coefficients are measured from 2 to 3 GHz with the R&S VNA.

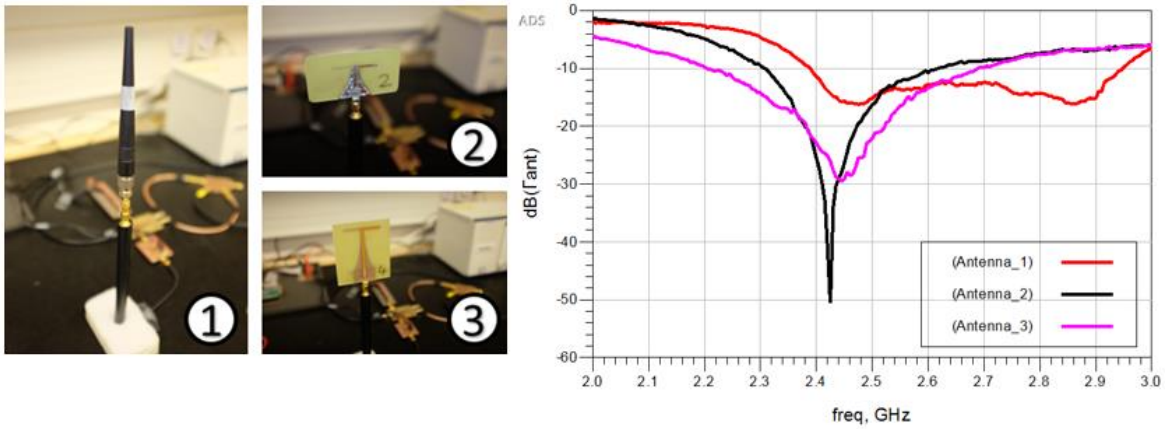

Figure 63. *EDB measurement setup with different antennas. On the left: (1) another Cisco-based antenna, (2)-(3) custom-made antennas developed at Tampere University of Technology, Finland. On the right: measured magnitude frequency response of the antenna reflection coefficients.*

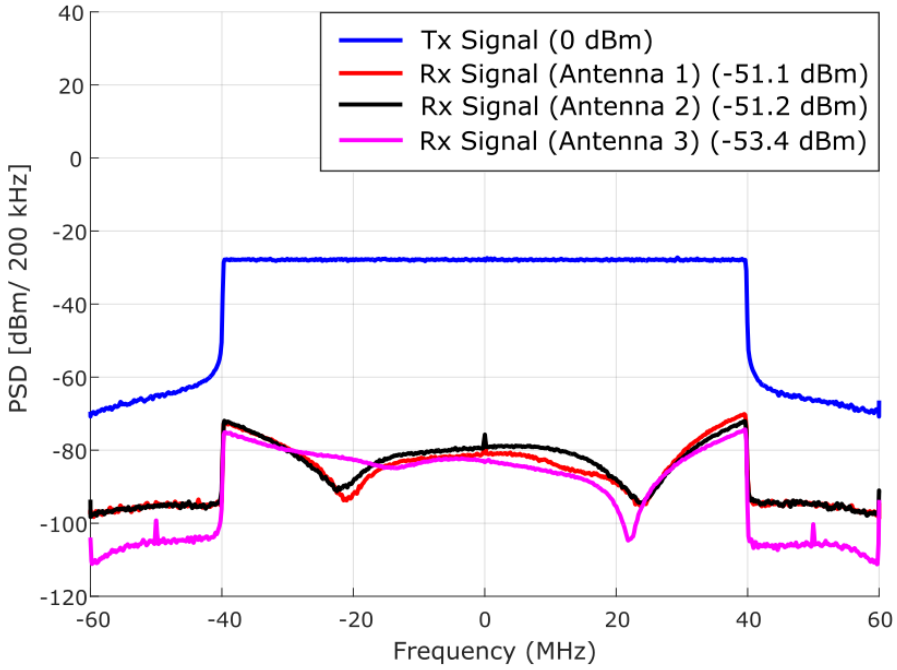

Figure 64. *Measured isolation performance with different antennas, again using 80 MHz instantaneous bandwidth at 2.44 GHz center-frequency. The TX power is 0 dBm.*

5.8 Analysis of the Isolation Performance Results

The measured duplexer isolation performances are very interesting for the 80 MHz instantaneous bandwidth signal case. These measurements are reported in Figure 59.a, Figure 60.a and Figure 61.a, for different scenarios, at 0 dBm TX power. In the standard lab conditions scenario, the developed EBD is able to reduce the SI power down to -50.4 dBm over the ambitious 80 MHz bandwidth, thus providing 50.4 dBs of TX-RX isolation. This represents a very high isolation value that is clearly outperforming the existing prototype measurement results in the literature, under such high instantaneous bandwidth and low-cost antennas. Then, similar iso-

lation performance is reported in Figure 60.a even when the surrounding environment is substantially more challenging containing now close-by reflecting objects. This is due to good tracking characteristics of the developed control system, tuning the balancing impedance accordingly. Next, in Figure 61.a, yet more aggressive changes are imposed by putting a hand completely around or close to the antenna, reflecting substantial antenna-user interactions. In such cases, very strong reflections are created, changing the characteristic impedance. Now, depending on the hand location and movements, the isolation varies between 50 dB and 35 dB. This is primarily due to the fact that the antenna-user interactions are here changing very fast, in time, and are thus difficult to track because of their nature. Figure 61.a illustrates the worst measured isolation performance equals to 35 dB (green line), where the user hand grabs the antenna in full. This is still an impressive result considering the isolation values of other TX-RX isolation circuitries such as circulators.

The isolation performance is measured also for 5, 20 and 40 MHz instantaneous signal bandwidths. All the measurements show that the isolation level increases by decreasing the instantaneous signal bandwidth, confirming the simulation result reported in [9]. High isolation peaks around 70-75 dB are achieved for 5 MHz signal bandwidth in the standard lab condition and the presence of reflectors scenarios as depicted in Figure 59.d and Figure 60.d. The isolation performance in the antenna-user interaction case varies between 37 and 57 dB depending on the position of the user's hand with respect to the antenna. However, those high levels of isolation refers to a small bandwidth condition.

Figure 65 represents then the measured EBD isolation performance for different instantaneous waveform bandwidths, in different reflection scenarios. In the case of antenna-user interactions, the reported isolation value corresponds to the average of the measured results with different hand locations.

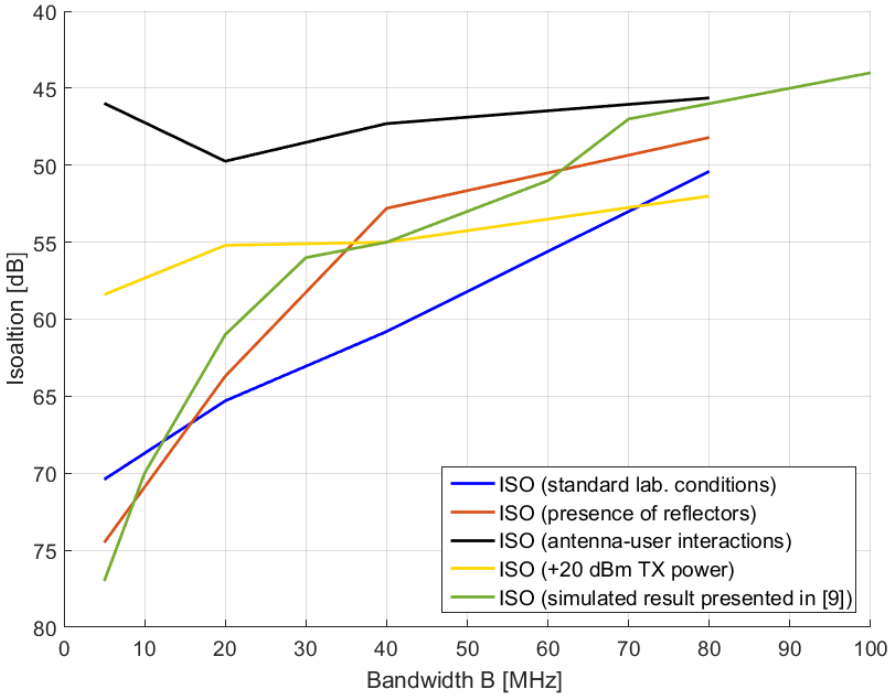

Figure 65. *Measured isolation performance versus instantaneous bandwidth.*

Also shown in Figure 65 are the measured isolation values with the low-cost PA involved, resulting to +20 dBm TX power. In general, based on the obtained results, it can be concluded that the EBD prototype and the associated digital control system perform very well even at higher TX powers and nonlinear SI. Compared to the 0 dBm transmit power case, in which the transmitter and EBD circuitry are essentially linear, the isolation performance with low-cost PA involved is somewhat decreased due to the non-linearity of the varactor diodes. This effect is clearly visible in Figure 62, especially for narrower carrier bandwidths. Here, any intermodulation products generated in the balancing network are in fact not perfectly balanced on the ATU side, degrading the effective isolation. The obtained results are next compared against those reported in [9], shown for convenience and reference also in Figure 65. The EBD developed in this thesis work achieves generally better isolation performance in case of wide instantaneous bandwidths. For narrower carrier bandwidths, the isolation values are essentially very similar. Two are the main reasons for obtaining enhanced isolation, compared to [9], with wideband signals. The first one is that in the developed EBD prototype there are overall ten different tuning variables, compared to five adopted in [9], controlling now both the ATU and the balancing impedance. This obviously simplifying the balancing operation, because it is done on both sides of the hybrid junction. Secondly, this duplexer implements both balancing impedance and ATU with varactors diodes, thus the balancing operation isn't affected by any balancing resolution constraint. Hence, the varactor diode capacitance can be continuously controlled through the reverse biasing control voltage. Differently, discrete balancing mechanisms are commonly adopted among the previous duplexer implementations, where discrete switching capacitor or resistor banks are integrated in the balancing impedance. Hence, those implementation suffers from a resolution constraint given by the minimum variation in the balancing impedance.

As Figure 65 shows, close to 10 dB improvement is thus obtained at 80 MHz instantaneous bandwidth. On the other hand, adding a yet more complex balancing network or more complex ATU would not essentially improve the overall isolation performance anymore, most likely. Furthermore, since the ATU and the balancing impedance are both realized with the same dielectric substrate and components, this yields intuitively a feasible balancing operation in the EBD.

As illustrated in Figure 64, the digital control system can again reliably tune the ATU and balancing impedance such that more than 50 dB of TX-RX isolation is obtained with different antennas and with ambitious instantaneous bandwidth of 80 MHz. This is different to most other reported works, which are typically deliberately designed and optimized for a particular antenna, i.e. PIFA. As the overall digitally-controlled EBD concept reported in this thesis work is able to tune and control both the antenna characteristics and the balancing impedance, substantial robustness is thus obtained.

5.9 Algorithm Convergence Speed

In Figure 66, an example of the learning characteristics and convergence of the digital control system is shown, in the form of the measured isolation versus the iteration number *N*. This

example is obtained with 80 MHz waveform bandwidth and measured in standard lab conditions. In this example, the balancing impedance tuning is done first, followed by the tuning of the ATU. As the figure illustrates, the overall control system converges fast and reliably in the true RF measurements.

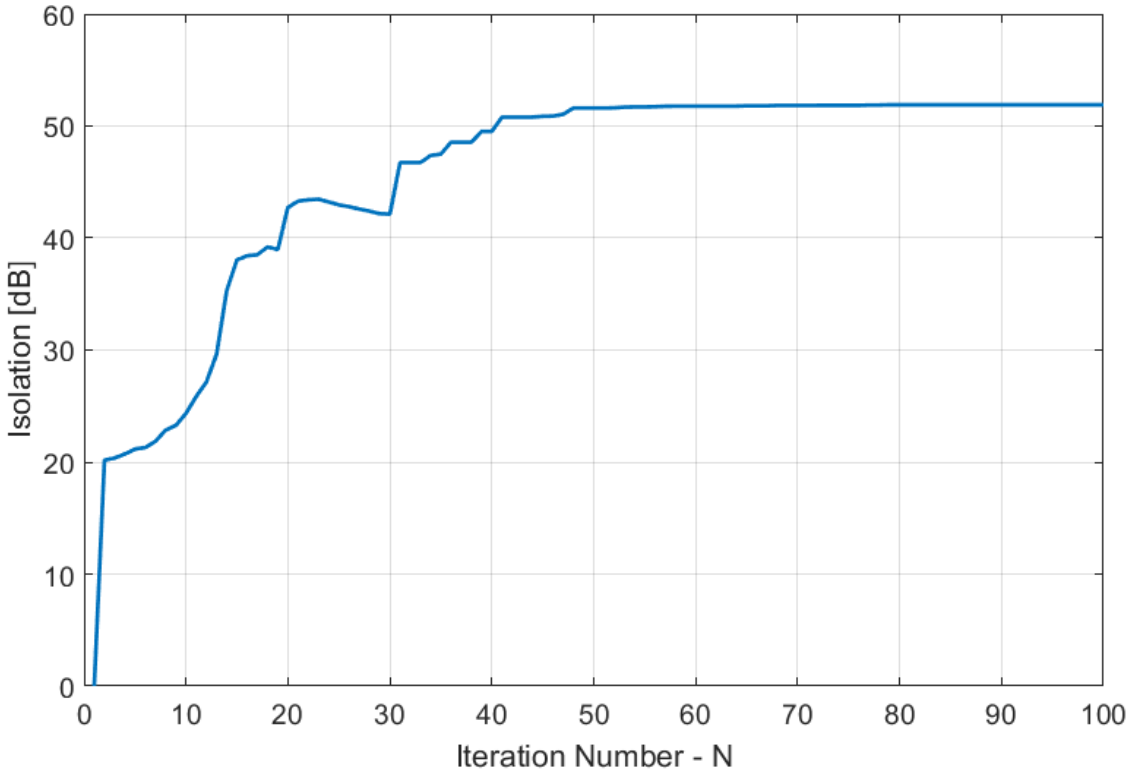

Figure 66. *An example illustration of the control system converge in terms of the measured isolation vs. the iteration number N. In this example, the balancing impedance is tuned first, for 0 < N < 25, while the antenna tuning unit (ATU) is being tuned then for 29 < N < 55, until the isolation converges.*

5.10 Measurement Summary

Table 3 gives the measurements summary of the implemented duplexer, comparing the overall performance with the previous works. The isolation characteristic of the duplexer is greater than 50 dB for an associated instantaneous bandwidth of 80 MHz satisfying the design goal. Up to 100 MHz 40dB-isolation bandwidth is measured enhancing the isolation capability with wideband signals. The measured TX and RX insertion losses are higher than the expected ones. This is partially due to the non-optimized prototype's layout, which has not been minimized during the design process and also to the low cost dielectric board material which is lossy. However, the TX and RX insertion loss are in line with the previous duplexer works. The prototype exhibits a relatively unexpected high linearity for both TX and RX paths. This is due to intrinsic design property of the duplexer. The ATU and balancing impedance are both realized with varactor diodes, thus the intermodulation products generated on the ATU side can be partially balanced from the balancing impedance side of the hybrid junction. Therefore, high isolation performance are achieved even with highly non-linear power amplifier boosting the

TX signal power level up to +20 dBm. In this case, the isolation performance decreases for small signal bandwidths, where the signal spectrum appears extremely corrupt and the balancing operation becomes more challenging. The implemented prototype exhibits poor linearity for the RX path. However, the RX signal power is often extremely low, i.e. -20 dBm, compared to the TX one. With these power levels the obtained IIP_3 represents a safety value to not incur in heavy intermodulation distortion.

Parameters		**This work**	**Design Goals**	**[11]**	**[35]**	**[14]**	**[10]**	**[12] [34]**	**[18] [24]**
Frequency Range[GHz]		2.4-2.48	2.4-2.48	2.4-2.48	1.9-2.2	1.5-2.5	1.7-2.2	1.7-2.2	1.8-2.2
Typology		FD	FD	FD	FD	DB	DB	DB	DB
Max TX power[dBm]		20	20	0	27	24	27	27	24
IL_{TX}**[dB]**		4.5	4	3.4	3.7	5.9	4.7	3.8	2.2
IL_{RX}**[dB]**		5	4	-	3.9	2.9	-	4	-
IIP_3**[dB]**	TX path	14	20	-	40	-	-	-	-
	RX path	-7	0	-	42	-	-5.6	-4.6	-
TX-RX Isolation	Isolation[dB] $_{TX-RX}$	53.4	>40	50	50	50-50	70-40	50-50	55 -45
	Ass. BW [MHz]	80	80	20	-	5	20	6	-
40 dB Isolation Bandwidth [MHz]		100	80	-	>250*	20	-	20	>250*
Technology		Discrete	Discrete	0.18µm CMOS	0.18µm CMOS	40 nm CMOS	90 nm CMOS	65 nm CMOS	65 nm CMOS
Balancing Impedance Tuning Dimension		7	7	2	4	2	2	7	2
ATU Tuning Dimension		3	3	-	-	-	-	-	-
Area [mm^2]		PCB	PCB	0.4	1.75	0.2	0.6	2.2	0.2

*with the duplexer's antenna port closed on 50 Ω termination or the balancing operation is done using an external impedance tuner.

Table 3. *Implemented duplexer performance comparison.*

The prototype was not able to meet all the design goals, but it exhibits extraordinary isolation performance for wideband signals. In almost all the recent works the on-chip prototypes show high isolation performance just for narrowband signal. High isolation bandwidth are reported in Table 3 for specific cases, where the antenna port of the duplexers are terminated on 50 Ω resistor or the balancing operation is done with an external electronically controlled impedance tuner.

6. CONCLUSIONS

This thesis work presents a novel digitally-controlled *electrical balance duplexer* (EBD) prototype capable of *full-duplex* (FD) radio communications. The key technical challenge in FD communication consists in removing the strong *self-interference* (SI) which is caused by the *transmitting* (TX) leakage into the *receiving* (RX) chain. Therefore, high TX-RX isolation requirements are needed in FD transceiver in order to suppress the SI, protecting the RX sensitiveness and relaxing the *analog-to-digital converter* (ADC) dynamic range requirements in the RX architecture. Such EBD can enable relatively high TX-RX isolations representing one valid option to pursue FD operation.

The aim of this master thesis consists in proofing the EBD working principle and isolation property. The prototype has been designed, fabricated and tested in the department of Electronics and Communications Engineering at Tampere University of Technology (TUT). The project has been carried out in collaboration with Intel Wireless Labs. The design is inspired to the previous duplexer works that can be found in the recent literature. Multiple concepts are mixed together to implement the final version of the prototype. Differently from the previous works, the author has decided to integrate an *antenna tuning unit* (ATU) in the duplexer, which benefits were just theoretically discussed in [18]-[15].

The measurement results presented in Chapter 5, show an improvement in the overall isolation performance for wideband signal with respect to the previous works. The most important experimental result shows that the developed EBD prototype can achieve up to 53 dB of isolation over an ambitious 80 MHz wide instantaneous *long term evolution* (LTE) signal waveform and integrating a real Cisco-based antenna. This result is obtained considering the EBD operating in standard lab conditions scenario and a TX power of 0 dBm. Furthermore, isolation performances are measured with different scenarios, when operating with different antennas and under a low-cost highly nonlinear power amplifier. In all those cases the duplexer isolation performance is still impressive. This is due to the self-adaptive or self-healing digital control system, which enables automatic tracking of time-varying antenna impedance characteristics, providing robustness against fast changes in the surrounding environment and against user interactions.

Comparing the obtained results with the previous works it is possible to conclude that the TX-RX isolation levels are very good. Therefore, the implemented EBD exceed all the previous duplexer in their isolation property. This is mainly due to the ten different control variables than can be tuned during the balancing operation. Several design parameters can be still optimized such as TX and RX insertion losses and *common mode rejection ratio* (CMRR) to improve the isolation performance. Concerning its physical implementation, the duplexer consists in three different PCBs which have to be connected together ending up in a 20x10 cm board. Thus, this implementation cannot be squeezed on a chip, making it suitable just for non-handheld devices, i.e. relay station. For time reasons, in fact, the prototype is at its first revision and it has not be optimized in its physical layout implementation because the main goal is only

for demonstration purposes. Thus, the future work will focus on improving the TX and RX paths insertion losses as well as increasing the layout miniaturization.
In conclusion, this thesis work shows that relatively high TX-RX isolation can be achieved using EBD. This contribute to pursue FD operation as one of the most essential targets and ingredients towards the 5G radio networks.

REFERENCES

[1] A. Sabharwarl, P. Schiniter, D. Guo, D. Bliss, S. Rangarajan and R. Wichman, "In-band full-dulex wireless: Challenges and opportunities", *IEEE Journal on Selected Areas in Communications,* vol 32, no. 9, pp. 1637-1652, Oct 2014.

[2] T. Huusari, Y.S. Choi, P. Liikkanen, D. Korpi, S. Talwar, M. Valkama, "Wideband Self-Adaptive RF Cancellation Circuit for Full-Duplex Radio: Operating Principle and Measurements", *IEEE Vehicular Technology Conference (VTC) Spring,* 2015.

[3] M. Duarte, C. Dick, and A. Sabharwal, "Experiment-driven characterization of full-duplex wireless systems," *IEEE Transactions on Wireless Communications,* vol. 11, no. 12, pp. 4296–4307, Dec. 2012.

[4] A. Sabharwarl, P. Schiniter, D. Guo, D. Bliss, S. Rangarajan and R. Wichman, "In-band full-dulex wireless: Challenges and opportunities", *IEEE Journal on Selected Areas in Communications,* vol 32, no. 9, pp. 1637-1652, Oct 2014.

[5] M. Duarte, C. Dick, and A. Sabharwal, "Experiment-driven characterization of full-duplex wireless systems," *IEEE Transactions on Wireless Communications,* vol. 11, no. 12, pp. 4296–4307, Dec. 2012.

[6] E. Everett, M. Duarte, C. Dick, and A. Sabharwal, "Empowering fullduplex wireless communication by exploiting directional diversity," in *Proc. 45th Asilomar Conference on Signals, Systems and Computers,* Nov. 2011, p. 2002-2006.

[7] J. I. Choi, M. Jain, K. Srinivasan, P. Levis, and S. Katti, "Achieving single channel, full duplex wireless communication," in *Proc. 2010, International Conf. Mobile Comput. Netw.*, pp. 1–12.

[8] D. Bharadia, E. McMilin, and S. Katti, "Full duplex radios," in *Proc SIGCOMM'13,* Aug. 2013, pp. 375–386.

[9] L. Laughlin, M. Beach, K.A. Morris, "Electrical Balance Isolation for Flexible Duplexing in 5G Mobile Devices", *IEEE Communication Workshop ICCW,* Jun. 2015.

[10] S.H. Abdelhalem, P.S. Gudem, L.E. Larson, "Hybrid Transformer-Based Tunable Differential Duplexer in a 90-nm CMOS Process", *IEEE Transcations Microwave Theory and Techniques,* vol 61, no. 3, pp.1316-1326, Feb. 2013.

[11] M. Mikhael, B. Liempd, J. Craninckx, R. Guindi, B. Debaillie, "An In-Band Full-Duplex Transceiver Prototype with an In-System Automated Tuning for RF Self-Interference Cancellation", IEEE *International Conference (5GU),* Nov. 2014.

[12] S.H. Abdelhalem, P.S. Gundem, L.E. Larson, “Hybrid Transformer-Based Tunable Integrated Duplexer with Antenna Impedance Tracking Loop”, *IEEE Custom Integrated Circuits Conference (CICC),* Sept. 2013.

[13] L. Laughlin, M.A.Beach, K.A. Morris, J.L. Haine, “Optimum Single Antenna Full Duplex using Hybrid Junctions”, IEEE *J. on Sel. Areas in Commun. (JSAC),* vol 32, no. 9, pp1653-1661, Sept 2014.

[14] M. Mikherman, H. Darabi, A. Abidi, “A Tunable Integrated Duplexer with 50 dB Isolation in 40nm CMOS”, *IEEE International Solid-State Circuits Conference*, 2009.

[15] L. Laughlin, M.A.Beach, K.A. Morris, J.L. Haine, “Electrical Balance Duplexing for Small Form Factor Realization of In-Band Full Duplex”, *IEEE Communication Magazine*, May 2015.

[16] A. Kumar, S. Aniruddhan, R.K. Ganti, “Directional Coupler, with High Isolation Bandwidthusing Electrical Balance”, *IEEE Microwave Symposium (IMS*), 2014.

[17] M. Thompson, J. K. Fidler, “Determination of the Impedance Matching Domain of Impedance Matching Networks”, *IEEE Transaction on Circuit and System,* vol 51, no. 10, Oct 2014.

[18] H. Darabi, A.Mirzaei, M.Mikhemar, “Highly Integrated and Tunable RF Front Ends for Reconfigurable Multiband Transceiver: A Tutorial”, *IEEE Transaction on Circuit and Systems,* vol 58, no. 9, Sept 2011

[19] J. de Mingo, A. Valdovinos, A. Crespo, D. Navarro, P. Garcìa, “An RF Electronically Controlled Impedance Tuning Network Design and its Application to an Antenna Input Impedeance Automatic Matching System”, *IEEE Transaction on Microwave Theory and Techniques,* vol. 52, no. 2, 2004.

[20] C. Hoarau, P.-E. Bially, J.-D. Arnould, P. Ferrari, P. Xavier, “An RF Tunable impedance Matching Network with a Complete Design and Measurement Methodology”, *IEEE European Microwave Conference,* Oct 2007.

[21] A.C. Carusone, D.A. John, “Analog Filter Adaptation using a Dithered Linear Search Algorithm”, *IEEE Transaction on Circuit and Systems,* vol. 4, 2002.

[22] W.H Press, S.A. Teukolsky, W.T. Vetterling, B.P. Flannery, “Downhill Simplex Method in Multidimensions”, *Numerical Recepies in C*, chapter 10, section 10.4, 1992.

[23] L. Laughlin, M.A.Beach, K.A. Morris, J.L. Haine, “Performance Variation in Elecrical Balance Duplexers due to User Interaction”, *IEEE International Symposium on Personal, Indoor, and Mobile Radio Communication (PIMRC),* Sept. 2014.

[24] M. Mikhemar, H. Darabi, A. Abidi, “An On-Chip Wideband and Low-Loss Duplexer for 3G/4G CMOS Radios”, 2010.

[25] John R. Long, “Monolithic Transformer for Silicon RF IC Design”, 2000.

[26] Ali M. Niknejad “Passive Devices for Communication Integrated Circuits”,2014.

[27] Mini Circuits, “RF and Microwave Transformer Fundamentals”, 2009.

[28] C. Hoarau1, P.-E. Bailly, J.-D. Arnould, P. Ferrari, and P. Xavier, “A RF Tunable Impedance Matching Network with a Complete Design and Measurement Methodology”, 2008.

[29] Y.S. Choi, H. Shirani-Mehr, “Simultaneous Transmission and Reception: Algorithm, Design and System Level Performance”, *IEEE Transaction on Wireless Communications*, vol. 12, no. 12, Dec. 2013.

[30] G. A. Campbell and R. M. Foster, “Maximum Output Networks for Telephone Substation and Repeater Circuits”, *Am. Inst. Electron. Eng. Trans.*, vol. 39, no. 1, 1920, pp. 231-90.

[31] Agilent Technologies, “Multiport & Balanced Device Measurement Application Note Series”, *Concepts in Balanced Device Measurements*, Application Note 1373-2.

[32] E.F. Sartori, “Hybrid Transformer”, *IEEE Transaction on Parts, Materials and Packing*, vol. PMP-4, no. 3, Sept. 1968.

[33] L. Laughlin, M. Beach and K.A. Morris, “Electrical Balance Duplexer in Indoor Mobile Scenario”, *IEEE Antennas and Propagation (EuCAP) Conference*, April 2015.

[34] S.H. Abdelhalem, P.S. Gudem, L.E. Larson, “Tunable CMOS Integrated Duplexer With Antenna Impedance Tracking and High Isolation in the Transmit and Receive Bands”, *IEEE Transaction on Microwave Theory and Techniques*, vol. 62, no. 9, Sept. 2014.

[35] B.V. Liempd, B. Hershberg, K. Raczkowski, S. Ariumi, U. Karthaus, K. F. Bink, J. Craninckx, “A +70dBm IIP3 Single-Ended Electrical-Balance Duplexer in 0.18µm SOI CMOS”, *IEEE International Solid-State Circuit Conference*, 2015.

[36] Y. Sun, J. Moritz, Xi Zhu, “Antenna Impedance Matching and Antenna Tuning for Green Software-defined and Cognitive Radio”, *IEEE Transaction on Circuit and Systems*, Aug. 2011.

[37] Y. Sun and J.R. Moritz, “Frequency Agile Antenna Tuning and Matching”, *IET HF Radio System and Techniques*, 2000.

[38] Y. Sun and J.K. Fidler, “Design Method for Impedance Matching Networks”, *IET Transaction in Circuits , Devices and Systems*, vol. 143, no.4 , Aug. 2002.

[39] Y. Sun and J.K. Fidler, “Practical Considerations of Impedance Matching Network Design”, *IET HF Radio System and Techniques*, 1994.

[40] Y. Sun and J.K. Fidler, “Components Value Ranges of Tunable Impedance Matching Networks in RF Communications Systems”, *IET HF Radio System and Techniques*, 1997.

[41] A. Huynh, M. Karlsson, S. Gong, “Mixed-mode S-parameters and Conversion Techniques”, Linköping University, Sweden.

[42] D.E. Marthaler, “An Overview of Mathematical Methods for Numerical Optimization”, *Numerical Method for Metamaterial Design.*

[43] Cisco, “Cisco Visual Networking Index: Global Mobile Data Traffic Forecast Update, 2015-2020”, Feb. 2016.

[44] D.M. Pozar, Microwave Enginerring, 4th edition, 2012.